

CALIFORNIA STATE POLYTECHNIC UNIVERSITY, POMONA
THESIS ELECTRONIC SIGNATURE PAGE

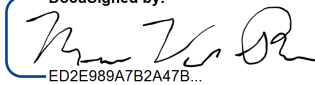
Submitted: Term Spring Year 2021
Bronco ID: 013534911
Email Address: gblachly@cpp.edu

THESIS INFORMATION


THESIS TITLE THE LUDLOW BATHOLITH, CENTRAL MOJAVE DESERT, CALIFORNIA: LATE CRETACEOUS MAGMATI
AUTHOR Gregory Blachly
PROGRAM Geology, M.S.

SIGNATURES

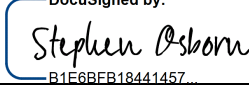
Nicholas Van Buer
Committee Chair Name
Thesis Committee Chair
Position
Geological Sciences Department
Department
Organization

DocuSigned by:

ED2E989A7B2A47B... 5/21/2021
Signature
njvanbuer@cpp.edu
Email

Jonathan Nourse
Committee Member 2 Name
Professor of Geological Sciences
Position
Geological Sciences Department
Department
Organization

DocuSigned by:

562E96F6E80E44B... 5/21/2021
Signature
janourse@cpp.edu
Email

Stephen Osborn
Committee Member 3 Name
Professor of Geological Sciences
Position
Geological Sciences Department
Department
Organization

DocuSigned by:

B1F6BFB18441457... 5/21/2021
Signature
sgosborn@cpp.edu
Email

Upload Thesis Attachment:



**THE LUDLOW BATHOLITH, CENTRAL MOJAVE DESERT, CALIFORNIA:
LATE CRETACEOUS MAGMATISM SYNCHRONOUS WITH DESTRUCTIVE
LARAMIDE EVENTS**

A Thesis

Presented to the

Faculty of

California State Polytechnic University, Pomona

In Partial Fulfillment

Of the Requirements for the Degree

Master of Science

In

Geology

By

Gregory Blachly

2021

SIGNATURE PAGE

THESIS: THE LUDLOW BATHOLITH, CENTRAL MOJAVE
DESERT, CALIFORNIA: LATE CRETACEOUS
MAGMATISM SYNCHRONOUS WITH
DESTRUCTIVE LARAMIDE EVENTS

AUTHOR: Gregory Blachly

DATE SUBMITTED: Spring 2021

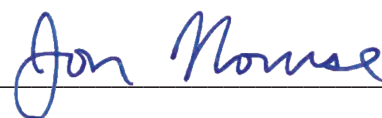
Department of Geological Sciences

Dr. Nicholas Van Buer
Thesis Committee Chair
Professor of Geological Sciences



5/14/21

Dr. Jonathan Nourse
Professor of Geological Sciences



5/6/21

Dr. Stephen Osborn
Professor of Geological Sciences



5/6/21

ACKNOWLEDGEMENTS

First and foremost, I would like to thank Dr. Van Buer for setting me up this amazing yet challenging project, and for the countless hours spent helping me to complete it. He has taught me more about geology and science than I could have imagined possible.

I would also like to thank Dr. Nourse for all the help and support on various aspects of my research, as well as Marty Grove for the personal level service given by him and others during our visit to Stanford University.

Finally, I need to thank Brianna House for driving, hiking, and getting stuck with me in the desert over and over again.

ABSTRACT

The Mojave Desert is an important section of California for geological research, as it was the first region of the western United States to experience the effects of Laramide disruption. This study looks at plutonic rocks in the vicinity of Ludlow, CA in the Mojave Desert, and focuses on one section of the Bristol Mountains where a large area of plutonic rock is exposed. Geologic mapping in the Bristol Mountains, reconnaissance sampling, U-Pb geochronology, and whole-rock compositional analysis were used to gather information into the magmatic and tectonic origins of the Bristol Mountains field site, and the associated plutonic rocks in the surrounding area. The Bristol Mountains site predominantly consists of five felsic units that range from granodiorite to granite. Also found at the site are large blobs of gabbro to the east, and mylonites that are products of a metamorphic core complex to the west. Three new U-Pb radiometric ages yield an age of 77.2 ± 1.3 Ma at the rim of the pluton, and ages of 74.9 ± 1.2 Ma and 74.6 ± 1.3 Ma in units closer to the core. From the concentric zoning and compositional variations of the five felsic Bristol Mountains units, it was determined that they are part of a large cogenetic intrusive suite referred to here as the Ludlow batholith, and that these units probably young inwards from the southeast to the northwest. Exposures of the Ludlow batholith were also found about 50 km to the southwest in the Rodman Mountains, and it is likely that about 2,000 km² of the central Mojave is underlain by a contiguous Ludlow batholith. From analysis of REEs and other trace elements, it was also revealed that Ludlow batholith is not a result of normal arc magmatism, and instead likely formed from slab-tear magmatism at the boundary of the Shatsky conjugate and Farallon Plate.

TABLE OF CONTENTS

SIGNATURE PAGE.....	ii
ACKNOWLEDGEMENTS.....	iii
ABSTRACT.....	iv
LIST OF TABLES.....	viii
LIST OF FIGURES.....	ix
INTRODUCTION	1
GEOLOGIC BACKGROUND.....	4
Proterozoic	4
Paleozoic.....	5
Triassic.....	6
Jurassic Magmatism.....	6
Cretaceous Magmatism.....	8
Properties of Cogenetic Intrusive Suites.....	12
Laramide Compression and Post-Laramide Extension.....	14
Cenozoic Magmatism and Basin and Range Extension.....	15
RESEARCH QUESTIONS.....	17
METHODS.....	18
Field Mapping.....	18
Field Site Sampling.....	20
Reconnaissance Sampling.....	20
U/Pb Geochronology and Zircons.....	21
U/Pb Geochronology Sample Preparation and Analysis.....	22

U/Pb Geochronology Spots, Runtime, and Isoplot.....	26
Whole-Rock Geochemistry.....	27
Whole-Rock Geochemistry Sample Preparation and Analysis.....	27
RESULTS.....	31
Field Map Description.....	31
Budweiser Granodiorite.....	31
Eagle Rock Granite.....	34
Brown Top Granite.....	37
Raindrop Granodiorite	38
Pink Bowl Granodiorite.....	40
Mafic Units.....	40
Description of Other Mapping Site Features.....	45
Reconnaissance Sampling.....	49
U/Pb Geochronology.....	52
Whole-Rock Major-Element Geochemistry.....	55
Trace-Element Geochemistry.....	66
DISCUSSION.....	73
Intrusions in the Bristol Mountains.....	73
Differentiation of the Bristol Mountains Intrusions.....	75
Defining the Ludlow Batholith.....	79
Rapid Melt Intrusion into the Crust.....	86
The Case for Slab-Tear Magmatism in the Central Mojave.....	89
Slab-Tear Model for the Origin of the Ludlow Batholith.....	93

CONCLUSIONS	97
REFERENCES	99
APPENDIX.....	111
U/Pb Geochronology.....	111
Cal Poly Pomona XRF Raw Data.....	114

LIST OF TABLES

Table 1: Major-Elemental Oxide Concentrations.....	56
Table 2: Trace-Element Concentrations.....	67

LIST OF FIGURES

Figure 1: Map of the Mojave Desert.....	3
Figure 2: Shatsky Conjugate (Liu, 2010)	9
Figure 3: Orientation of the Farallon Plate (Saleeby, 2003)	10
Figure 4: Geologic Maps of Other Intrusive Suites.....	13
Figure 5: Research Area.....	19
Figure 6: SHRIMP-RG Image.....	25
Figure 7: Bristol Mountains Geologic Map.....	32
Figure 8: Bristol Mountains Cross Section.....	33
Figure 9: Budweiser Granodiorite.....	35
Figure 10: Eagle Rock Granite.....	36
Figure 11: Brown Top Granite.....	39
Figure 12: Raindrop Granodiorite	39
Figure 13: Pink Bowl Granodiorite.....	41
Figure 14: Biotite Forms.....	42
Figure 15: Outcrop Images.....	43
Figure 16: Gabbro Units at Outcrop Scale.....	44
Figure 17: Gabbro and Felsic Units Contacts.....	46
Figure 18: Scattered Diorite.....	47
Figure 19: Mafic Enclaves.....	48
Figure 20: Detachment Fault.....	50
Figure 21: Mylonite.....	51
Figure 22: U-Pb Geochronology Plots.....	53

Figure 23: Zircon Grain Cathodo-Luminescence.....	54
Figure 24: Harker Plots.....	58
Figure 25: Major-Element Oxides vs. Distance Plots.....	60
Figure 26: FeO + MgO vs. Distance Plot.....	61
Figure 27: Modified Alkali-Lime Index.....	62
Figure 28: Aluminum Saturation Index vs. Alkalinity Index.....	63
Figure 29: Fe-Index.....	64
Figure 30: Quartz-Plagioclase-Alkali Feldspar Ternary Diagram.....	65
Figure 31: Nb (ppm) vs. Y (ppm).....	68
Figure 32: Ta (ppm) vs. Yb (ppm).....	69
Figure 33: La/Yb vs. Yb (ppm).....	70
Figure 34: Sr/Y vs. Y (ppm).....	71
Figure 35: Gd/Yb vs. Sr/Y.....	72
Figure 36: Outline of Ludlow Batholith.....	80
Figure 37: Possible Orientations of the Ludlow Batholith.....	85
Figure 38: Isostatic Residual Gravity Map.....	87
Figure 39: Interpretative Tectonic Diagram.....	94

INTRODUCTION

The Mojave Desert is home to rocks that represent every phase of western United States Cordilleran evolution, yet it is significantly less researched than other regions on the west coast, partially because of widespread Cenozoic cover (Fig. 1). Plutons in the Mojave Desert are particularly important features of Cordilleran geology because they are located where Laramide disruption first affected the western U.S., and where it also did the most damage to the underlying lithosphere (Fig. 2, 3). As a result of this, many plutons in the Mojave, especially those that formed synchronously with Laramide disruption, have very important stories to tell about an enigmatic time and place in the geologic past. It is also believed that normal arc magmatism cessation occurred sometime around 80 Ma in the Mojave region due to low-angle subduction of the Farallon plate that resulted from the subduction of a more buoyant oceanic plateau at the margin (Chen and Moore, 1982; Liu et al., 2010; Saleeby, 2003) (Fig 2, 3). Despite widespread termination of magmatism in the western U.S. earlier in the Cretaceous, plutons ranging in age from about 78 Ma to 72 Ma are still located throughout certain portions of the Mojave Desert and their origins are largely unknown (Howard, 2002; Needy et al., 2009) (Fig. 1). This study focuses on an area in the central Mojave Desert that (1) has not been adequately researched and is lacking in detailed geologic mapping, and (2) contains significant exposures of plutonic rocks that have unknown magmatic and tectonic origins (Fig. 1, 5, 7). The geologic history of the Mojave Desert is full of blank sections that must be filled in to obtain a complete picture of the evolution of the western United States magmatic arc, especially since the Mojave is where the colliding oceanic plateau did the most

damage, restructuring the whole lithosphere and replacing the lower part with schist (e.g., Chapman et al., 2010; Grove et al., 2003; Jacobson et al., 2011) (Fig. 1-3).

The area surrounding Ludlow, CA in the central Mojave Desert is one such region of the Mojave Desert that has not been adequately researched, yet contains ample plutonic rocks, apparently of various ages and origins (Bedford et al., 2010; Dibblee, 1964, 1966, and 1967; Dibblee and Bassett, 1966) (Fig. 1). The research area of this project is outlined by the Cady Mountains to the north, the Lava Bed Mountains to the south, the Rodman Mountains to the west, and the Bristol Mountains to the east, with Ludlow, CA in the center (Fig. 1,5). Included within this region is a well exposed area of plutonic rock in the Bristol Mountains that is the subject of geologic mapping and extensive sample analysis within this study (Fig. 5, 7). Samples were also collected from various other areas within the larger field area surrounding Ludlow, CA in order to compare them to samples found within the Bristol Mountains, and to better determine the tectonic and magmatic origins of these under-analyzed sections of rock located within this area of the central Mojave Desert. (Fig. 1, 5) This research will present new geologic mapping (Fig. 7), U/Pb geochronology ages (Fig. 22), major-element geochemical data (Fig. 24-30), and trace-element geochemical data (Fig. 31-35) from the Bristol Mountains site and from various reconnaissance sites throughout the greater research area (Fig. 5, 7). The Mojave Desert not only represents a gap in the geologic history of the western U.S., but it is also ground zero of Laramide collision where the most notable and significant damage to the lithosphere occurred (Fig. 2). Because of this, the goal of this study is to better understand the effects that the destructiveness of Laramide collision had on the Mojave Desert.

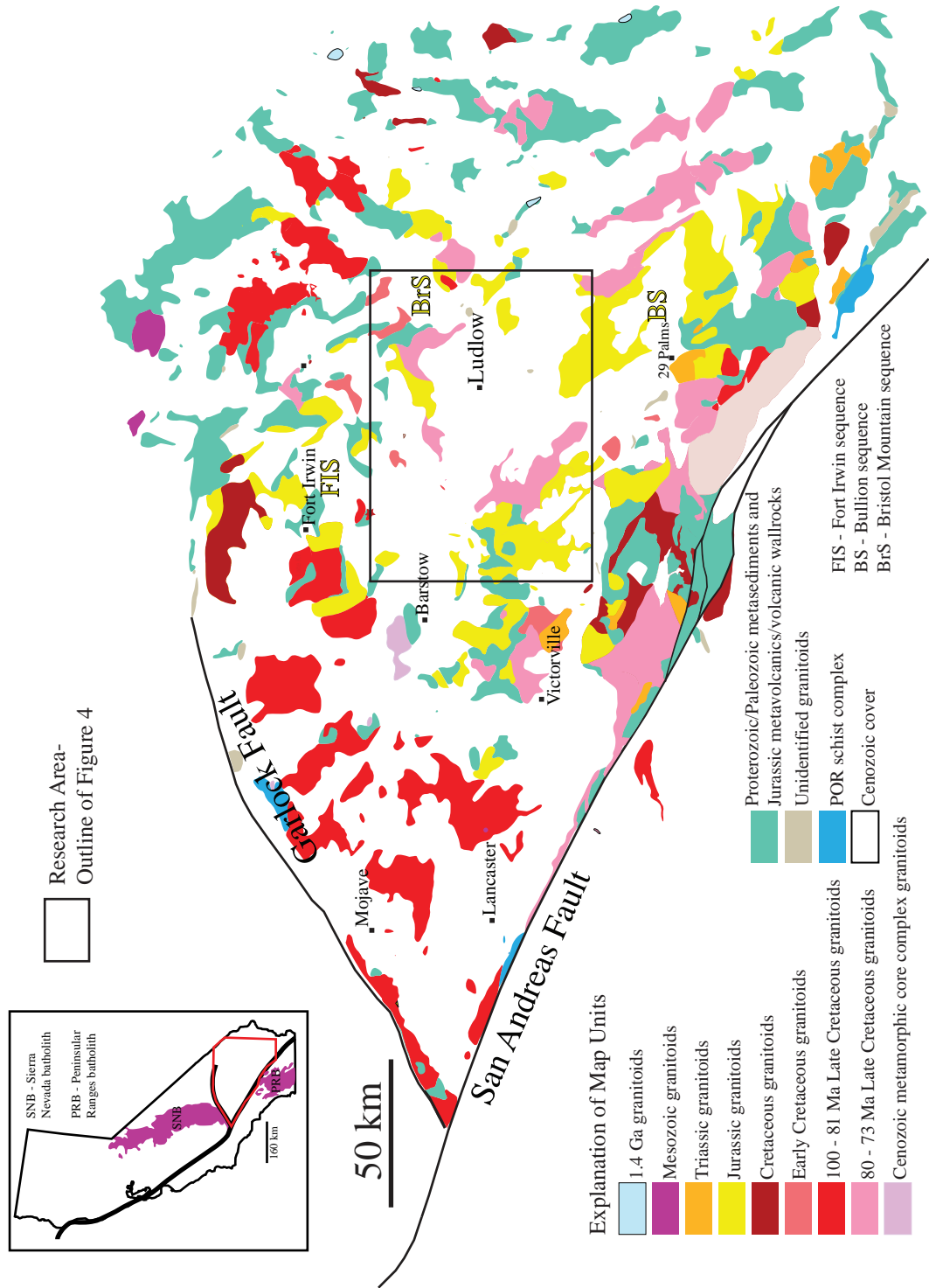


Figure 1. Map of the Mojave Desert showing the approximate locations and ages of plutons. The square surrounding Ludlow, CA represents the area of study, better shown in figure 5. Modified from Van Buer, in prep.

GEOLOGIC BACKGROUND

Proterozoic

The Proterozoic Mojave Desert region experienced several complex plutonic events between 1.76 and 1.64 Ga (Strickland et al., 2013; Wooden and Miller, 1990). Magmatism initiated around 1.76 Ga when a pre-orogenic magmatic suite began to intrude supracrustal metasedimentary gneisses that were originally deposited about 1.79-1.75 Ga. The oldest supracrustal rocks of the Mojave Desert contain inherited zircon grains over 2.0 Ga, but the protolith of these zircons is not known. The initial 1.76 Ga pre-orogenic magmatic pulse has a calc-alkalic affinity and has been interpreted as forming in an arc setting on or adjacent to a continent (Strickland et al., 2013; Wooden and Miller, 1990). Between 1.71 and 1.69 Ga, the Mojave Desert was part of a significant, regionally extensive deformation event known as the Ivanpah Orogeny (Wooden and Miller, 1990). This event generated a large volume of granitoids in the Mojave region, and metamorphosed supracrustal and pre-orogenic plutons in the region to granulite and upper amphibolite facies (Wooden and Miller, 1990). Granitoids resulting from the Ivanpah orogeny are similar in nature to pre-orogenic granitoids in the sense that they also represent calc-alkaline magmatism in an arc related setting (Wooden and Miller, 1990). Post-orogenic, 1.69–1.65 Ga granitic plutons, which are also prevalent in the Mojave, likely represent a shift in the tectonic setting of the southwestern portion of North America at the time. When compared to pre-orogenic and syn-orogenic granites, post-orogenic granites represent more potassic, A-type granitic melts (Barth et al., 2009; Wooden and Miller, 1990). The change from calc-alkaline magmatism to this more

evolved, potassic magmatism may signify a shift from a period of crustal formation in the Mojave region to a period of crustal stabilization (Strickland et al., 2013).

Between 1.5 and 1.4 Ga, North America entered a period of localized extension and continent-wide intrusion of crustal-derived anorogenic granitoids that were emplaced into the upper crust (Anderson and Bender, 1989). Magmatism responsible for the origin of these anorogenic granites is related to heating of an undepleted mantle, and the rise of mantle plumes into the undifferentiated Proterozoic crust (Anderson and Bender, 1989). These granitoids now lie beneath a large portion of the mountain ranges in the southwestern United States, and can be found in various locations in Arizona, southern Nevada, and the eastern Mojave Desert. The anorogenic suite of granitoids in southern California is marginally metaluminous, bearing biotite and sphene \pm hornblende and fluorite, is more potassic, iron-enriched and depleted in Ca, Mg, and Sr in contrast to typical orogenic granitoids, and has a large-ion-lithophile-element enriched composition (Anderson and Bender, 1989).

Paleozoic

Scattered Paleozoic strata unconformably overlay the Proterozoic basement but are only exposed locally throughout the Mojave Desert as metasedimentary wall rocks (Stone et al., 1983). Most of these exposed strata are deformed and metamorphosed, especially when in contact with Mesozoic plutons (Stone et al., 1983). There are no identified Paleozoic outcrops within the research area surrounding Ludlow, CA, but they are known to exist nearby to the south in the southern Bristol Mountains, and to the northeast in the Providence Mountains (Stone et al., 1983).

Triassic

The onset of Triassic magmatism reflects a shift from a passive to convergent margin in Western North America (Burchfiel and Davis, 1975; DeCelles, 2004; Miller, 1978; Yonkee and Weil, 2015). Triassic Mojave plutons mark the beginning of arc magmatism related to the east-directed subduction of the Farallon plate, beneath the North American plate, which initiated in the latest Permian and continued into the Cretaceous (Miller, 1978). Permian-Triassic arc magmatism is believed to have begun at about 275 Ma in the northern Mojave's Deserts El Paso terrain, which at the time was the southwestern Laurentian margin (Cecil et al., 2018). Magmatism then extended north and south into the areas that are now the Sierra Nevada and the Peninsular ranges and continued until 240 Ma (Cecil et al., 2018). Triassic plutons are primarily characterized as intermediate to felsic, calcic to calc-alkalic, and as having chemistries consistent with magmatism in an arc setting (Cecil et al., 2018). Although they signify an important shift in the tectonics of the region, Triassic plutons throughout the Mojave Desert are scarce when compared to younger Mesozoic plutons.

Jurassic Magmatism

Formed by the continued oblique subduction of the Farallon plate beneath the North American plate that initiated during the Permian, the Jurassic magmatic arc was once continuous from Sierra Nevada, through the Mojave, and into the Peninsular ranges (Miller and Glazner; 1995, Schermer and Busby, 1994). This second pulse of arc magmatism commenced in the central and eastern Mojave during the Early Jurassic, with the emplacement of plutons at 183 Ma and 181 Ma (Barth et al., 2016). Once initiated, Jurassic magmatism in the southwestern U.S. Cordillera was voluminous and melt

production increased until it reached a peak ca. 161 Ma, at which point melt production decreased over time and the arc began migrating westward (Barth et al., 2016). In the central and eastern Mojave Desert, the Fort Irwin sequence and the Bullion sequence represent older, Early to early Middle Jurassic magmatism, and are both high-K calc-alkalic rock suites (Barth et al., 2016) (Fig. 1). Late Jurassic magmatism, which is illustrative of a period of waning melt production, is best represented in the central and eastern Mojave Desert by the Bristol Mountains sequence that is dated to 164-161 Ma in areas of the southern Bristol Mountains, the Lava Hills, the south Providence Mountains, and the Colton Hills (Barth et al., 2016; Fox and Miller, 1990) (Fig. 1). This sequence of Jurassic plutons consists of subalkaline diorite and monzodiorite, metaluminous to weakly peraluminous granite, and other mixed plutonic rocks. Compared to the older Fort Irwin and Bullion sequences, the Bristol Mountains sequence is relatively LILE-enriched, shoshonitic, and alkali-calcic, indicating a shift in magmatic composition over time during the Jurassic (Barth et al., 2016; Fox and Miller, 1990). The areas used to define the Bristol Mountain sequence are located nearby, but to the northeast and southeast of the Ludlow batholith and the research area of this study (Fig. 1).

In the Mojave region, Jurassic magmatism may have terminated as late as 146 Ma (Tosdal and Wooden, 2015) and was then followed by a period of approximately 26 m.y. where no granitic intrusions were emplaced east of the Sierra Nevada or in the Mojave (Chen and Moore, 1982). Overall, Jurassic magmatism in the Mojave is represented by many different rock types ranging from gabbro to granite, and marks a magmatic transition from older, mafic to more felsic, calcic-alkaline rocks like those seen in the late Cretaceous (Barth et al., 2008).

Cretaceous Magmatism

At about 120 Ma, emplacement of mid Cretaceous granitic plutons began and was followed by steady eastward migration of arc magmatism (Chen and Moore, 1982). This eastward migration of magmatism is related to the flattening of the subduction zone, which results in an eastward migration of the position of the mantle wedge responsible for producing melts associated with arc magmatism (Chen and Moore, 1982). The initial cause of eastward arc migration and the flattening of the subduction angle is not fully known. At 90 Ma, an oceanic plateau, known as the Shatsky conjugate, within the Farallon plate began to subduct beneath the North American plate and resulted in this period of increased flat slab subduction and further eastward migration of magmatism (Liu et al., 2010; Saleeby, 2003) (Fig. 2, 3). Large-volume magmatism of both the Sierra Nevada batholith and Southern California batholith ceased at about 85 Ma, at which point magmatism migrated hundreds of kilometers inland (Liu et al., 2010). Mid-to-late Cretaceous (100-81 Ma) plutonic rocks represent the late stage of normal arc magmatism, which ultimately ceases in most of the Mojave Desert at 80 Ma (Needy et al., 2009). In the Mojave, Late Cretaceous plutonic rocks range from calcic to alkali-calcic and have silica content ranges from 53% to 76.8 % (Vermillion et al., in prep). Although arc magmatism cessation occurs at 80 Ma due to increasingly low angle subduction linked to subduction of the Shatsky conjugate, Late Cretaceous magmatism however continued between 80 Ma and 72 Ma in certain areas of the Mojave when normal arc magmatism had already ceased throughout most of the Cordillera (Needy et al., 2009). More specifically the areas with 80-72 Ma plutons include the eastern Transverse Ranges, the Cadiz Valley batholith (Howard, 2002; Needy et al., 2009) and the Ludlow batholith

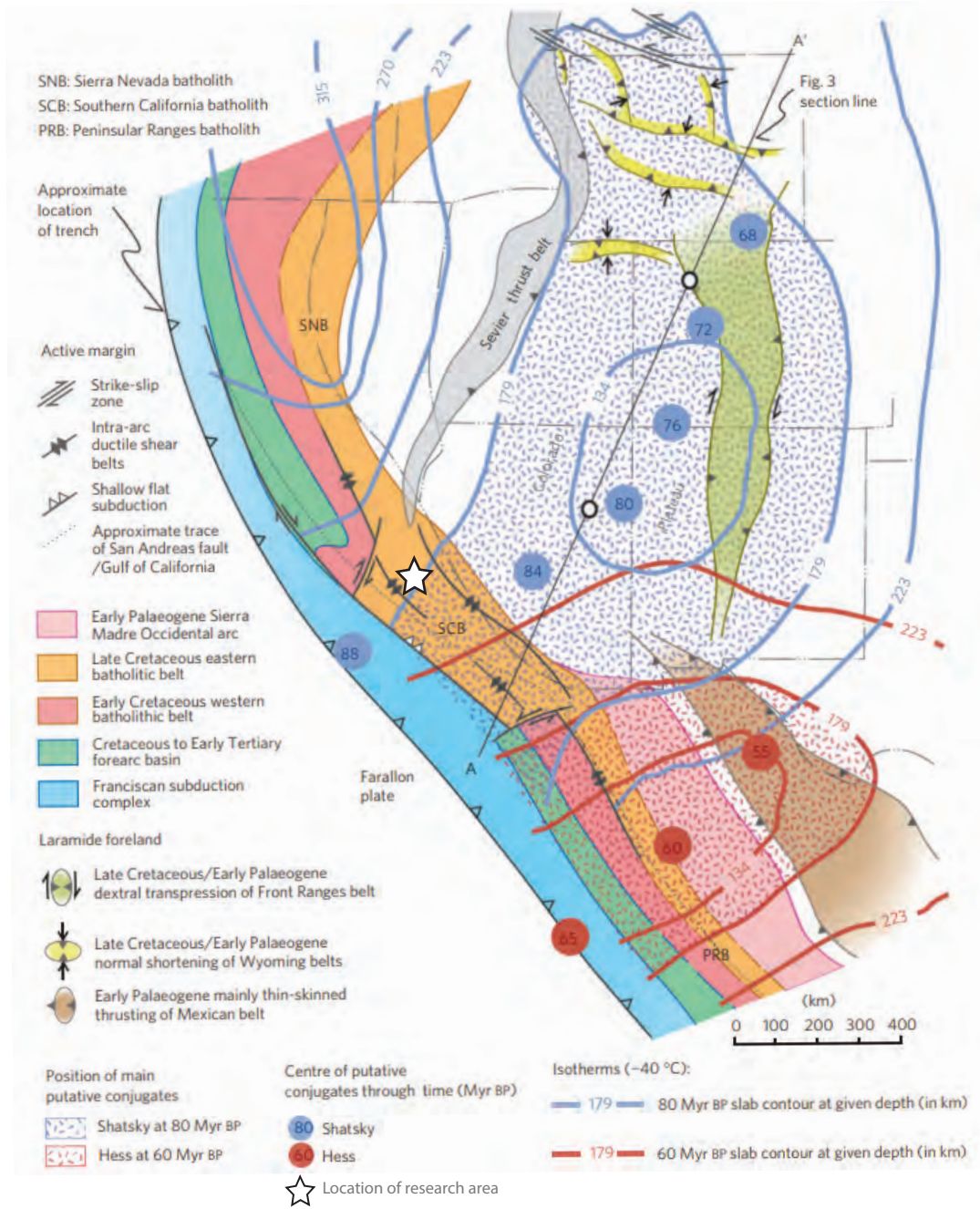
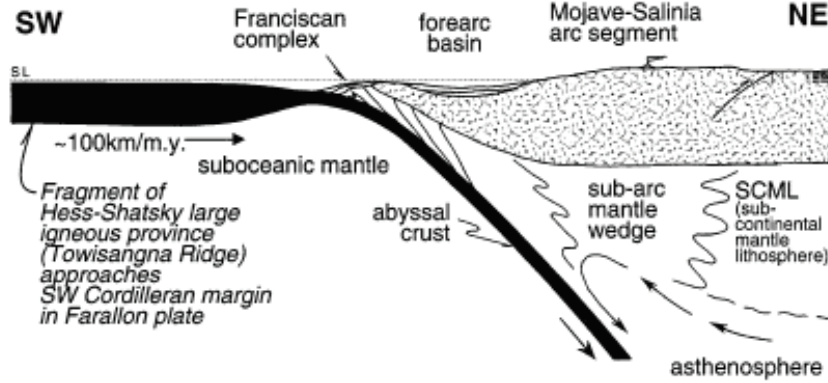
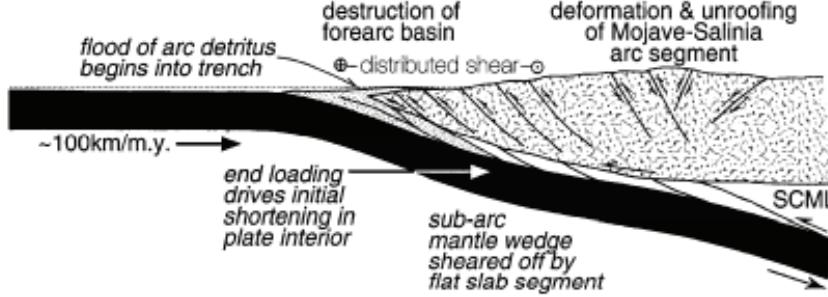


Figure 2. Reconstructed map of the western United States indicating the locations of the Hess and Shatsky conjugates through time. The blue circles represent the position of the center of the Shatsky conjugate during the time represented by the age (Ma) in the middle of the circle. Modified from Liu et al., 2010.

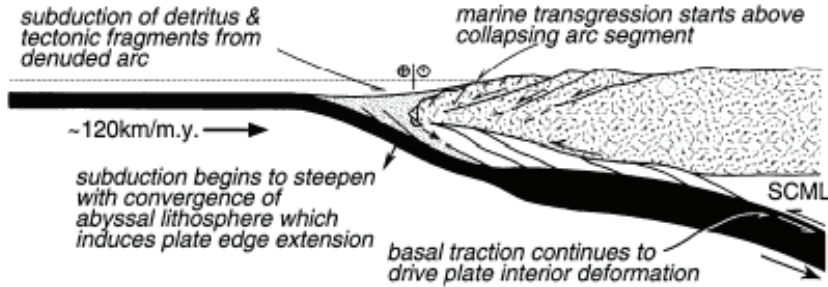
A. 90-85 Ma: Just prior to slab segmentation



B. ca.80 Ma: Laramide shallow slab segment subduction



C. ca.70 Ma: Extensional collapse starts in wake of shallow slab segment



D. ca.60 Ma: Plate edge orogen collapsed above steepened slab

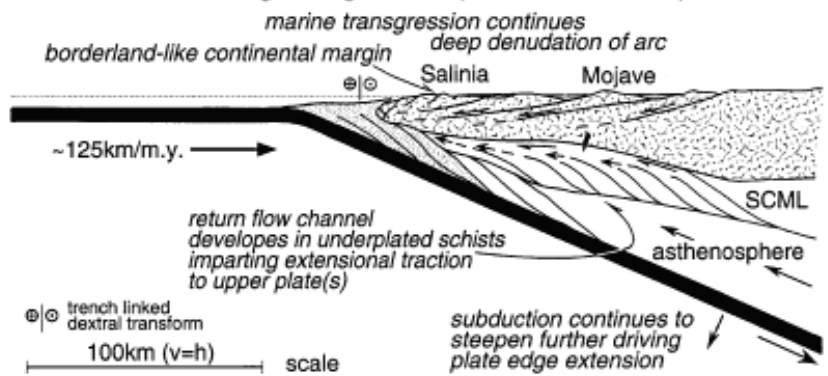


Figure 3. Diagram showing the changing subduction angle of the Farallon plate and the orientation of the Hess-Shatsky large igneous province over time. From Saleeby, 2003.

described in this study. Additionally, there are a few areas in the eastern Mojave containing plutons of this age, as well as some other small and scattered areas throughout the Mojave.

In the central and eastern Mojave, Mesozoic plutons were emplaced into two distinct bedrock types. Plutons in the northern section of the eastern Mojave were emplaced into Paleozoic metasedimentary strata of eugeoclinal affinity, while plutons in the southern section of this region were emplaced into Neoproterozoic and Paleozoic miogeoclinal-cratonal strata and their Paleoproterozoic gneissic substrate which was once the old Laurentian craton edge (Stewart and Poole, 1975; Stone and Stevens, 1988; Martin and Walker, 1992; Walker et al., 2002). The Bristol Mountains and, more specifically, the area of this study, are located within the southern section of the eastern Mojave and therefore the Jurassic and Cretaceous plutons that dominate the region were likely impacted by the Neoproterozoic and Paleozoic miogeoclinal-cratonal strata and their Paleoproterozoic gneissic substrate that it was emplaced into.

Only minimal research has been done on the rocks in the proposed area of the Ludlow batholith prior to this study. Previous mapping and U/Pb geochronology data of the Bristol Mountains site (that is the focus of this study) is presented by Hess (2017) and suggests that the Late Cretaceous pluton in question was emplaced at about 75 Ma (Fig. 7). It should be noted that Hess (2017) does not thoroughly map out plutonic subunits or present any geochemical data. Three U/Pb zircon ages from Hess (2017) are added to the detailed geologic map shown in this study (Fig. 7), and other relevant information is used to help form the conclusions presented herein.

Properties of Cogenetic Intrusive Suites

Many large intrusive suites were emplaced near the end of Late Cretaceous arc magmatism and many cogenetic intrusive complexes also share common traits that suggests they are products of similar geologic processes. These common traits can also aid in identifying whether a newly studied plutonic body can be considered part of a cogenetic intrusive suite. Several intrusive suites of the Sierra Nevada batholith, such as the Tuolumne, Whitney, and Sahwave intrusive suites, have been studied in detail and therefore are good examples of Cretaceous intrusive complexes in the Cordilleran region that share common properties, and that can be used as analogs to other intrusive suites. All three of the zoned plutons mentioned above (as well as most others) have younger units nested with older ones, relatively mafic outer units with equigranular textures, and felsic inner units that contain K-feldspar megacrysts (Bateman, 1992; Coleman et al., 2004; Hirt, 2007; Van Buer and Miller, 2010) (Fig. 4). More specifically, most intrusive suites have mafic granodiorite outer intrusions that grade progressively inward to granodiorite or granite cores and increase in silica content from rim to core (Bateman, 1992; Coleman et al., 2004; Hirt, 2007; Van Buer and Miller, 2010) (Fig. 4). Another common characteristic is the steep dip angles of both the internal and external unit contacts throughout a zoned intrusion, as seen in both the Whitney and Sahwave intrusive suites (Hirt, 2007; Van Buer and Miller; 2010) (Fig. 4). Outer units have also been noted to have high percentages of contact-aligned mafic enclaves, while enclaves within inner units are far less abundant (Coleman et al., 2004; Hirt, 2007; Van Buer and Miller, 2010).

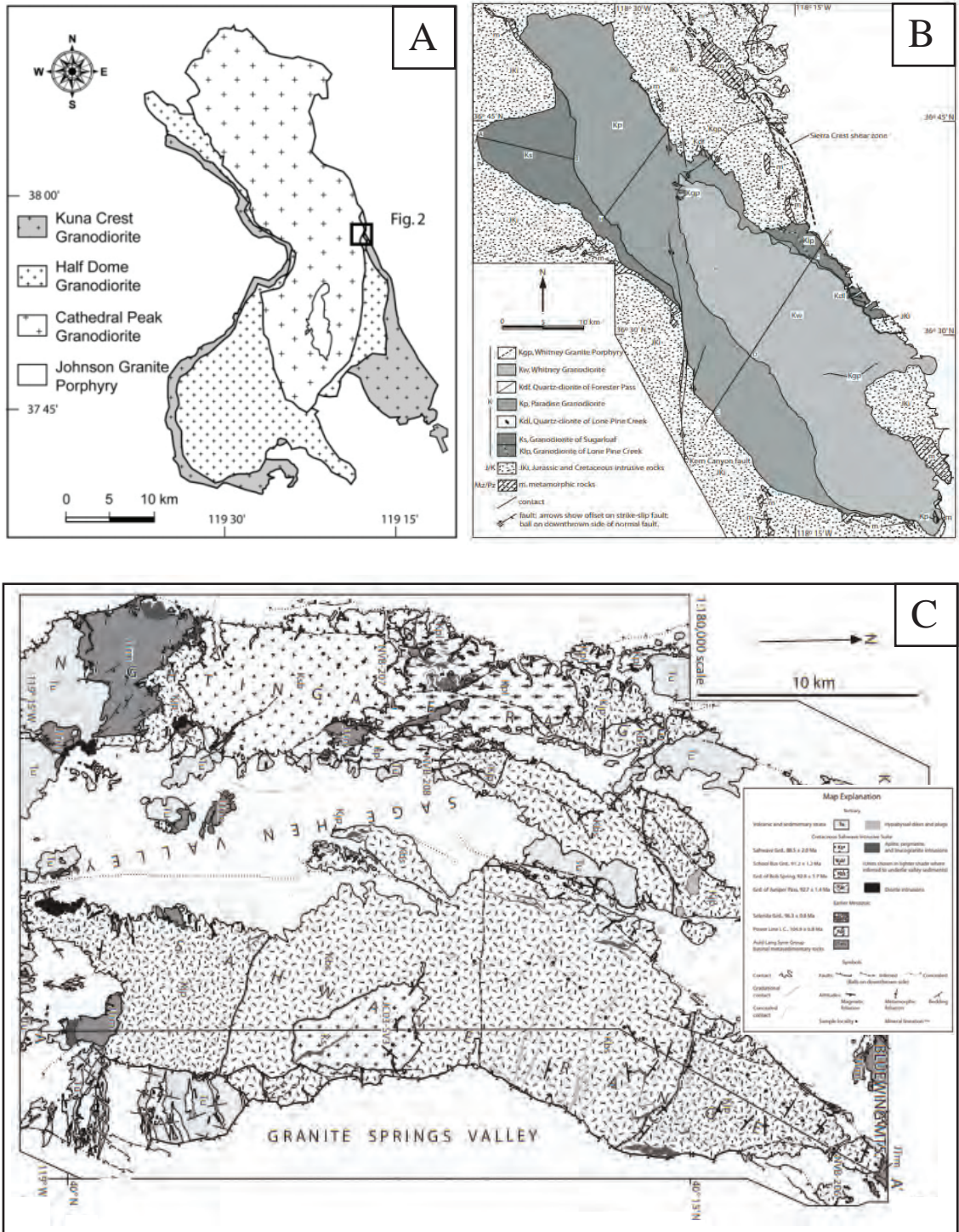


Figure 4. Geologic maps of (A) the Tuolumne, (B) the Whitney, and (C) the Sahwawe intrusive suites from the Sierra Nevada batholith. Figures are from (A) Coleman et al., 2004, (B) Hirt, 2007, and (C) Van Buer and Miller, 2010.

Laramide Compression and Post-Laramide Extension

Low angle subduction of the Farallon plate beneath the North American plate not only contributed to the cessation of magmatism during the Late Cretaceous, but also produced compressional and extensional events in the western United States (Fig. 3). The compressional events caused by the initial low-angle subduction of the Farallon plate and oceanic plateau are known as the Laramide orogeny, which began at approximately 80 Ma and continued until approximately 35 Ma as deformation migrated NE towards the continental interior (Liu et al., 2010; Livaccari, 1991; Saleeby, 2003) (Fig. 2, 3). Initial Laramide compressional events were responsible for the forearc destruction, intra-arc ductile thrusting, and rapid exhumation of the south Sierra Nevada batholith that occurred closer to the margin (Jacobson et al., 2011; Saleeby, 2003) (Fig. 3). Compression during the Laramide triggered cessation of magmatism during the Late Cretaceous by shut-off asthenospheric flow beneath the western margin of the North American plate and led to the shearing off of the upper mantle in the southern Sierra Nevada, the Mojave region, and the northern Peninsular ranges, which was then followed by underplating of schists derived from Franciscan subduction complexes (Chapman et al., 2010; Grove et al., 2003; Jacobson et al., 2011; Saleeby, 2003) (Fig. 3). At 70 Ma, the angle of subduction of the Farallon plate beneath the North American plate began to steepen, compressional forces started to subside, and extensional forces began to dominate the western United States (Fig. 3). This episode of widespread extensional collapse of the recently thickened crust affected the Southern Cordillera immediately after Laramide compressional events at 70 Ma and continued at more inland locations as late as 35 Ma (Chapman et al., 2010; Livaccari, 1991; Saleeby, 2003; Wood and Saleeby, 1997) (Fig. 3).

Hess (2017) describes a mylonitic shear zone in the Bristol Mountains that records a top-to-the-SW, down-dip, non-coaxial sense of shear, and suggests that the shear zone recorded deformation temperatures at upper greenschist to lower amphibolite conditions (~350 to ~550 °C). $^{40}\text{Ar}/^{39}\text{Ar}$ thermochronology data suggests that the pluton cooled below K-feldspar MDD small domain closure temperatures by about 65 Ma, and continued to cool at rates of about 22 °C/m.y. in the footwall and about 16 °C/m.y. in the shear zone as a result of the Laramide extensional event (Hess, 2017).

Cenozoic Magmatism and Basin and Range Extension

After Laramide disruption, asthenospheric flow eventually reignited beneath the North American plate due to the continued easing of compressional forces, which also led to the development of the basin and range extensional province (Coney and Harms, 1984; Constensius, 1992; Glazner et al., 2002). Basin and range extension was characterized by the development of metamorphic core complexes and bimodal volcanism that initiated to the north and south around 45 Ma but converged in southern Nevada by approximately 15 Ma (Coney and Harms, 1984; Constensius, 1992). The Mojave Desert during this time was experiencing a northwest sweep of volcanism out of Arizona that was accompanied by extensional faulting (Glazner et al., 2002). A large portion of the central Mojave Desert has also been tectonically rotated over the course of two separate Miocene clockwise crustal rotational events (Glazner et al., 2002; Luyendyk, 1991; Ross et al., 1989; Wells and Hillhouse, 1989). The first clockwise rotational event occurred in the early Miocene and is linked to widespread north-south crustal extension that was taking place throughout southern California during basin and range extension (Glazner et al., 2002; Luyendyk, 1991; Ross et al., 1989). In the middle Miocene, basin and range

extension ceased, and deformation shifted from extensional faulting to predominantly strike-slip faulting along northwest-striking dextral faults and west-striking sinistral faults which further contributed to the tectonic clockwise rotation (Glazner et al., 2002; Luyendyk, 1991; Ross et al., 1989). Large strike-slip faults can be found throughout the central Mojave from Barstow to east of Ludlow, and significant clockwise rotations of up to 50° have been documented throughout the region (Glazner et al., 2002; Luyendyk, 1991; Ross et al., 1989; Wells and Hillhouse, 1989).

The greater study area surrounding Ludlow, CA described in this study (Fig. 1, 5) has been widely affected by Cenozoic processes, and portions of the area are overlain by significant Cenozoic volcanism. Glazner (1988 and 2000) describes various aspects of the Cady Mountains and Rodman Mountains, both of which are located within the area where reconnaissance sampling was conducted for this study (Fig. 5). The Sleeping Beauty area of the southern Cady Mountains records volcanism, extensional faulting, and potassic metasomatism during a time of tectonic transition between 20 and 18.5 Ma (Glazner 1988) (Fig. 5). The Rodman mountains are in the southwest section of the research area for this study, and several of the reconnaissance samples were collected in or around them (Fig. 5). These mountains are home to the Silver Belt fault that is surrounded by 1.9 km of Tertiary mafic lava flows on the northern side of the fault, which are overlain by and intercalated with coarse clastic rocks that have been derived from the south side of the fault (Glazner, 2000).

RESEARCH QUESTIONS

The research questions to be addressed in this thesis are as follows:

- 1) Are granitoid outcrops in this area part of a massive cogenetic suite, or are they part of disparate and unrelated magmatic events?
- 2) What is the age, or range of ages, of the intrusive suite?
- 3) How did the intrusive suite differentiate?
- 4) What is the tectonic and magmatic origin of the intrusive suite?

METHODS

Field Mapping

The research area surrounding Ludlow, CA contains areas of outcropping rocks that are broadly granitic and visually similar to Late Cretaceous plutonic rocks elsewhere in the Mojave Desert (Fig. 1, 5). Of these apparently similar areas, an area of about 40 square kilometers in the Bristol Mountains was chosen for detailed mapping at the scale of 1:24000 using a USGS 24K topographic map as a base map (Fig. 7). This area has been studied and mapped previously by Hess, 2017, but that study did not focus on magmatic variations within the intrusive suite. This site was specifically chosen for mapping because the rock outcrops are well exposed, are composed predominantly of light-colored granitoids similar in appearance to late Cretaceous plutonic rocks elsewhere in the Mojave, and the site is accessible (Fig. 1, 7). The rock units mapped were defined based on texture and mineral composition (Fig. 9-13), and emphasis in mapping was placed on the plutonic rocks at the site (Fig. 7). Other metamorphic and mylonitic rock types are found at the site, but they are not as directly relevant to this study (Fig. 20, 21). Field mapping is also essential for effectively choosing sampling locations for U/Pb geochronology and whole-rock compositional analysis (Fig. 7).

The field site is located approximately 14 miles from Ludlow, CA and sandy terrain can make the site slightly difficult to access without a four-wheel drive vehicle, although it has been done several times (Fig. 5). It is recommended to bring a good shovel along when travelling on these roads. From the dirt road south of the field site, it is a two-to-three-mile hike to reach the site itself, and terrain is rugged and mountainous throughout most of it. Satellite imagery was used in part to map units inaccessible on

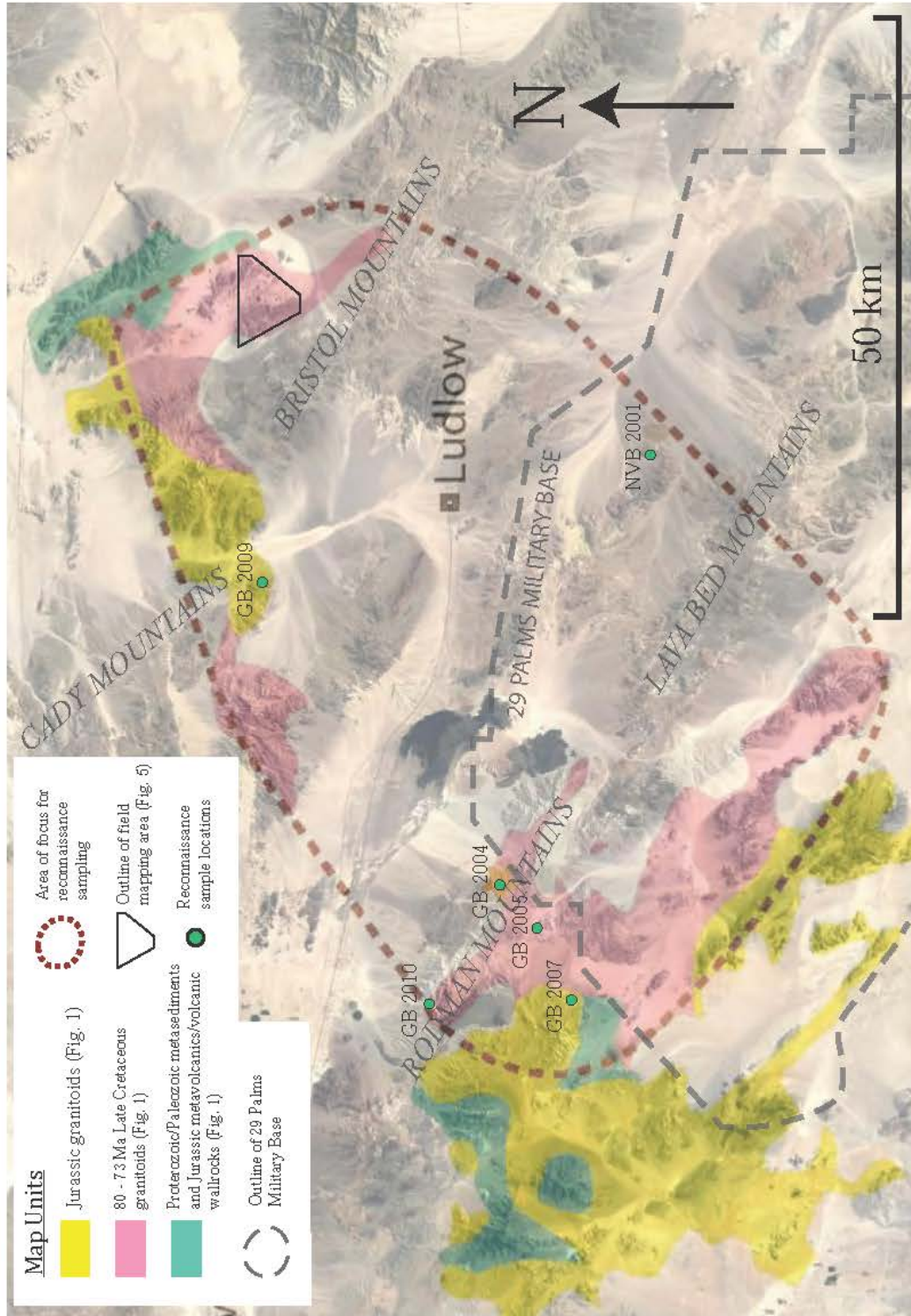


Figure 5. Research area outlined in figure 1. The black line outlines the field mapping location that is depicted in figure 7. The dashed red line surrounds the area where possible samples related to the rocks in the field mapping area were initially searched for. Colored blobs indicating pluton ages are taken from Van Buer, in prep.

steep mountain sides, and to aid in determining paths of least resistance while navigating through the field site (Fig. 7). Mapping was predominantly done using a paper base map and a GPS phone app. The geologic map was digitized using Adobe Illustrator (Fig. 7).

Field Site Sampling

To address the research questions, samples at the mapping site were collected for U/Pb geochronology and whole rock geochemistry. For U/Pb geochronology, one sample was collected from each of the mapped plutonic units to determine an age for these units (Fig. 7, 22). Eleven samples along a 5.5 km transect were collected for whole-rock major element compositional analysis (Fig. 7, 24-30). This transect runs perpendicular to the interplutonic contacts at the site and goes through all five major mapping units (Fig. 7, 25, 26). Eleven samples are evenly spread along this transect, about 500 m apart (Fig. 7). Unfortunately, due to limited laboratory access resulting from the COVID-19 pandemic, ages have only been determined for three out of five samples collected for geochronology (Fig. 7, 22), and geochemical data has been determined for nine of the eleven samples collected along the transect (Fig. 7, 24-30). Still, at least one sample from each of the five mapping units was analyzed for whole-rock major and trace-element geochemistry (Fig. 7, 24-35).

Reconnaissance Sampling

Reconnaissance sampling also took place outside of the smaller mapping site, in the greater area surrounding Ludlow, CA (Fig. 5). Sampling sites were chosen from an area of about 4000 square kilometers, where rock units that are visually similar and possibly cogenetically related to the Bristol Mountain units are located (Fig. 5). Possible sampling locations were preliminarily chosen on Google Earth based on likeliness in

color to the Bristol Mountain units. While visiting the reconnaissance locations, samples were collected from sites found to be mineralogically and texturally like the mapped units in the Bristol mountains (Fig. 5). Six samples mineralogically and texturally similar to the major mapping units in the Bristol mountains, were collected for whole rock geochemistry (Fig. 5). All six of these samples were selected for whole-rock major and trace-element analysis (Fig. 5, 24, 27-35).

U/Pb Geochronology and Zircons

U/Pb geochronology utilizes the decay of radioactive U and Th isotopes in rocks to determine ages of crystallization. ^{238}U , ^{235}U , and ^{232}Th are radioactive parent isotopes that decay to stable Pb isotopes and follow unique decay series. ^{238}U decays to ^{206}Pb with a half-life of 4.468 Ga, ^{235}U decays to ^{207}Pb with a half-life of 703.8 Ma, and ^{232}Th decays to ^{208}Pb with a half-life of 14.01 Ga. ^{206}Pb , ^{207}Pb , and ^{208}Pb are all stable and radiogenic isotopes, and therefore only exist in significant amounts as results of these radioactive decays, unlike ^{204}Pb which is entirely primordial and does not form by radioactive decay. The isotopic ratios $^{238}\text{U}/^{206}\text{Pb}$ and $^{235}\text{U}/^{207}\text{Pb}$ are used to determine the age of the zircon grain in a sample. When these isotopic ratios agree on an age, they will plot on the concordia line. When the $^{238}\text{U}/^{206}\text{Pb}$ and $^{235}\text{U}/^{207}\text{Pb}$ isotopic ratios plot on the concordia line, and therefore yield the same age, the zircon grains are presumed to have remained a closed system since crystallization and the sample is said to be concordant. Samples are discordant when $^{238}\text{U}/^{206}\text{Pb}$ and $^{235}\text{U}/^{207}\text{Pb}$ isotopic ratios do not produce the same age. Discordance can occur when the zircons have had their crystal lattices damaged or recrystallized by either radiation damage or a significant metamorphic event, and therefore have become an open system since crystallization; or when spots represent

a mixture of areas with different ages. During this sort of open system behavior, lead diffuses out of the zircon grains and thus some radiogenic daughter isotopes from the decay of uranium and thorium are lost. When the isotopic ratios of a discordant sample are plotted, a discordia line is created. Concordant samples are most ideal for determining the age of rock units.

The U/Pb dating method is applied to zircon crystals because the crystal lattice of zircon incorporates both uranium and thorium, but strongly rejects lead. The chemical formula of zircon is $ZrSiO_4$. Zirconium, uranium, and thorium all commonly take oxidation states of +4, allowing for substitution of uranium and thorium for zirconium in the crystal lattice. The most common oxidation state of lead is +2, making it a larger ion that will not fit in the crystal lattice in place of zirconium. When zircons yield concordant ages, it can often be assumed that they contained no initial lead, and all measured lead is a radiogenic and a result of the decay of uranium and thorium. Although zircon is in relatively low abundance in a granitoid rock when compared to other minerals, zircon's low magnetic susceptibility and high density makes separation and preparation of a pure zircon sample viable.

U/Pb Geochronology Sample Preparation and Analysis

Preparation of zircon grains for U-Pb geochronology was conducted at Cal Poly Pomona in the rock preparation and mineral separation lab. To begin preparing zircon grains for analysis using mass spectrometry, samples collected in the field are placed on a metal plate and crushed to < 1 cm chip size using a sledgehammer. Chips are pulverized using a disc mill, with the two grinding disks are separated by a 0.3 mm gap. The 0.3 mm gap is big enough to let whole zircon grains into the collection pan, but small enough that

only individual mineral grains will make it through. Once the sample has been pulverized into individual mineral grains, the sample is run through a Gemeni water table to concentrate dense zircon grains into grooves in the table. Once they are caught in a groove on the table, zircons are less likely to be forced out than many of the other lower density mineral grains. While running each sample, the water table is constantly shaking, and flowing water is forcing the individual mineral grains down the table. Samples are run on the table until most of the material is either forced off the end of the table or is collected in one of the grooves in the table. Once the water has stopped flowing and the shaking mechanism has been turned off, the material that has been collected at the end of each groove is collected with a disposable pipette and transferred to a vial. Collecting the material at the end of the grooves is an effective way to separate a significant amount of zircon grains from the rest of the bulk sample. The collected zircon grains and the rest of the material collected from the grooves on the water table are then treated overnight with vinegar in order to remove any rust that has formed on the surface of the mineral grains. After rinsing several times with deionized water and drying under a heat lamp, the samples are further separated from other mineral grains using a Frantz isodynamic magnetic separator. The Frantz consists of one ramp that splits into two. There is a strong magnetic field that reaches a maximum between the two ramps, such that only nonmagnetic material can fall downhill through the magnetic field to reach the lower ramp. Varying the electric current through the Frantz changes the strength of the magnetic field. Samples are run through the ramp at four different amperages to separate magnetic materials in the sample from the nonmagnetic zircon grains. After running the sample through the Frantz at 0.4, 0.8, 1.2, and 1.6 A, the zircon grains are collected at the

end of the nonmagnetic ramp after the fourth run at 1.6 A. Individual zircon grains are picked out of the collected nonmagnetic material using a binocular microscope and placed on double-sided tape on a glass slide. For each sample, between 40 and 60 zircon grains are picked and placed in rows on designated sections of the double-sided tape. A map of the glass slide and double-sided tape is also created to keep track of zircon grain locations for each sample on the slide. Each slide holds zircons from up to six samples and zircon standards of known ages. The grains are then mounted in epoxy, which is left to harden.

Cathodo-luminescence (CL) images of each sample were taken using the scanning electron microscope at the Cal Poly Pomona, College of Engineering Advanced Imaging Laboratory (Fig. 23). CL images reveal the zonation within the zircon grains, and aid in identification of older cores within the zircon grains (Fig. 23). These detailed CL images provide valuable information about the zircon grains and aid in spot selection on the mass spectrometer (Fig. 23).

Zircon U/Pb analyses were conducted at the SHRIMP-RG laboratory at Stanford University. The lab is cooperatively managed by Stanford University and the U.S. Geological Survey and houses a Sensitive High-Resolution Ion Microprobe-Reverse Geometry (SHRIMP-RG) (Fig. 6). The SHRIMP-RG is a double-focusing secondary ion mass spectrometer (SIMS) that consists of an electrostatic analyzer (ESA) and a magnetic sector. The SHRIMP-RG uses a beam of primary oxygen ions to create and sputter secondary ions from the zircon grains into the mass spectrometer (Fig. 6). These secondary ions then travel through ion optics, which focus the scattered secondary ions into a beam that is directed towards the magnetic sector and the electrostatic analyzer in

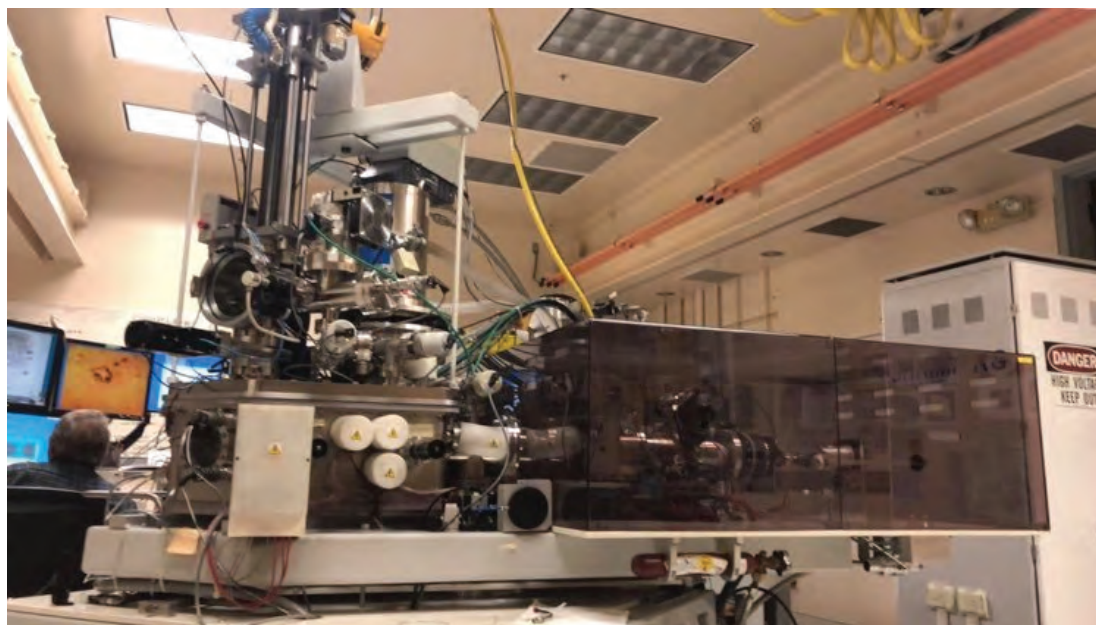


Figure 6. Image of a segment of the Sensitive High Resolution Ion Microprobe-Reverse Geometry (SHRIMP-RG) housed at Stanford University. The primary ion beam source is located in the black box, the sample chamber can be seen on the left, and the secondary ions travel away from the viewer through part of the machine not visible in the photograph.

the mass spectrometer (Fig. 6). The magnet then proceeds to alter the path of the secondary ions based on the weight of the ions, which creates a beam of secondary ions has been filtered based on the mass of the individual ions (Fig. 6). Heavier secondary ions will take a wider path when traveling through the magnetic sector, while lighter ions will take a shorter path through the sector, and thus the ions will become spatially separated ion beams, based on mass. The filtered beam then proceeds to enter the ESA which refocuses the dispersed secondary ions into a singular beam and reverses the angular trajectories and velocity dispersion of the ions created by the magnet. The ion beam then passes into a collector which detects abundance of the ionic/molecular species for the Pb, U, and Th isotopes present (Fig. 6).

U/Pb Geochronology Spots, Runtime, and Isoplot

Primary ion beam spots were chosen for each zircon grain with the assistance of the CL images that have been taken of each sample and standards (Fig. 23). These CL images aid in the distinction of rims and cores in the zircon grains and allow for proper placement of spots to hit each zircon grain with the ion beam (Fig. 23). Typical spots generated by the SHRIMP-RG primary ion-microprobe are 25 microns wide and between 1 and 5 microns deep, which is shallower than the pits created using other techniques such as laser ablation (Fig. 23). Therefore, the volume of material analyzed using ion-microprobe analyses is orders of magnitude smaller than the material analyses using laser ablation techniques. Each spot analysis on the SHRIMP-RG takes approximately 10 to 20 minutes and each sample contains between 11 or 12 spots. Concordia diagrams and best-fit age plots are generated using Isoplot (Vermeesch, 2018) (Fig. 22).

Whole-Rock Geochemistry

Analysis of the chemical composition of samples is necessary for answering the research questions presented in this study. Determining the elemental and mineralogical composition of rocks aids in establishing if the rock units in question are a cogenetic intrusive suite, and if so, how they differentiated. Whole-rock analysis of samples yields the concentrations of major and trace elements present in a sample. Major elements are presented as weight percentages in their oxide forms. Trace elements are presented in ppm in their elemental form. Because of their high concentrations, major element compositions are responsible for the physical properties of melts and the minerals that precipitate from them. Along with field observations, differentiation of cogenetic igneous rocks is best characterized by looking for trends in various plots that compare different combinations of major elemental oxides. Trace elements, on the other hand, give insight into the origin of a melt due to their relatively consistent proportions in a magmatic body throughout the entirety of its evolution. Trace elements are generally less strongly affected by the crystallization of individual phases, and often only occur as impurities in other minerals.

Whole-Rock Geochemistry Sample Preparation and Analysis

Samples analyzed for whole-rock geochemistry were run either at Cal Poly Pomona rock preparation and mineral separation laboratory using X-ray Fluorescence (XRF), or at the Washington State University Peter Hooper GeoAnalytical Lab using both XRF and inductively-coupled-plasma mass spectrometry (ICP-MS). All trace-element analyses were conducted using the XRF and ICP-MS at Washington State University's Peter Hooper GeoAnalytical Lab. The XRF at Cal Poly Pomona runs

samples in powdered form, while the XRF and ICP-MS at the Peter Hooper GeoAnalytical Lab runs samples in the form of glass beads, and therefore preparation of samples is different for each machine.

Powdered samples at Cal Poly Pomona are prepared by first crushing chips of the sample in a ball mill to reduce the sample to powder. Six grams of powdered sample are mixed with 1.2 grams of cellulose powder to help fuse the powder together. The material is then flattened into a disk using a hydraulic press that is cranked to 15 tons of force. Two disks for each sample are made and analyzed using the XRF. All glass-bead samples were prepared and analyzed at the Washington State University Peter Hooper GeoAnalytical Lab.

X-Ray Fluorescence (XRF) spectroscopy is the process by which x-rays bombard a sample with enough energy to excite electrons from inner electron shells to outer electron shells. Excited electrons that return to the ground state will emit secondary x-rays known as fluorescent x-rays. Certain wavelengths of secondary x-rays are characteristic of certain elements. The fluorescent x-rays that are emitted from the sample then travel to a curved crystal that maximizes reflection of the radiation to an exit slit. Only certain angles will reach the exit slit rather than hitting the wall on either side. The XRF rotates the curved crystal by an angle θ while rotating the slit and detector by 2θ , so that the angles are always correct for reflection, even as the angle changes. Each angle corresponds to a specific wavelength (energy) via Bragg's Law, and each wavelength corresponds to a certain element. The XRF detects the amount of kilocounts per second of reflected radiation at these specific angles that correspond to specific elements. The more kilocounts per seconds recorded for an angle of emitted and reflected

radiation, the more the corresponding element is present in the sample, as quantified based on calibration against 9 USGS standards with known elemental concentrations. BCR-2, BIR-1, W-2, AGV-2, GSP-2, and G-2 are used by both Cal Poly Pomona and WSU. QLO-1, BHVO-2, and RGM-1 are only used by Cal Poly, Pomona, and PCC-1, DNC-1, and STM-1 are only used by WSU.

Once XRF analysis is complete, raw data is then normalized to 100% based on the total yield of oxides for each sample. The CIPW norm is used to calculate an idealized mineralogy for igneous rocks based on their elemental compositions (Cross et al., 1902) (Fig. 30). CIPW norm calculations follow a set of rules designed to allocate the oxides to a set of end-member minerals (Cross et al., 1902). Because the CIPW norm uses a limited set of minerals that reflects compositional variables instead of mineralogical variables, accurate comparisons and identifications of samples can be made (Fig. 30). The CIPW norm assumes only anhydrous mafic minerals are present, and therefore does not correspond exactly with the actual mineralogy of biotite and hornblende bearing rocks, but can be used as a good proxy for quartz and feldspars (Fig. 30). Modal mineralogy was not point counted in thin section partially due to complications related to COVID-19 restrictions. All XRF geochemical data is renormalized based on the total yield of oxides for each sample, since it is usually under 100%. Data from samples that have been measured twice is then averaged.

Whole-rock data is interpreted by using a variety of variation diagrams (Fig. 24, 27-35). Variation diagrams compare two or more chemical constituents of various samples. Any constituents can be compared to another, but some have proven to provide more useful information than others. Three popular plots are the modified alkali-lime

index ($\text{NaO}_2 + \text{K}_2\text{O} + \text{CaO}$ vs. Wt% SiO_2) (Fig. 27), the ASI index vs AI-index ($\text{Al}/(\text{Na} + \text{K})$ vs. $\text{Al}/(\text{Ca} + \text{Na} + \text{K})$) (Fig. 28), and the Fe-index ($\text{FeO}/(\text{FeO} + \text{MgO})$ vs Wt% SiO_2) (Fig. 29). Trends in these plots can help with interpretations of differentiation processes, which may give insight into the tectonic processes responsible for the creation of the intrusive suite under question. For variation diagrams to have significance, it must be reasonable to assume that the rocks being examined are related and make up a petrogenetic province, and they should only be used to assess the validity of a specific hypothesis.

RESULTS

Field Map Description

Mapping of the Bristol Mountains field site was conducted at a 1:24000 scale, and the area contains several rock units of varying ages and compositions (Fig. 7). The focus of this study centers around the Late Cretaceous intrusions found in this area, but the relationship between these intrusions and the other features of the area is also important to understand. Most of the field mapping area is taken up by five light-colored rock units, that strike in generally the same direction (Fig. 7, 9-13). These units predominantly strike in a NE-SW direction, but some units can better be described as having a NNE-SSW strike direction (Fig. 7). The felsic units have dips varying from about 30° to 60° in most areas, although some outcrops on the southern edge of the site appear to have greater dip angles of around 80° or more (Fig. 7, 8). The five felsic units covered in this study vary in grain size, composition, mineralogy, age, and sometimes outcropping texture (Fig. 9-13). The field and hand-sample descriptions of these units are as follows.

Budweiser Granodiorite

The Budweiser Granodiorite (Kbw) can be defined as equigranular hornblende biotite granodiorite with columnar biotite and sphene (named for its proximity to the Budweiser wash) (Fig. 9). This unit is located on the southeastern boundary of the field site and is one of the least exposed of the five units in terms of volume but is the one of the most easily accessible due to its proximity to the dirt road a couple miles south of the site (Fig. 7). This unit has a medium-grained equigranular texture, with a groundmass of quartz and feldspar minerals ranging in sizes of about 1 to 3 mm in diameter (Fig. 9). Compared to the other felsic, light-colored units, the average crystal size of the

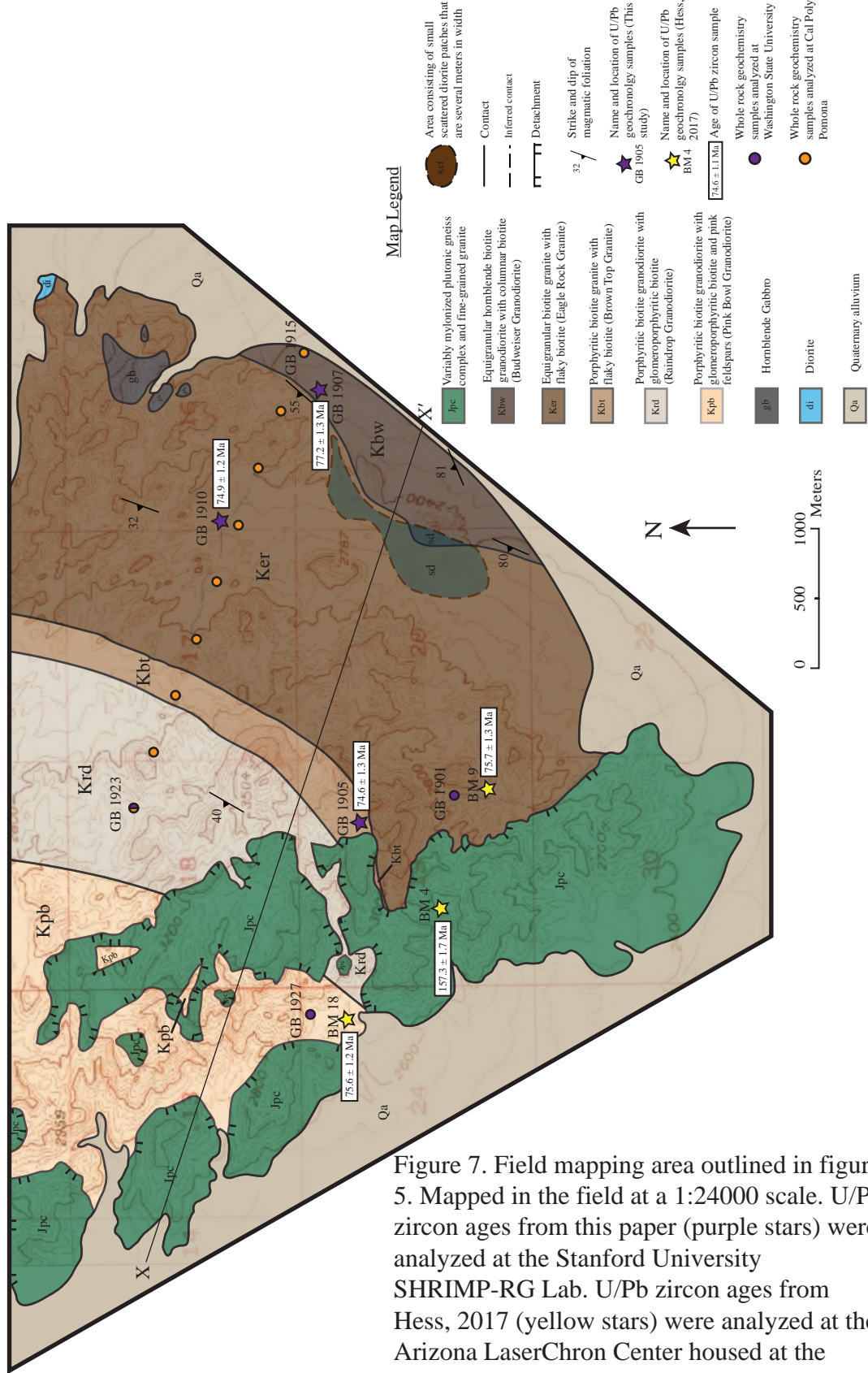


Figure 7. Field mapping area outlined in figure 5. Mapped in the field at a 1:24000 scale. U/Pb zircon ages from this paper (purple stars) were analyzed at the Stanford University SHRIMP-RG Lab. U/Pb zircon ages from Hess, 2017 (yellow stars) were analyzed at the Arizona LaserChron Center housed at the University of Arizona using a SC-ICP-MS.

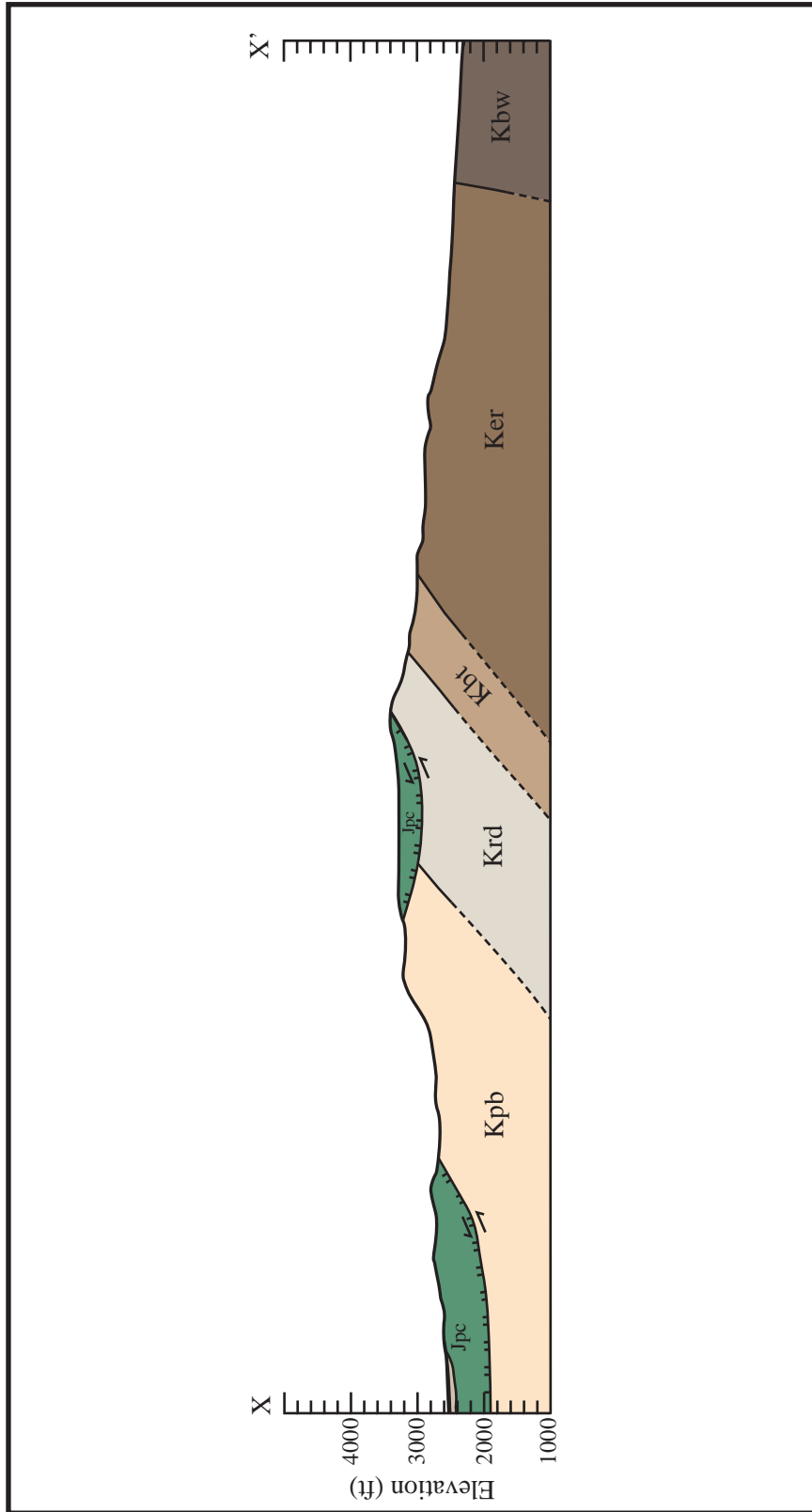


Figure 8. Cross section of the Bristol Mountains across the transect X-X', shown in the Bristol Mountains geologic map (Fig. 7).

groundmass in Kbw is noticeably the smallest (Fig. 9). Compositionally, hand samples are about 20% quartz and 25% mafic minerals, and the feldspar is 70% plagioclase and 30% K-feldspar (Fig. 9). The quartz and feldspar minerals are mostly subhedral, and the shape of many of the biotite crystals in Kbw is columnar (Fig. 9, 14). The Budweiser Granodiorite is the only unit that contains this biotite form, making it easily distinguishable from the other units. The shape of columnar biotite is similar to that of a tall aluminum can (Fig. 14). These relatively cylindrical shaped biotite crystals can often be 3-4 millimeters tall and around 1-2 mm in diameter and can vary from distinctly hexagonal to more circular (Fig. 14). Not all biotite crystals in this unit are distinctly columnar in shape, but most do extend significantly along the c axis. This unit is also the only one that consistently contains both hornblende and sphene (Fig. 9). The hornblende crystals are not as prevalent or as large as the biotite crystals. Small sphene crystals are the least prevalent, yet still easily identifiable, mineral in the samples. The Budweiser Granodiorite does appear to have a generally darker weathering pattern than the other units, which is due to its relatively mafic composition (Fig. 9). Kbw is also the most fragile and crumbly of the units, easily shattering into small pieces upon being struck with a 5-pound sledgehammer. Once collected, samples from this unit seem to crumble simply by transporting them in backpack or storing them in a confining space.

Eagle Rock Granite

The Eagle Rock Granite (Ker) is defined as equigranular biotite granite with flaky biotite (named for a distinctly shaped and protruding outcrop within) (Fig. 10, 15). This unit encompasses the largest area out of the five units mapped and is also the most easily accessible as it is the most southern unit, and the closest to the dirt road located to the



Figure 9. Field photo of the Budweiser Granodiorite (Kbw). This unit is equigranular hornblende biotite granodiorite with columnar biotite and sphene. This is the oldest and most mafic of the five felsic units mapped.



Figure 10. Field photos of the Eagle Rock Granite (Ker). This unit is equigranular biotite granite with flaky biotite.

south of the site (Fig. 7). This unit has a medium- to coarse-grained equigranular texture, with a groundmass of quartz and feldspar minerals that have an average size ranging from about 3 to 7 mm in diameter (Fig. 10). Although also equigranular in texture, Ker has a visibly larger average groundmass crystal size than that of Kbw (Fig. 10).

Compositionally, hand samples are about 35% quartz and 10% biotite, and the feldspar is 60% plagioclase and 40% K-feldspar (Fig. 10). The quartz and feldspar minerals are primarily anhedral, and the shape of many of the biotite crystals in the Eagle Rock Granite can be described as flaky (Fig. 10, 14). Both Ker and Kbt predominantly contain the flaky biotite form (Fig. 14). Flaky biotite contains clumps or groupings of small sheets of biotite, but unlike columnar biotite, do not form in thick stacks or organize in such a way to make a definable shape (Fig. 14). While the columnar biotite is made up of larger biotite crystals, flaky biotite is generally a more loose and disorganized grouping of smaller, thinner biotite crystals (Fig. 14). Therefore, only the width of flaky biotite clusters can be easily measured in most circumstances (Fig. 14). Flaky biotite crystals are often around 2-4 mm in diameter and can vary in shape from distinctly hexagonal, to circular, to undistinguishable (Fig. 14). The Eagle Rock Granite is one of the lightest colored units, especially in canyons and other areas where weathering may have a relatively low impact on the rock outcrop surfaces (Fig. 10, 15).

Brown Top Granite

The Brown Top Granite (Kbt) is defined as porphyritic biotite granite with flaky biotite (named for the distinct color of the mylonites that are present at the highest point of the field site and within this unit) (Fig. 11). This unit encompasses the smallest area out of the five units mapped and is only about 300 meters in width (Fig. 7). This unit has

a coarse-grained porphyritic texture, with a groundmass of quartz and feldspar minerals that have an average size ranging from about 4 to 7 mm in diameter (Fig. 11). Potassium feldspar phenocrysts encompass about 5% of the surface area of outcrops and samples and have an average size of about 1.5 to 2 centimeters (Fig. 11). Compositionally, hand samples are about 30% quartz and 15% biotite, and the feldspar is 60% plagioclase and 40% K-feldspar (Fig. 11). The quartz and feldspar minerals are primarily anhedral, phenocrysts are subhedral, and the shape of many of the biotite crystals can also be described as flaky (Fig. 11, 14). Although both units contain flaky biotite, Kbt has larger biotite crystals than Ker (Fig. 11).

Raindrop Granodiorite

The Raindrop Granodiorite (Krd) is defined as porphyritic biotite granodiorite with glomeroporphyritic biotite (Fig. 12, 15) (named after a sudden change in weather that occurred while sampling this unit). This unit encompasses a significant portion of the mapping area, and but less so than Ker (Fig. 7). This unit has a coarse-grained porphyritic texture, with a groundmass of quartz and feldspar minerals that have an average size ranging from about 3 to 6 mm in diameter (Fig. 12). K-feldspar phenocrysts encompass about 5% of the surface area of outcrops and samples and have an average size of about 1 to 1.5 centimeters (Fig. 12). Compositionally, hand samples are about 30% quartz and 15% biotite, and the feldspar is 65% plagioclase and 35% K-feldspar (Fig. 12). The quartz and feldspar minerals are primarily anhedral, phenocrysts are subhedral to anhedral, and small biotite crystals are frequently grouped together in clusters (glomeroporphyritic texture) (Fig. 14). Glomeroporphyritic biotite has very little shine and can be described as looking dull or dirty even (Fig. 14).

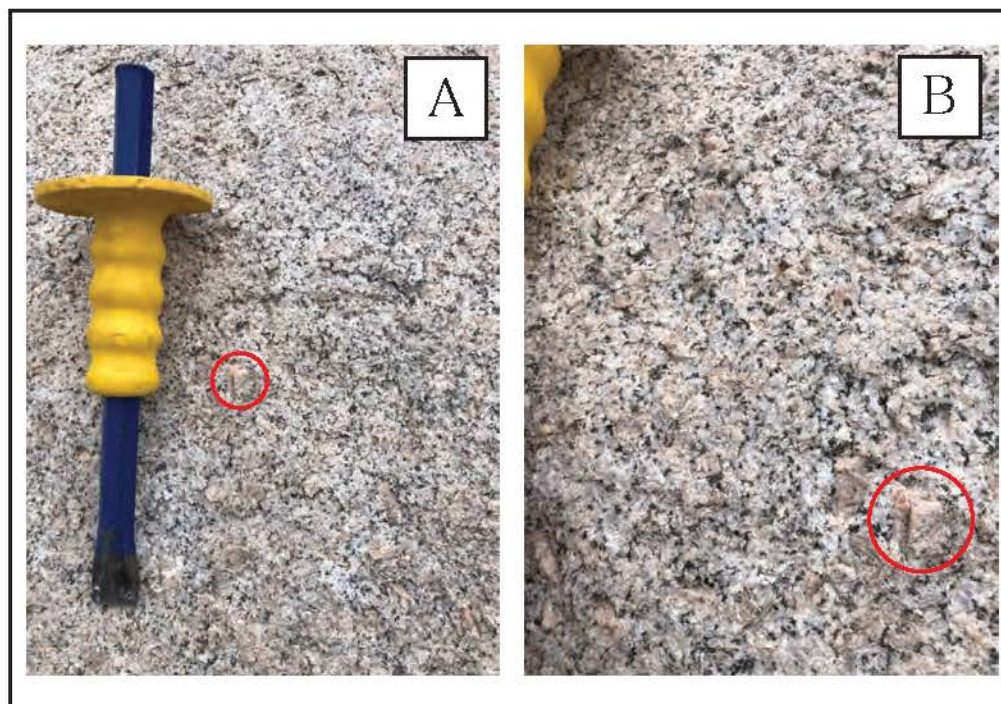


Figure 11. Field photos of the Brown Top Granite (Kbt). This unit is porphyritic biotite granite with flaky biotite. Red circles outline the same example of a distinctly larger phenocryst. The chisel is 30 cm long.



Figure 12. Field photos of the Raindrop Granodiorite (Krd). This unit is porphyritic biotite granodiorite with glomeroporphyritic biotite. The hammer is 27 cm long.

Pink Bowl Granodiorite

Encompassing the most northwestern part of the mapping area, the Pink Bowl Granodiorite (Kpb) is defined as porphyritic biotite granodiorite with glomeroporphyritic biotite and large pink K-feldspar phenocrysts (named after a bowl-shaped valley and the distinct pink phenocrysts within this unit) (Fig. 7, 13). This unit has a coarse-grained porphyritic texture, with a groundmass of quartz and feldspar minerals that have an average size ranging from about 3 to 6 mm in diameter (Fig. 13). Pink potassium feldspar phenocrysts encompass about 15% of the surface area of outcrops and samples and have an average size of about 1.5 to 2 centimeters (Fig. 13). Compositionally, hand samples are about 30% quartz and 20% biotite, and the feldspar is 70% plagioclase and 30% K-feldspar (Fig. 13). The quartz and feldspar minerals are subhedral to anhedral, phenocrysts are euhedral to subhedral, and the shape of the biotite crystals is glomeroporphyritic (Fig. 13, 14).

Mafic Units

A prominent feature of this field site is the large outcroppings of gabbro on the eastern side (Fig. 16, 17). These gabbro outcrops are quite large, on the scale of 100+ meters in diameter, but comprise only a small portion of the total mapping area (Fig. 7, 16). Gabbros are located within the Eagle Rock Granite, and veins of leucogranite can often be seen cross cutting within them (Fig. 7, 16). In a few locations, thin bands of alternating light and dark material can be found at or near contacts between granodiorite and gabbro (Fig. 17). In areas where exact contacts between gabbro and more felsic material can be found, the grain size of the felsic material is often quite fine (Fig. 17). Even when compared to the finest grain felsic unit (Kbw), the average crystal sizes of

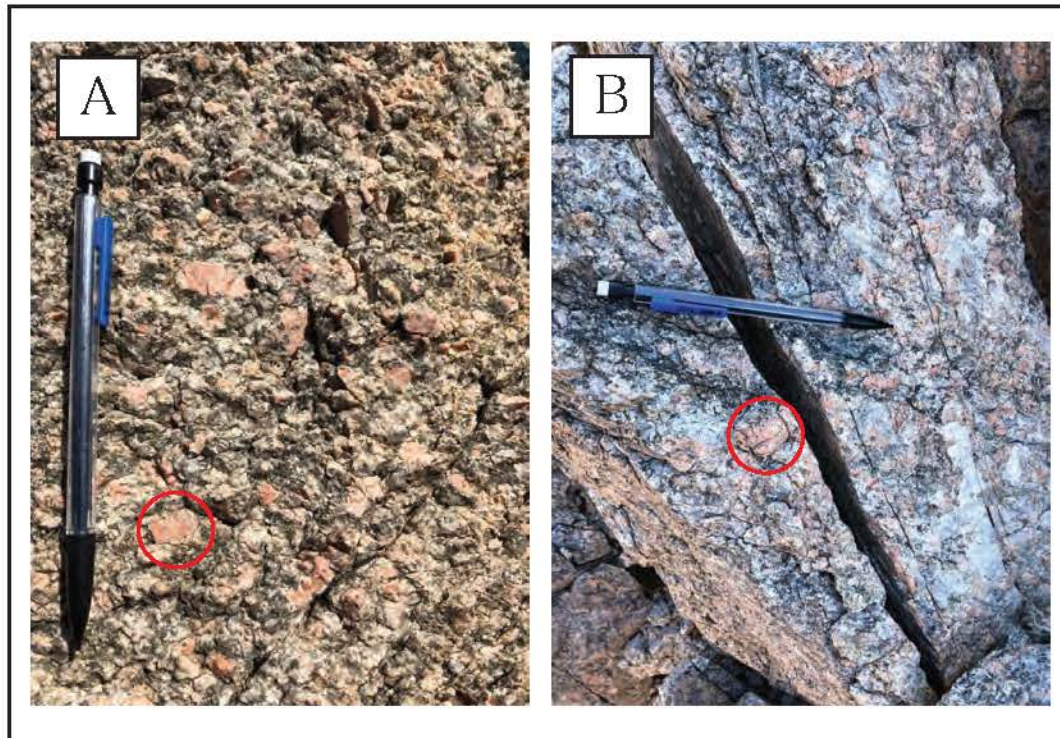


Figure 13. Field photos of the Pink Bowl Granodiorite (Kpb). This unit is porphyritic biotite granodiorite with glomeroporphyritic biotite and large pink phenocrysts. Red circles outline some examples of a distinctly larger phenocrysts.

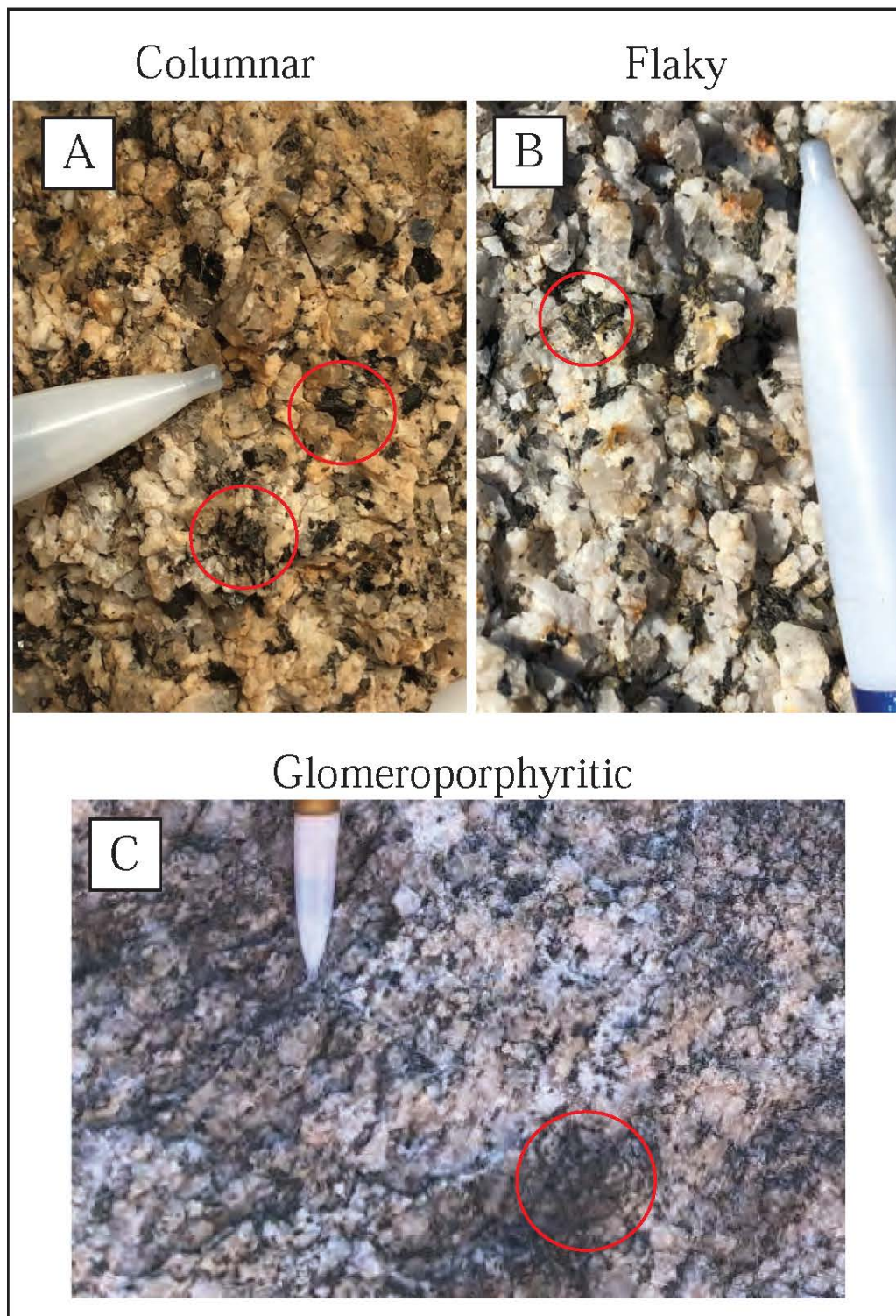


Figure 14. Examples of the three different shapes of biotite found in the five felsic units of the field mapping area. Columnar biotite is found in Kbw. Flaky biotite is found in Ker and Kbt. Glomeroporphyritic biotite is found in Krd and Kpb. Red circles outline distinct examples of each respective biotite shape.

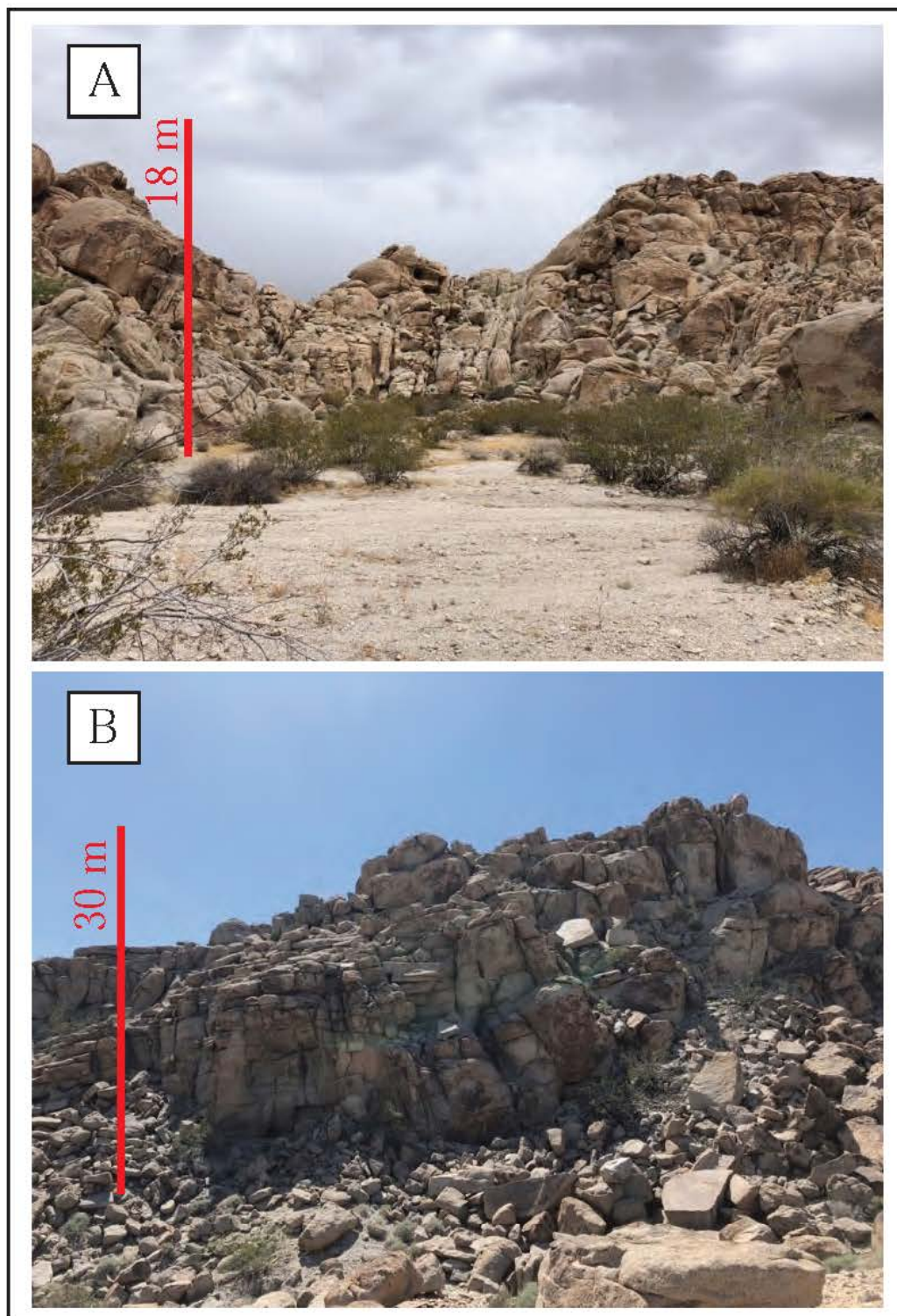


Figure 15. Field photos of outcrops taken in the middle of the field area encompassing Ker and Krd. (A) View looking to the east from near the location of sample GB 1910 (Ker). (B) View looking to the west from near the location of sample GB 1923 (Krd).

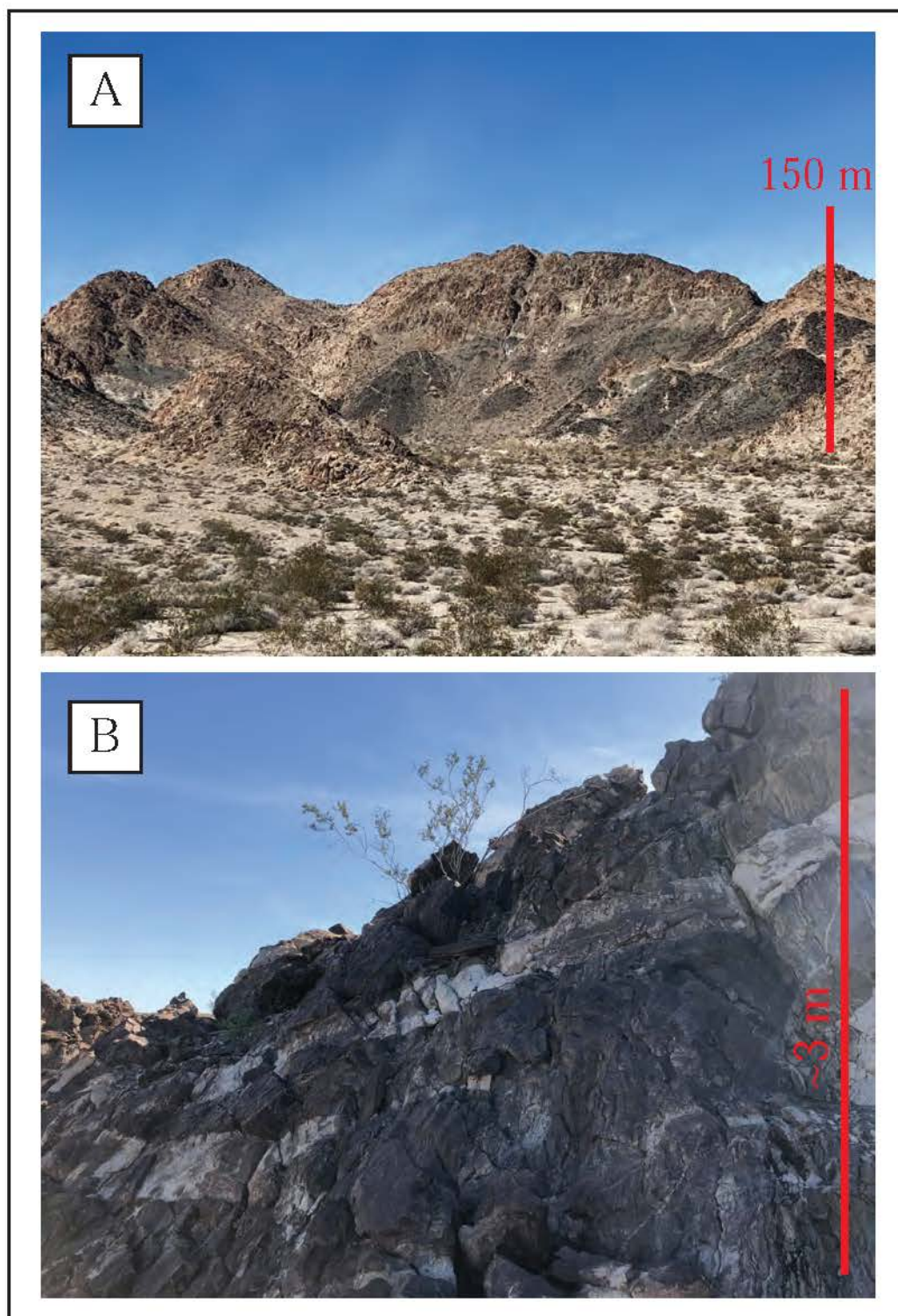


Figure 16. Outcrop scale images of the gabbro units located on the eastern side of the field mapping area. (A) Image looking to the northeast. The base to peak, the section of mountain in the middle of the photo is about 140 meters. (B) A more felsic band of material intertwined in a section of mafic material.

light-colored material at these contacts are noticeably smaller (Fig. 9, 17). Scattered patches of diorite can be found at the southeastern portion of the site, near the contact between Kbw and Ker (Fig. 18). These diorite patches are not prevalent, but they are notable (Fig. 18). Often, they are found in circular blotches ranging from about 3 to 6 m in diameter, but in some places are seen along the base of small valleys or dips in terrain (Fig. 18). Mafic enclaves can be found throughout the Budweiser Granodiorite (Kbw) (Fig. 19). These enclaves are 20-30 cm in length, of varying thicknesses, and have elongated axes that follow the strike of Kbw (Fig. 7, 19).

Description of Other Mapping Site Features

Outcrops of felsic units in the middle of the field site are predominantly rounded and tan to brown in color but can be more varied in other locations (Fig. 15). For example, rocks are very light colored with little desert varnish in canyons and the valley located at the northeastern section of the site (Fig. 15). Felsic units can also be very light colored in areas nearby the detachment on the western side of the site (Fig. 20). The western side of the mapping area includes a detachment fault that is part of a metamorphic core complex (Fig. 7, 20). The lighter Cretaceous granodiorite units are located within the footwall of the detachment fault, and darker Jurassic variably mylonized plutonic gneiss and fine-grained granite are located in the overlying hanging wall (Fig. 7, 20). Mylonite is also found at the detachment fault (Fig. 21), and felsic rocks contacting or nearby the detachment can appear to have been tectonically strained. The mylonized felsic rocks are much harder and lighter colored than the same type of felsic rocks located elsewhere in the mapping area. The tectonized are also more cohesive,

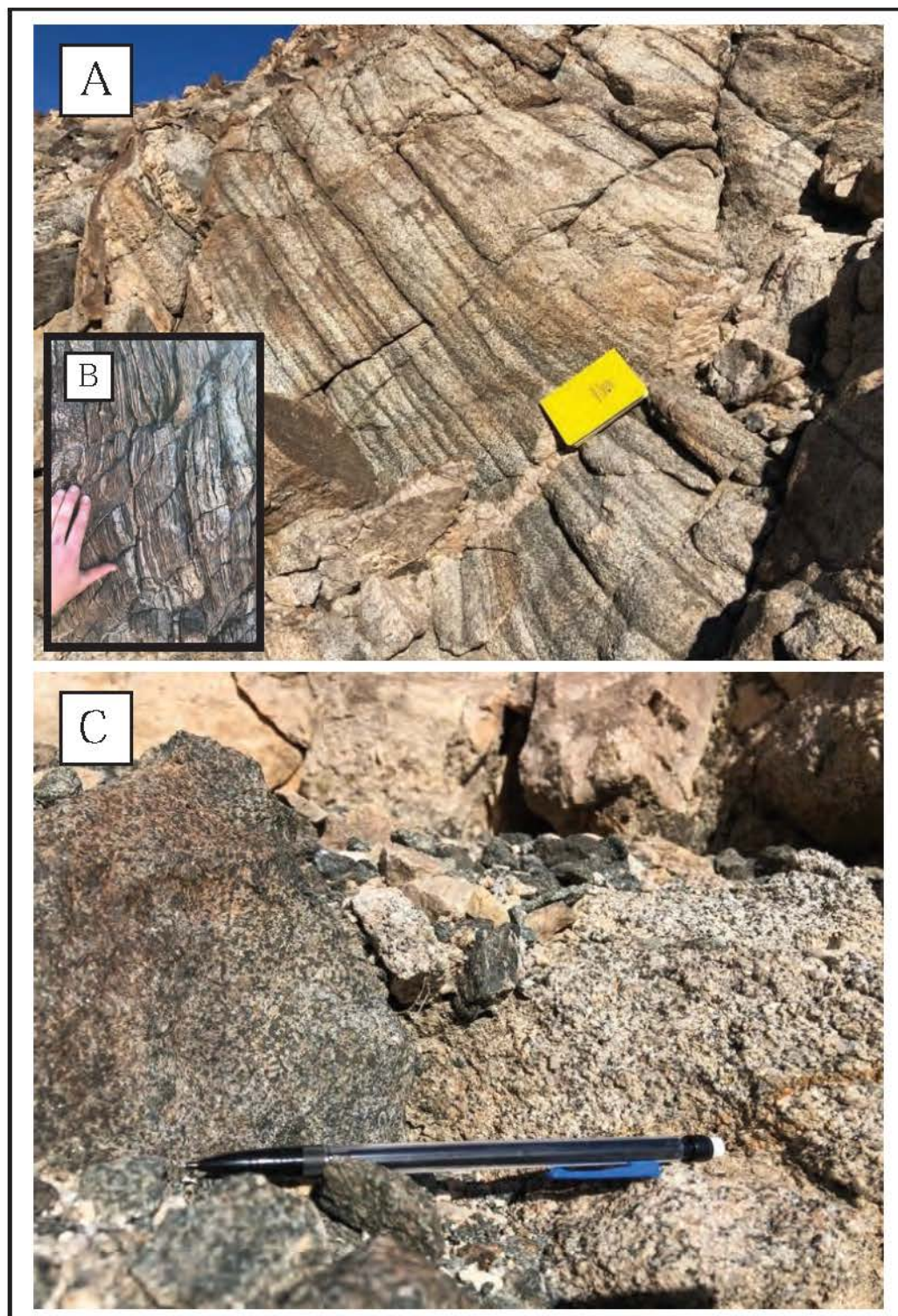


Figure 17. More images of or nearby the gabbro units located on the eastern side of the field mapping area. (A) and (B) both show a distinct banding pattern of alternating light and dark materials. Both images were taken nearby a contact between felsic and gabbro units. (C) Upclose image of a contact between a felsic and a gabbro unit.



Figure 18. Image of scattered patches of diorite located in southern most portion of the field site. The diorite in the red circle is about 5 meters in diameter.

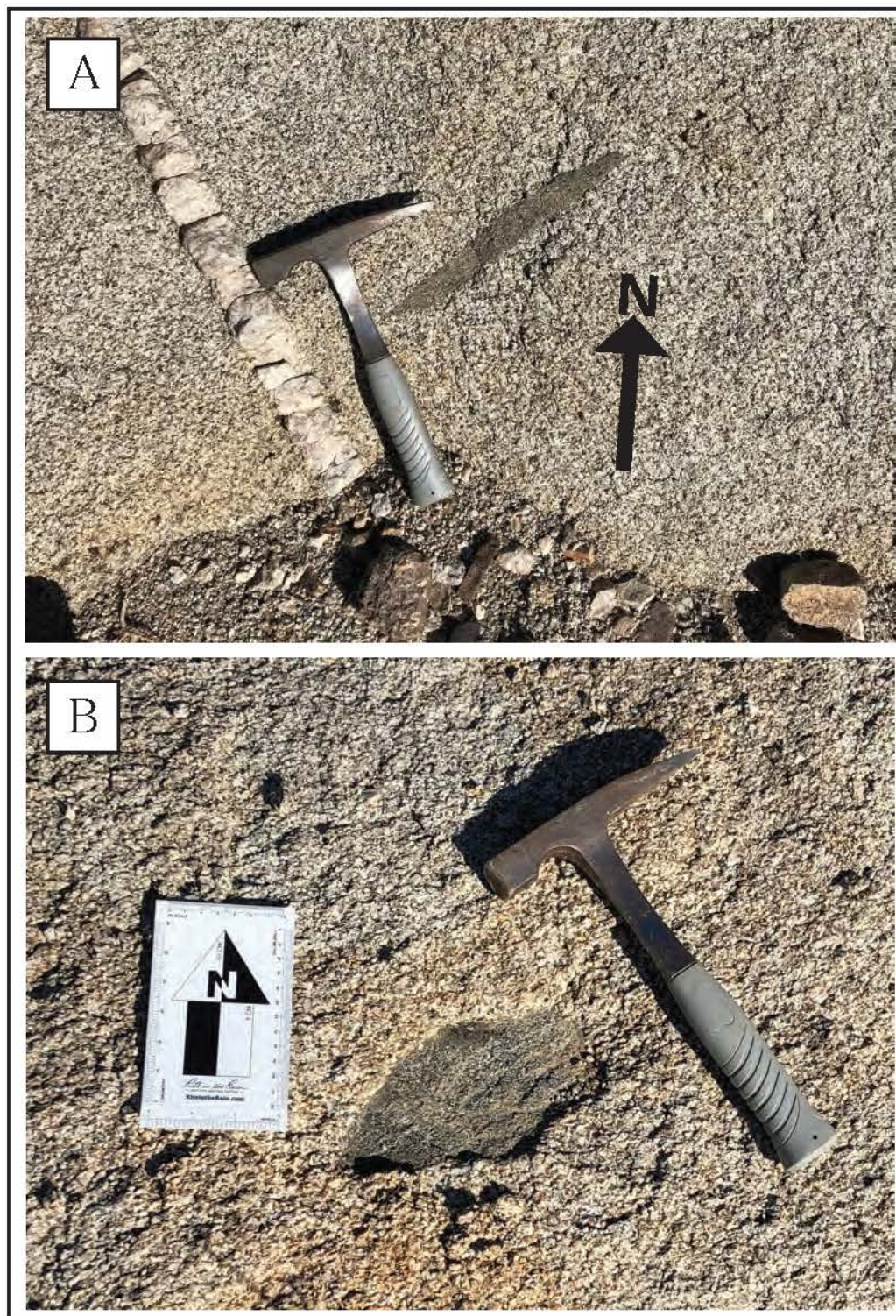


Figure 19. Images of mafic enclaves located in the southern and southeastern portion of the field site (within Kbw). The orientation of the elongate axis of the enclaves generally follows the orientation of the nearby contact between granodiorite/granite units.

giving samples a smooth look and feel, rather than the crumbly texture that most of the felsic rocks exhibit.

Reconnaissance Samples

Reconnaissance samples were collected to determine whether plutonic rocks in the surrounding area may be related to the five felsic units of the Bristol Mountains field mapping area (Fig. 5). One sample was collected from the Cady Mountains to the west of the mapping site, one was collected from the Lava Bed Mountains to the south, and four were collected from the Rodman Mountains to the southwest (Fig. 5). Each sample collected shared some resemblance to at least one of the five felsic units of the Bristol Mountains site, but samples GB 2004 and GB 2010 located in the Rodman Mountains bore the closest resemblance (Fig. 5). These two samples were most like Kbt of the Bristol Mountains site, as they shared distinguishing features such as having flaky biotite crystals and large K-feldspar phenocrysts (Fig. 5, 11). Samples GB 2004 and GB 2010 also were representative of a large area of the Rodman Mountains, as the same rock units were continually seen throughout the surrounding area on drives and hikes (Fig. 5). Both GB 2004 and GB 2010 were collected from the same ridge miles from one another, and it seems likely that rocks similar to the Bristol Mountains site are found consistently between the two samples (Fig. 5). GB 2005 and GB 2007 were also collected in the Rodman Mountains, south of the ridge in which GB 2004 and GB 2010 were collected (Fig. 5). GB 2005 is very light-colored, has a fine grain equigranular texture, and is found right by a couple small patches of gabbro (Fig. 5). GB 2007 is equigranular and medium grained, like the Budweiser Granodiorite of the Bristol Mountains, but the percentage of mafic minerals is small (Fig. 5). GB 2009 was collected from the Cady

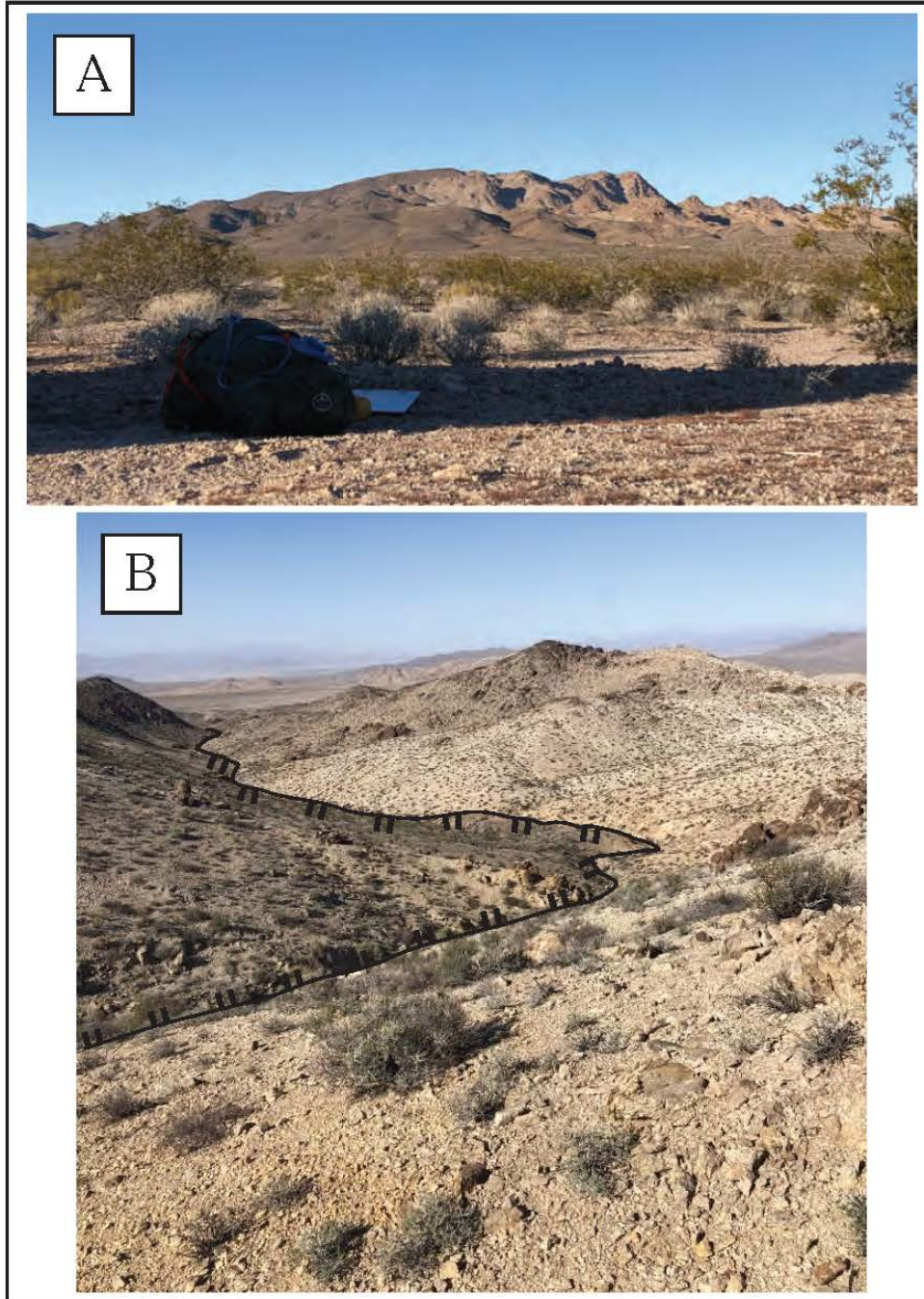


Figure 20. Images of the detachment fault located on the western portion of the field mapping site. The darker material is the Jurassic variably mylonized plutonic gneiss complex and the lighter material is the Cretaceous granodiorite. (A) View looking north of the entire field mapping site, taken from the dirt road about two miles away. From the road to the tallest peak in the image, the elevation change is about +1340 ft. Darker colored rock is seen on the left (west) side of the image while lighter colored rock is seen on the right (east) side of the image. (B) View looking north while standing on the detachment fault. The Jurassic unit (hanging wall) is to the left of the marked contact and Cretaceous units (footwall) are to the right.



Figure 21. Image of mylonite located near the detachment fault on the western portion of the field mapping area

Mountains (Fig. 5). It is the finest grained of the reconnaissance samples and has a low mafic percentage, but also has a similar composition to samples from the Bristol Mountains. NVB 2001 is an equigranular quartz monzonite from the Lava Bed Mountains with low mafic percentage (Fig. 5).

U/Pb Geochronology

Three samples from the Bristol Mountains site were collected for zircon U/Pb geochronology to constrain crystallization ages of the felsic units (Fig. 22). These samples were GB 1907 from Kbw, GB 1910 from Ker, and GB 1905 from Kbt (Fig. 7, 22). All three samples yielded Late Cretaceous ages, contained older inherited cores, and exhibited oscillatory zoning textures (Fig. 22, 23). Ten spot analyses of zircon crystal rims from sample GB 1907 (Kbw) yielded ages ranging from 75.8 to 78.6 Ma, and a weighted mean $^{206}\text{Pb}/^{238}\text{U}$ age of 77.2 ± 1.3 Ma with a 95% confidence and MSWD of 0.44 (Fig. 22). Two inherited cores from GB 1907 were also analyzed and yielded Late Jurassic ages of 152 ± 6 Ma, and 156 ± 10 Ma (Fig. 22, 23). Eleven spot analyses of zircon crystal rims from sample GB 1910 (Ker) yielded ages ranging from 72.0 to 76.0 Ma, and a weighted mean $^{206}\text{Pb}/^{238}\text{U}$ age of 74.9 ± 1.2 Ma with a 95% confidence and MSWD of 0.46 (Fig. 22). One inherited core from GB 1910 was analyzed and yielded a Middle Jurassic age of 171 ± 10 Ma (Fig. 22, 23). Eleven spot analyses of zircon crystal rims from sample GB 1905 (Kbt) yielded ages ranging from 69.3 to 77.3 Ma, and a weighted mean $^{206}\text{Pb}/^{238}\text{U}$ age of 74.6 ± 1.3 Ma with a 95% confidence and MSWD of 1.15 (Fig. 22). One inherited core from GB 1905 was analyzed and yielded a Middle Jurassic age of 166 ± 8 Ma (Fig. 22, 23).

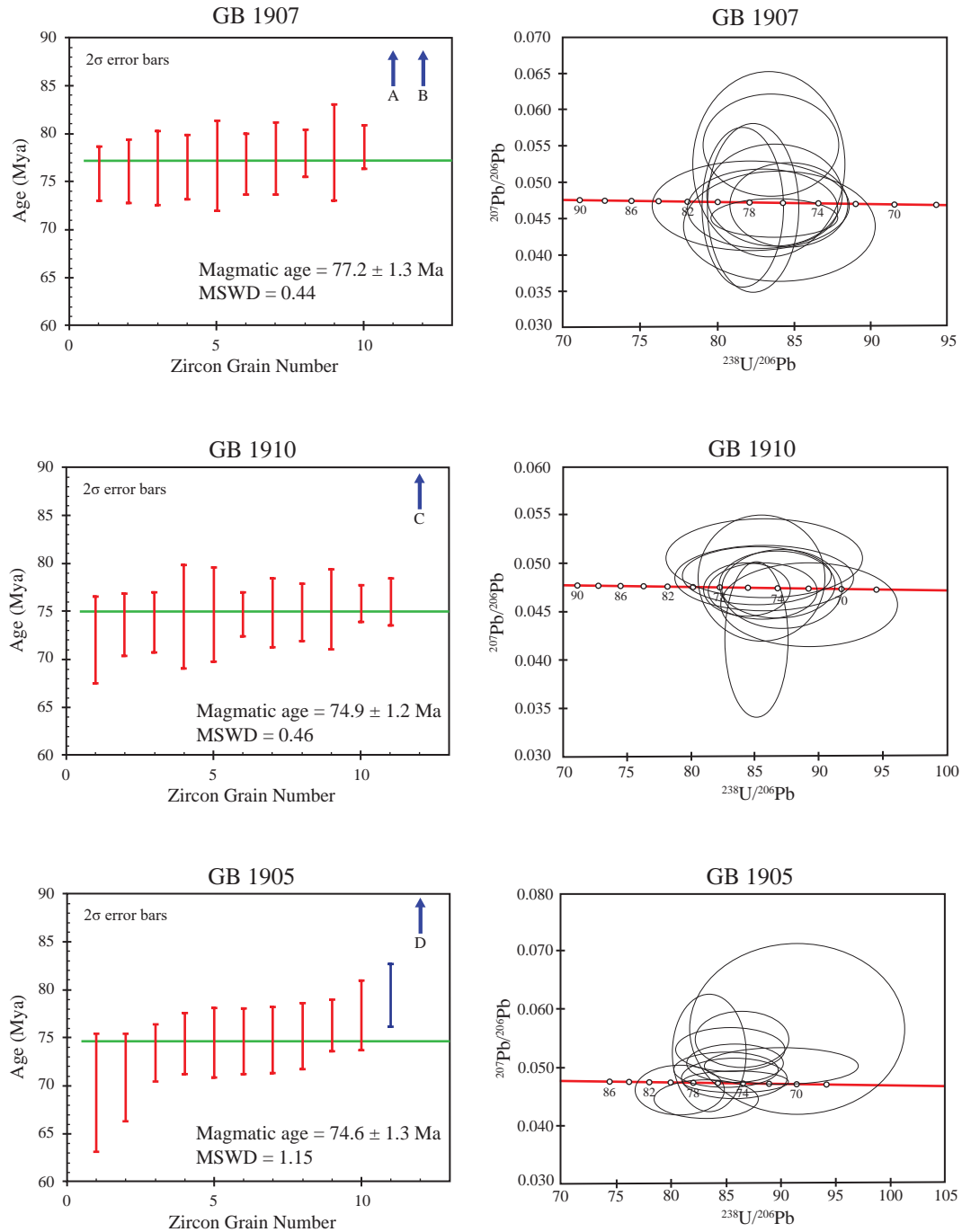


Figure 22. U/Pb zircon mean age plots and inverse concordia diagrams for samples GB 1907 (Kbw), GB 1910 (Ker), and GB 1905 (Kbt) located in the Bristol Mountains field mapping area (Fig. 7). These samples are represented by purple stars in figure 7. Arrows A, B, C, and D point to ages of inherited cores. Core A = 152 ± 6 Ma, core B = 156 ± 10 Ma, core C = 171 ± 10 Ma, and core D = 166 ± 8 Ma.

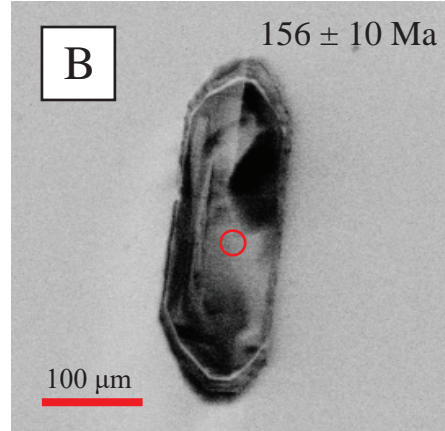
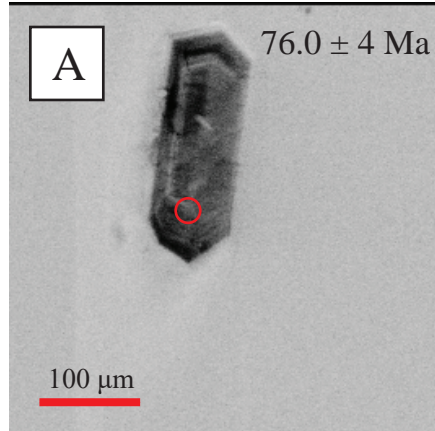
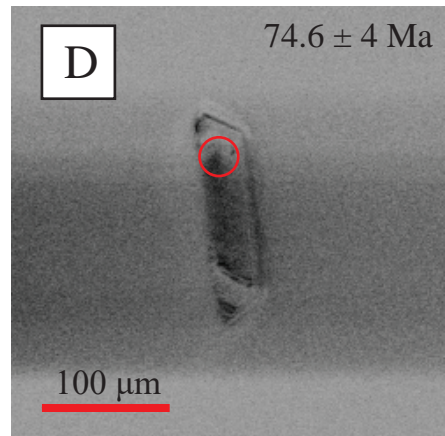
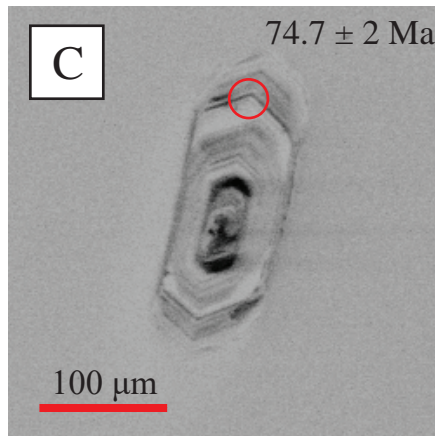
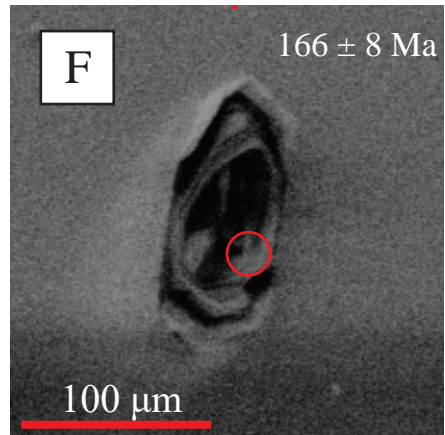
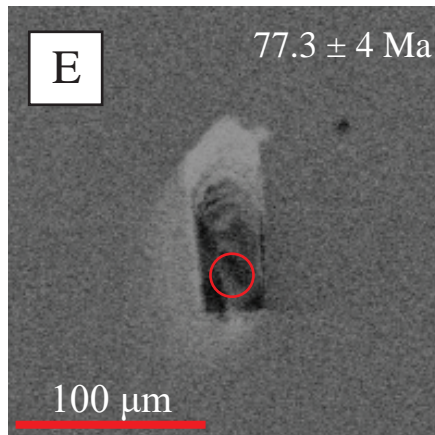
GB 1907GB 1910GB 1905

Figure 23. Cathodo-luminescence (CL) images of zircon grains taken at Cal Poly Pomona. The red circles are representative of the location of the spot created by the SHRIMP-RG's primary ion beam, which are approximately 30 microns wide. Images (B) and (F) are older inherited zircon cores found within samples GB 1907 and GB 1905 respectively.

Whole-Rock Major-Element Geochemistry

Fourteen samples collected from the Bristol Mountains mapping site (Fig. 7), and six samples from various locations in the Cady, Lava Bed, and Rodman Mountains (Fig. 5) were analyzed for whole-rock major-elemental composition. Nine samples were analyzed at the Cal Poly Pomona rock preparation and mineral separation laboratory using X-ray Fluorescence (XRF), and twelve samples were analyzed by XRF at the Washington State University Peter Hooper GeoAnalytical Lab (Fig. 5, 7, 24-35). Sample GB 1923 was analyzed by XRF at both the Cal Poly Pomona, and Washington State University laboratories. Unnormalized oxide data are shown in Table 1, but normalized data is used in the diagrams that follow. The diagrams used to evaluate geochemical trends and variation are as follows: (1) Harker plots of oxides vs. silica (Fig. 24), (2) major-element oxides vs. distance across the five units at the Bristol Mountains mapping site (Fig. 25, 26), (3) modified alkali-lime index diagram (Fig. 27), (4) aluminum saturation index vs. alkalinity index diagram (Fig. 28), (5) iron index diagram (Fig. 29), and (6) quartz-plagioclase-alkali feldspar ternary diagram (Fig. 30). Some discrepancies between the Cal Poly Pomona and the Washington State University data do exist, possibly due to the differing method of analysis (powder vs. glass bead) or different USGS standards used by the XRF machines (Fig. 25). Powder XRF analysis may be biased due to incomplete homogenization between the sample and the binder. There may also be different matrix effects related to X-ray absorption by cellulose (in CPP powder samples) vs. lithium tetraborate (in WSU glass bead samples). Overall, samples are either calc-alkali or calcic (Fig. 27), peraluminous (Fig. 28), and magnesian (Fig. 29).

Table 1. Unnormalized major-elemental oxide concentrations of samples in weight percentage (wt%). Orange samples are Bristol Mountains field site samples that were analyzed at Cal Poly Pomona (Fig. 7). Purple samples are Bristol Mountains field site samples that were analyzed at Washington State University (Fig. 7). Green samples are reconnaissance samples that were analyzed at Washington State University (Fig. 5).

Sample Number	SiO ₂ (wt%) unnorm.	MgO (wt%) unnorm.	Al ₂ O ₃ (wt%) unnorm.	Na ₂ O (wt%) unnorm.	P ₂ O ₅ (wt%) unnorm.	K ₂ O (wt%) unnorm.	CaO (wt%) unnorm.	TiO ₂ (wt%) unnorm.	MnO (wt%) unnorm.	FeO (wt%) unnorm.	Total (wt%) unnorm.
GB 1915	65.23	2.05	15.56	3.75	0.19	3.29	3.71	0.41	0.06	2.97	97.52
GB 1916	67.13	1.14	14.75	3.74	0.15	3.68	2.51	0.40	0.04	2.21	96.00
GB 1917	72.32	0.47	12.21	3.09	0.07	4.31	1.25	0.18	0.03	1.06	95.18
GB 1918	71.42	0.45	12.59	3.29	0.08	3.79	1.78	0.21	0.03	1.14	94.98
GB 1919	68.97	0.50	14.12	3.64	0.07	4.36	1.94	0.19	0.04	1.10	95.16
GB 1920	70.25	0.42	13.77	3.89	0.06	3.25	2.00	0.16	0.03	0.89	94.88
GB 1921	70.48	0.46	13.75	4.03	0.06	3.09	2.24	0.18	0.03	0.98	95.45
GB 1922	69.90	0.43	14.10	3.92	0.05	3.45	2.28	0.14	0.02	0.80	95.27
GB 1923	70.39	0.44	13.51	4.01	0.06	3.03	2.26	0.17	0.03	0.97	95.00
GB 1901	74.37	0.24	13.80	3.26	0.03	4.72	1.50	0.15	0.02	0.90	98.98
GB 1905	74.32	0.29	13.76	3.62	0.04	4.42	1.21	0.17	0.03	1.07	98.93
GB 1907	67.31	1.46	15.50	3.84	0.17	3.53	3.22	0.53	0.06	3.20	98.81
GB 1910	75.05	0.33	12.84	3.22	0.06	4.36	1.38	0.20	0.03	1.22	98.68
GB 1923	72.81	0.27	14.68	4.00	0.05	3.87	1.91	0.16	0.03	1.00	98.77
GB 1927	73.56	0.34	14.14	4.06	0.05	3.42	1.59	0.17	0.03	1.04	98.41
GB 2004	71.47	0.41	15.18	3.89	0.10	4.29	1.82	0.25	0.03	1.47	98.92
GB 2005	68.60	0.63	15.64	2.98	0.14	6.13	2.63	0.28	0.03	1.27	98.33
GB 2007	62.52	2.75	17.01	6.43	0.37	1.22	5.29	1.02	0.06	1.86	98.53
GB 2009	70.94	0.68	14.31	3.10	0.12	4.91	1.95	0.33	0.05	2.32	98.69
GB 2010	70.43	0.55	15.20	3.86	0.13	4.21	2.14	0.31	0.03	1.71	98.58
NVB 2001	65.13	1.47	15.39	2.89	0.17	6.59	3.85	0.56	0.06	2.31	98.43

Additionally, samples are predominantly granite or granodiorite, although a few reconnaissance samples plot as quartz monzonite or quartz diorite (Fig. 30)

Four Harker plots were used to evaluate how different oxide concentrations relate to silica content in both Bristol Mountains and reconnaissance samples (Fig. 24). On the Al_2O_3 vs. SiO_2 Harker plot, aluminum content of the Bristol Mountain samples ranges from 12.2% in Ker to 15.6% in Kbw, and from 14.3% to 17.0% in reconnaissance samples (Fig. 24). The plot has a very linear array that slightly curves downward to lower Al_2O_3 at higher silica content, and all recon samples generally fall along the linear trend created by the Bristol Mountain samples, but do not tightly align along the trend (Fig. 24). On the CaO vs. SiO_2 Harker plot, calcium content of the Bristol Mountain samples ranges from 1.2% in Kbt, to 3.7% in Kbw, and from 1.8% to 5.3% in reconnaissance samples (Fig. 24). The four samples with the lowest silica content from the Bristol Mountains plot along a very linear downward-trending line (Fig. 24). As the silica content of the Bristol Mountains samples reach >73%, there is a loose grouping of most of the Bristol Mountains samples that trend downward (Fig. 24). Reconnaissance samples, along with the lowest silica content Bristol Mountains samples, make a very tight, linear, and decreasing CaO trend (Fig. 24). On the MgO vs. SiO_2 Harker plot, magnesium content of the Bristol Mountain samples ranges from 0.2% in Ker to 2.0% in Kbw, and from 0.4% to 2.8% in reconnaissance samples (Fig. 24). Bristol Mountains samples show a large linear decrease in MgO for the four lowest SiO_2 samples, then a flat-trending linear grouping of the other samples (Fig. 24). Reconnaissance samples loosely follow the initial downward linear trend at lower silica contents, and level out and group with most Bristol Mountains samples at about 72% SiO_2 (Fig. 24). On the K_2O vs.

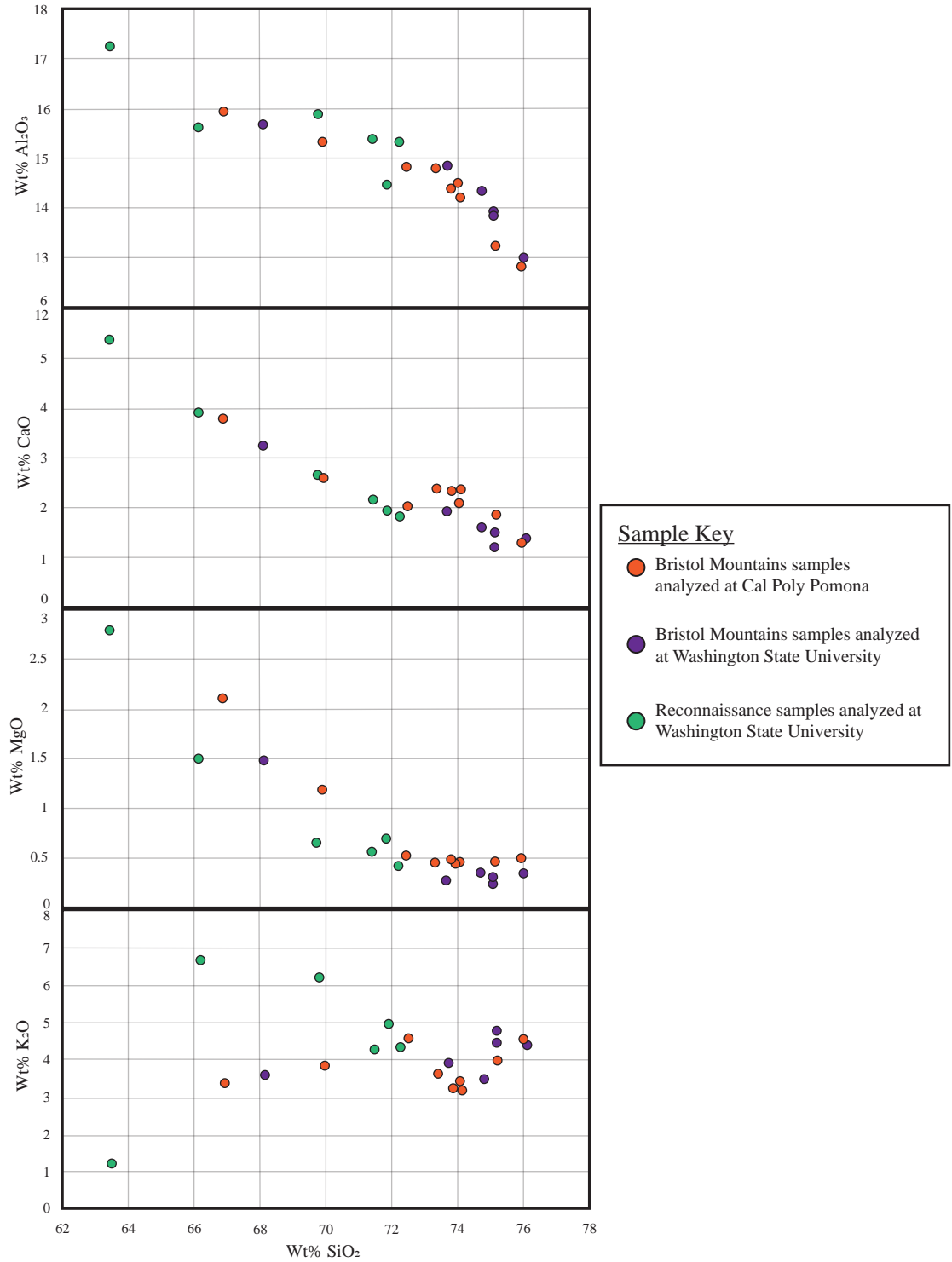


Figure 24. Harker plots of oxides vs. silica. Orange samples are Bristol Mountains field site samples that were analyzed at Cal Poly Pomona (Fig. 7). Purple samples are Bristol Mountains field site samples that were analyzed at Washington State University (Fig. 7). Green samples are reconnaissance samples that were analyzed at Washington State University (Fig. 5).

SiO₂ Harker plot, potassium content of the Bristol Mountain samples ranges from 3.0% in Krd to 4.7% in Ker, and from 1.2% to 6.6% in reconnaissance samples (Fig. 24). This is the least linear of the four Harker plots. The diagram shows a slight increase in K₂O for the lowest four SiO₂ Bristol Mountains samples, a drastic dip in K₂O from SiO₂ 72% to ~74%, and then a steep increase in K₂O for samples with SiO₂ about 75% and above (Fig. 24). Three reconnaissance samples follow the initial linear increase in K₂O at lower SiO₂ created by Bristol Mountains samples (GB 2007, GB 2004, GB 2010) (Fig. 24). One sample plots close to a grouping of other samples at ~72%, but doesn't tightly fit the linear trend (GB 2009), and two samples do not plot close to any other samples (NVB 2001, and GB 2005) (Fig. 24).

Four plots of oxides vs. distance were used to interpret how major oxide concentrations shift between the five units at the Bristol Mountains site (Fig. 25, 26). The x axis represents distance NW along an azimuth of 270° from the most southeast bedrock exposure, such that the left side of these diagrams represents the most southeast unit (Kbw) while the right side represents the most northwest unit (Kpb) (Fig. 7, 25, 26). On the SiO₂ vs. distance plot, there is a large increase in silica content when transitioning from Kbw into Ker, then a slight dip in silica content from Ker to Krd, and a slight increase in silica from Krd to Kpb (Fig. 25). On the K₂O vs. distance plot, potassium content generally increases from Kbw to about the center of Ker (or closer to Kbw), then decreases consistently from Ker to Kpb (Fig. 25). It should be noted that this graph has the highest discrepancy in the values for samples analyzed at Cal Poly Pomona versus Washington State University, and that the WSU data was used predominantly in the interpretation of this graph (Fig. 25). On the Al₂O₃ vs. distance plot, aluminum content is

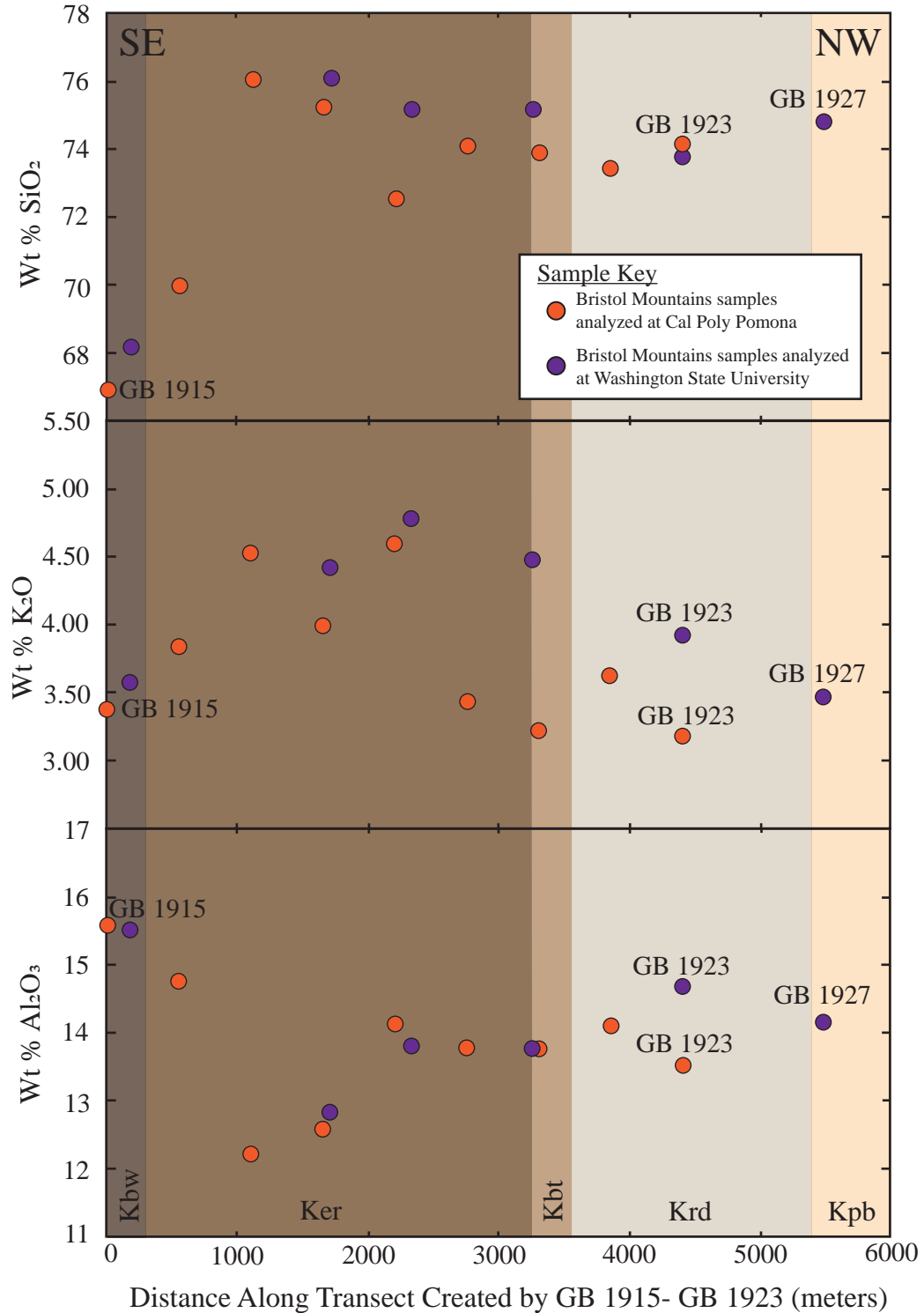


Figure 25. Plot showing how major-element oxide concentrations change throughout the Bristol Mountains field site from the southeast to the northwest (from Kbw to Kpb). Orange samples were analyzed at Cal Poly Pomona (Fig. 7). Purple samples were analyzed at Washington State University (Fig. 7). Colors of each unit match those in figure 7.

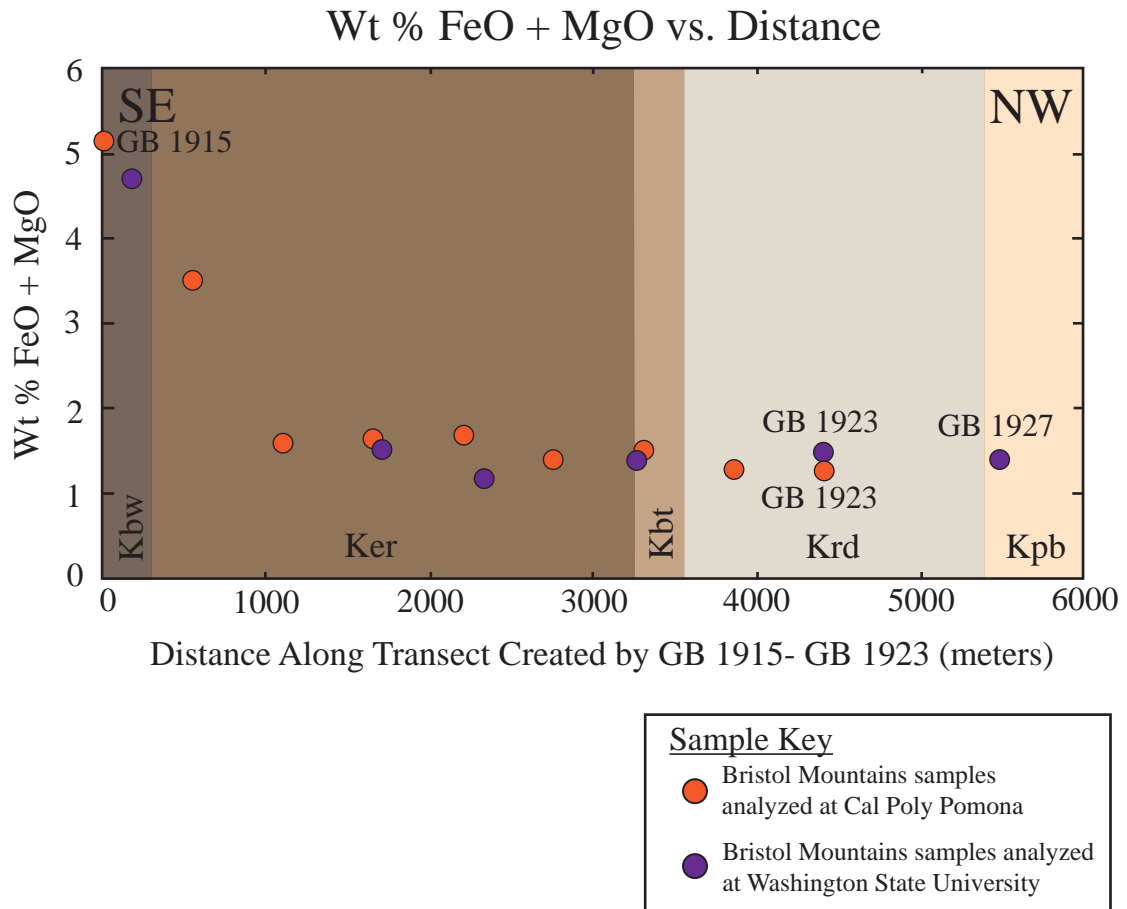


Figure 26. Plot showing how FeO + MgO concentrations change throughout the Bristol Mountains field site from the southeast to the northwest (from Kbw to Kpb). Orange samples were analyzed at Cal Poly Pomona (Fig. 7). Purple samples were analyzed at Washington State University (Fig. 7). Colors of each unit match those in figure 7.

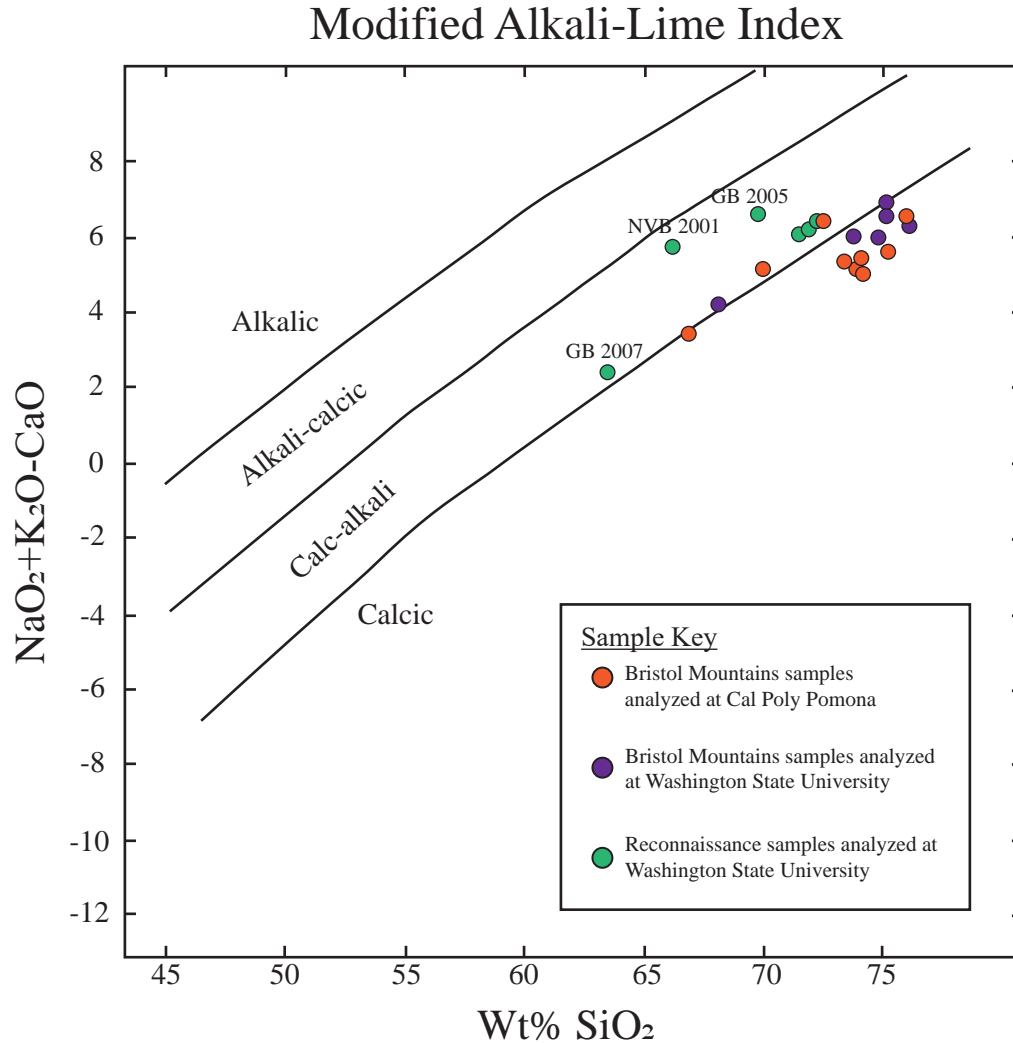


Figure 27. Modified Alkali-Lime Index. Orange samples are Bristol Mountains field site samples that were analyzed at Cal Poly Pomona (Fig. 7). Purple samples are Bristol Mountains field site samples that were analyzed at Washington State University (Fig. 7). Green samples are reconnaissance samples that were analyzed at Washington State University (Fig. 5).

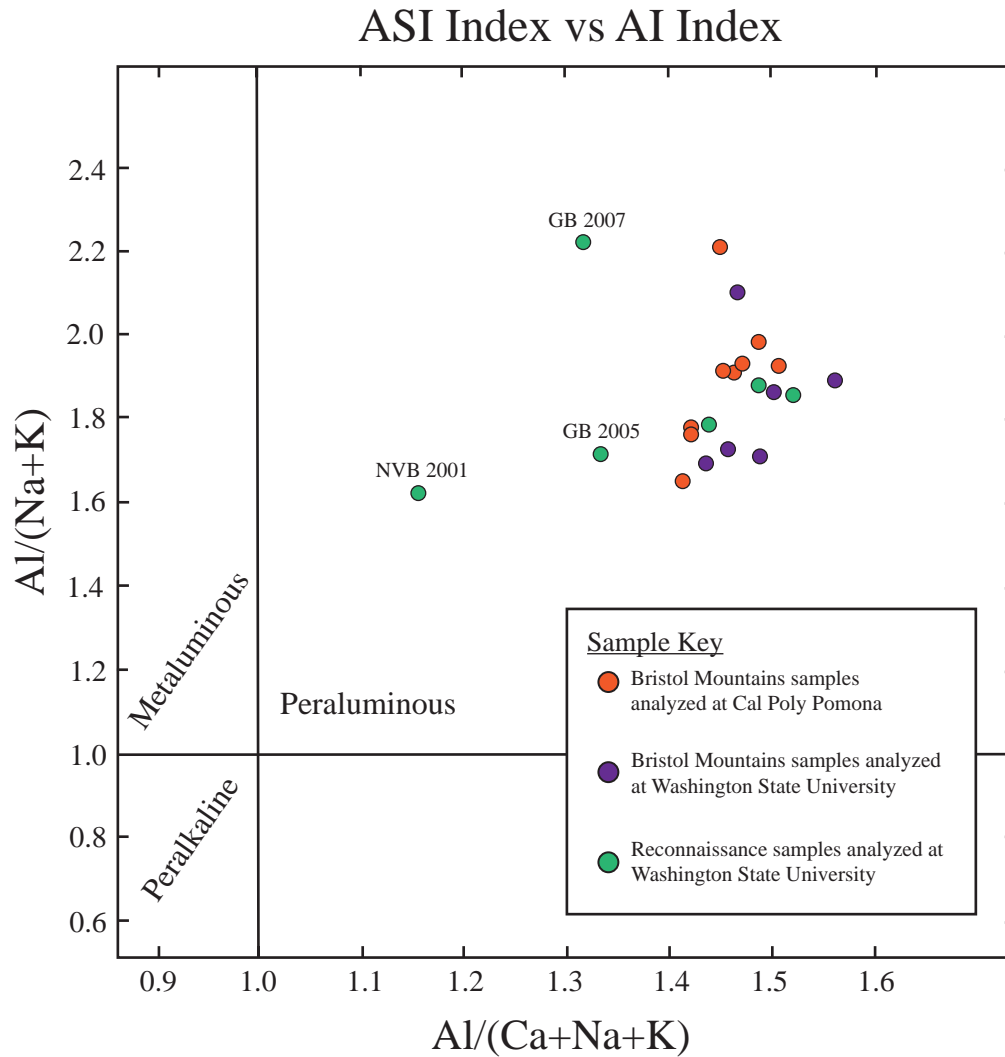


Figure 28. Aluminum saturation index vs alkalinity index. Orange samples are Bristol Mountains field site samples that were analyzed at Cal Poly Pomona (Fig. 7). Purple samples are Bristol Mountains field site samples that were analyzed at Washington State University (Fig. 7). Green samples are reconnaissance samples that were analyzed at Washington State University (Fig. 5).

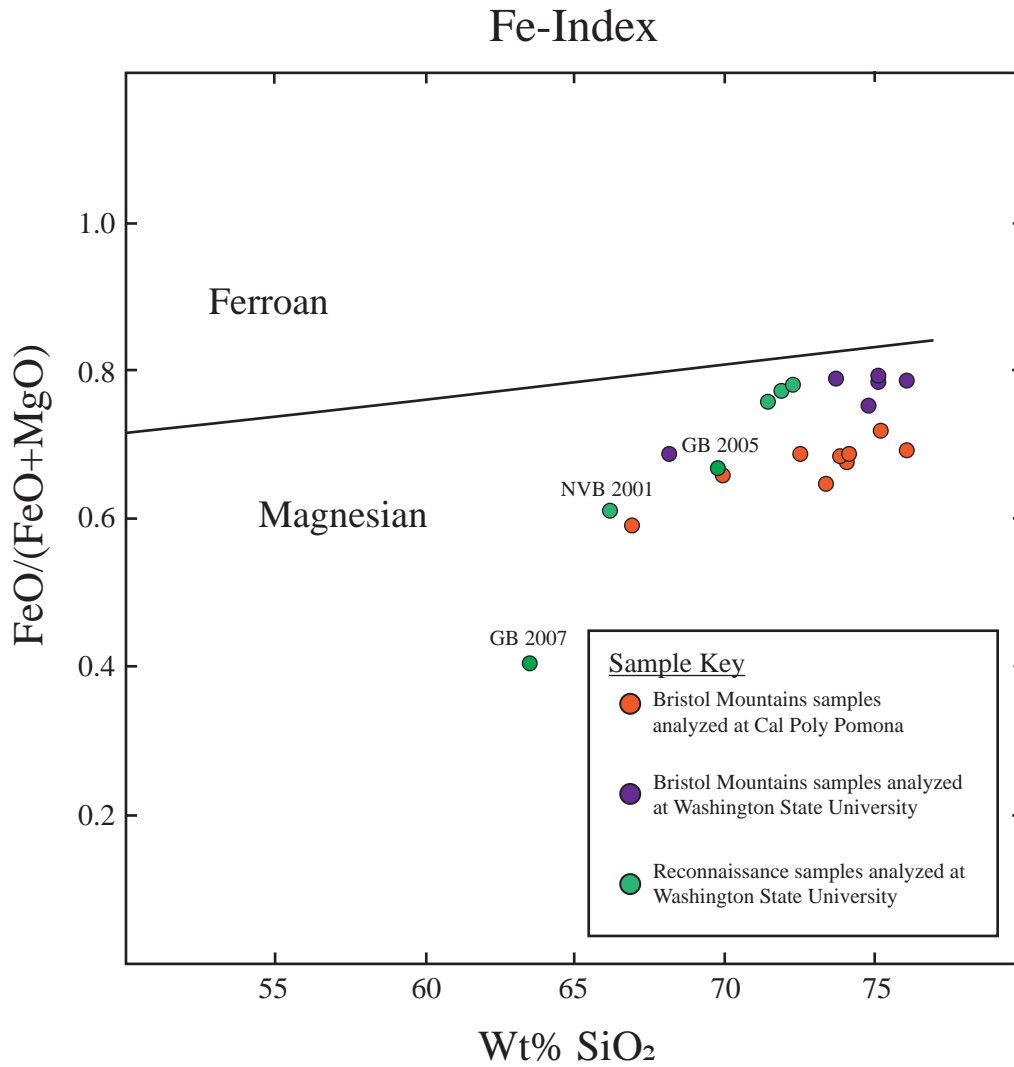


Figure 29. Fe-Index. Orange samples are Bristol Mountains field site samples that were analyzed at Cal Poly Pomona (Fig. 7). Purple samples are Bristol Mountains field site samples that were analyzed at Washington State University (Fig. 7). Green samples are reconnaissance samples that were analyzed at Washington State University (Fig. 5).

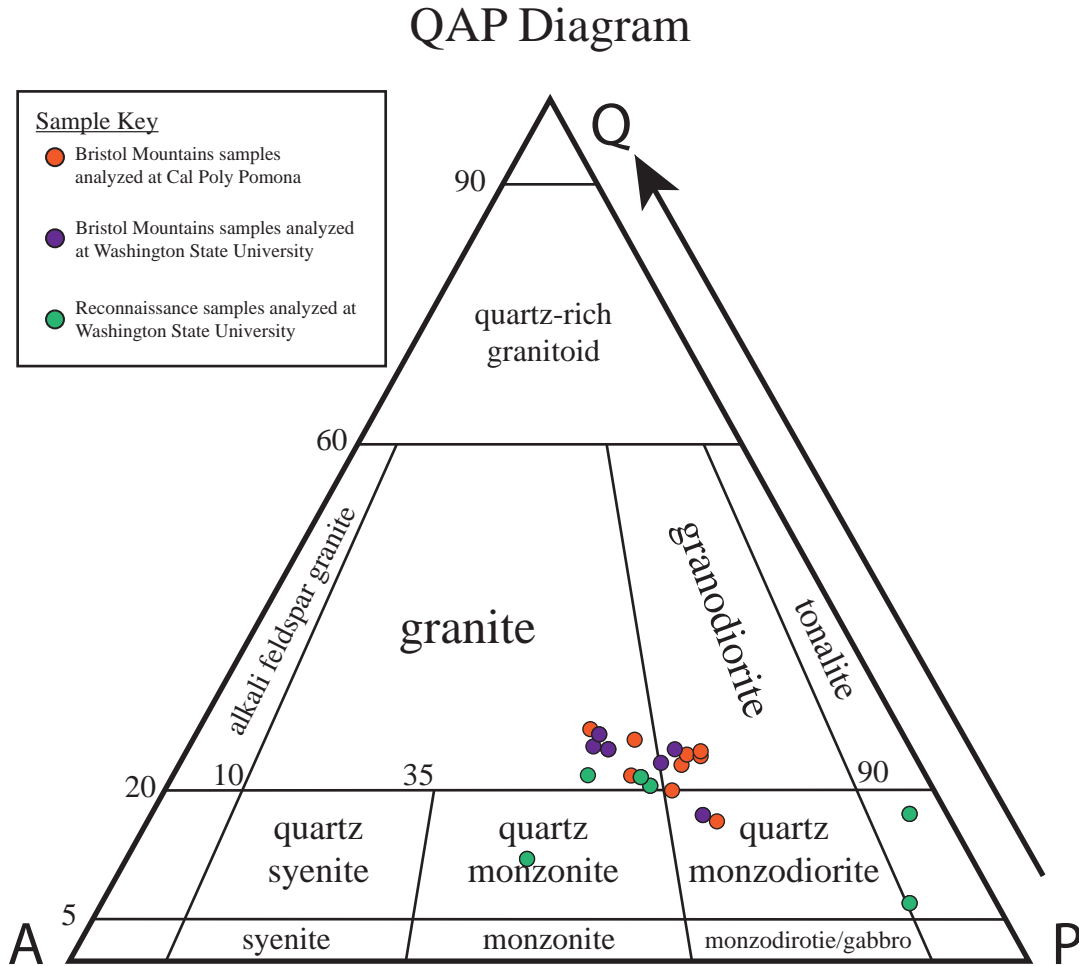


Figure 30. Quartz-Alkali Feldspar-Plagioclase Ternary Diagram. Orange samples are Bristol Mountains field site samples that were analyzed at Cal Poly Pomona (Fig. 7). Purple samples are Bristol Mountains field site samples that were analyzed at Washington State University (Fig. 7). Green samples are reconnaissance samples that were analyzed at Washington State University (Fig. 5). QAP diagram is based on the CIPW normative analysis of XRF data (Cross et al., 1902).

highest in Kbw, and decreases drastically while transitioning to Ker (Fig. 25). The lowest aluminum concentrations are in Ker (closer to Kbw) and is followed by increasing values towards the middle portion of Ker which level out and stay consistent through most of Ker, Kbt, Krd, and Kpb (Fig. 25). On the FeO +MgO vs. distance plot, there is a large decrease in the weight percentage of FeO + MgO as you transition from Kbw into Ker, then values remain relatively constant from Ker to Kpb (Fig. 26).

Trace-Element Geochemistry

Six samples collected from the Bristol Mountains mapping site (Fig. 7), and six samples from various locations in the Cady, Lava Bed, and Rodman Mountains (Fig. 5) were analyzed for trace-element data. All six samples were analyzed using inductively-coupled-plasma mass spectrometry (ICP-MS) at the Washington State University Peter Hooper GeoAnalytical Lab. The trace-element concentrations of samples are shown in Table 2. Trace-element data is plotted in several diagrams to compare samples to one another, and to other plutons of varying tectonic origins (Fig. 31-35). All five trace-element plots are derived from Hildebrand and Whalen, 2017 (Fig. 31-35). Throughout all five plots, Bristol Mountains samples plot in a relatively tight grouping along with two other reconnaissance samples (GB 2004, GB 2010) from the Rodman Mountains (Fig. 31-35). This grouping plots well within the “slab failure plutons” or “adakites” sections of the different diagrams, while the other four reconnaissance samples plot in the arc range, or in between arc and slab-tear ranges (Fig. 31-35).

Table 2. Trace-element concentrations of samples in parts per million (ppm). Purple samples are Bristol Mountains field site samples that were analyzed at Washington State University (Fig. 7). Green samples are reconnaissance samples that were analyzed at Washington State University (Fig. 5).

Element (ppm)	GB	GB	GB	GB	GB	GB	GB	GB	GB	GB	GB	NVB
	1901	1905	1907	1910	1923	1927	2004	2005	2007	2009	2010	2001
La	15.29	17.51	32.41	15.97	17.96	16.82	29.78	44.17	73.38	66.27	29.70	29.07
Ce	25.36	31.98	65.68	28.24	32.71	31.20	55.55	81.23	147.39	121.37	55.34	60.24
Pr	2.76	3.52	7.54	3.11	3.56	3.47	6.10	8.97	17.01	13.10	6.14	7.06
Nd	9.04	11.86	26.85	10.32	11.97	11.83	20.66	31.24	61.07	44.76	20.84	25.78
Sm	1.50	2.16	4.63	1.74	2.16	2.13	3.44	6.11	11.38	8.09	3.41	5.25
Eu	0.38	0.51	1.12	0.45	0.62	0.56	0.83	1.31	2.19	1.22	0.89	1.21
Gd	1.04	1.58	3.25	1.20	1.72	1.61	2.41	5.19	9.31	6.81	2.39	4.49
Tb	0.15	0.24	0.45	0.17	0.30	0.23	0.34	0.89	1.39	1.06	0.33	0.71
Dy	0.80	1.42	2.38	1.01	1.73	1.32	1.83	5.63	8.29	6.39	1.71	4.36
Ho	0.15	0.27	0.43	0.20	0.33	0.25	0.34	1.15	1.65	1.27	0.32	0.90
Er	0.41	0.71	1.10	0.53	0.91	0.68	0.91	3.16	4.40	3.38	0.87	2.51
Tm	0.06	0.11	0.15	0.09	0.14	0.10	0.13	0.45	0.64	0.52	0.12	0.38
Yb	0.46	0.70	0.98	0.58	0.88	0.66	0.85	2.74	4.03	3.28	0.84	2.50
Lu	0.08	0.11	0.15	0.10	0.14	0.10	0.13	0.41	0.62	0.52	0.13	0.38
Ba	506	992	880	1026	897	814	1269	1250	351	1110	1457	1698
Th	18.76	8.02	19.06	6.10	5.31	6.31	11.93	16.60	19.99	22.30	11.04	23.25
Nb	5.76	8.80	8.90	6.90	8.70	7.65	9.48	7.66	18.07	15.68	9.22	12.39
Y	4.47	7.92	11.61	5.95	9.74	7.22	9.56	31.02	42.48	35.07	9.20	23.97
Hf	2.98	2.96	4.79	2.83	3.04	2.92	4.13	3.23	8.76	6.29	4.29	5.44
Ta	0.45	0.77	0.62	0.55	1.26	0.69	0.80	0.74	1.08	1.54	0.75	1.06
U	1.59	0.57	2.72	0.69	0.91	0.73	1.58	3.57	2.80	2.52	1.50	3.84
Pb	19.76	22.39	16.80	20.44	21.08	20.33	23.92	12.69	13.46	25.78	21.50	7.87
Rb	156.1	115.9	113.7	108.0	119.5	101.3	143.1	139.8	49.8	190.8	135.3	188.7
Cs	0.90	0.68	1.20	1.01	1.15	0.81	1.42	1.00	0.29	3.13	1.61	3.57
Sr	303	347	553	323	435	472	468	752	539	270	543	419
Sc	1.4	2.2	6.2	2.2	1.9	2.0	2.3	5.8	15.2	5.5	2.8	9.8
Zr	91	99	176	98	103	104	147	113	340	223	154	198

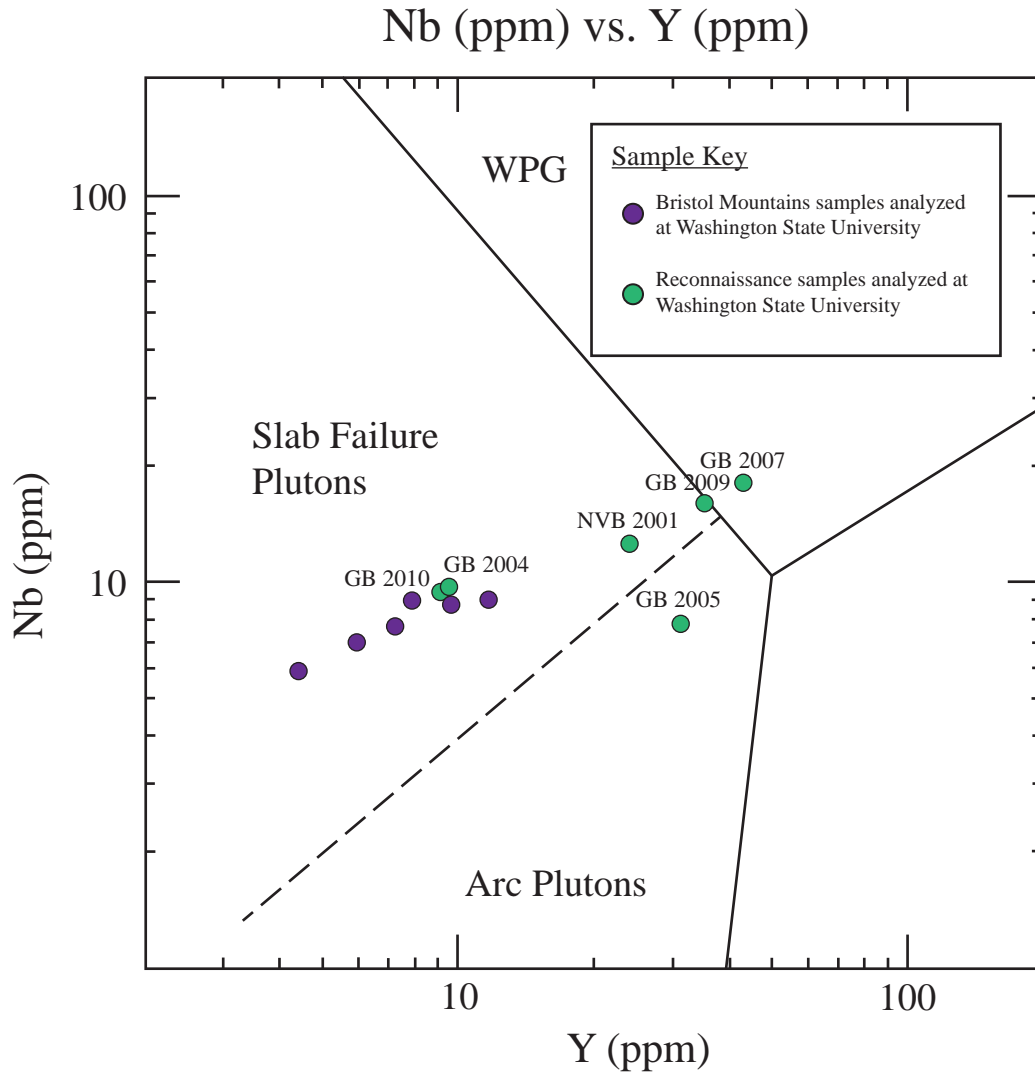


Figure 31. Nb (ppm) vs. Y (ppm). Purple samples are from the Bristol Mountains field mapping area (Fig. 7). Green samples are reconnaissance samples from the greater area surrounding Ludlow, CA (Fig. 5). Segmentations and groupings in the graph are defined by Hildebrand and Whalen (,2017).

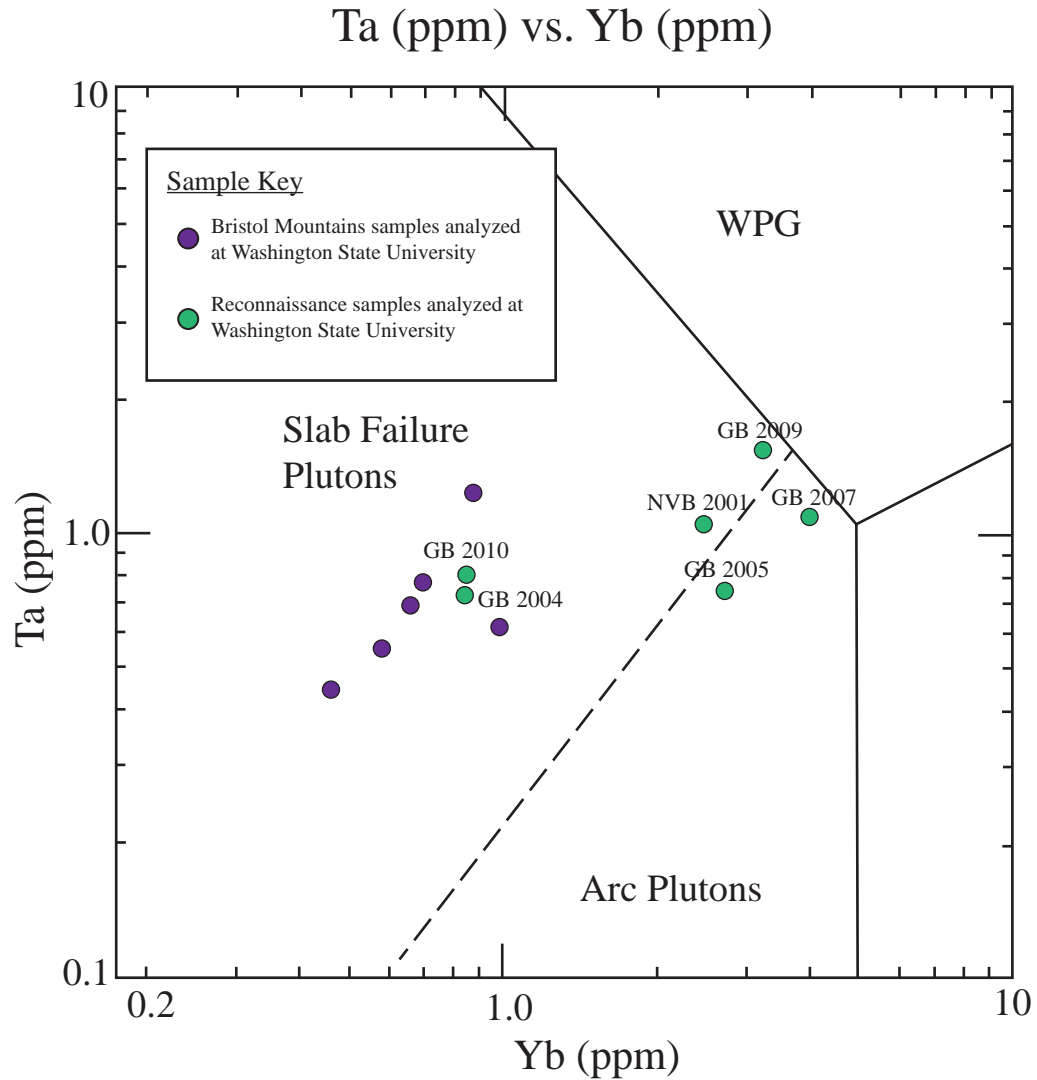


Figure 32. Ta (ppm) vs. Yb (ppm). Purple samples are from the Bristol Mountains field mapping area (Fig. 7). Green samples are reconnaissance samples from the greater area surrounding Ludlow, CA (Fig. 5). Segmentations and groupings in the graph are defined by Hildebrand and Whalen (,2017).

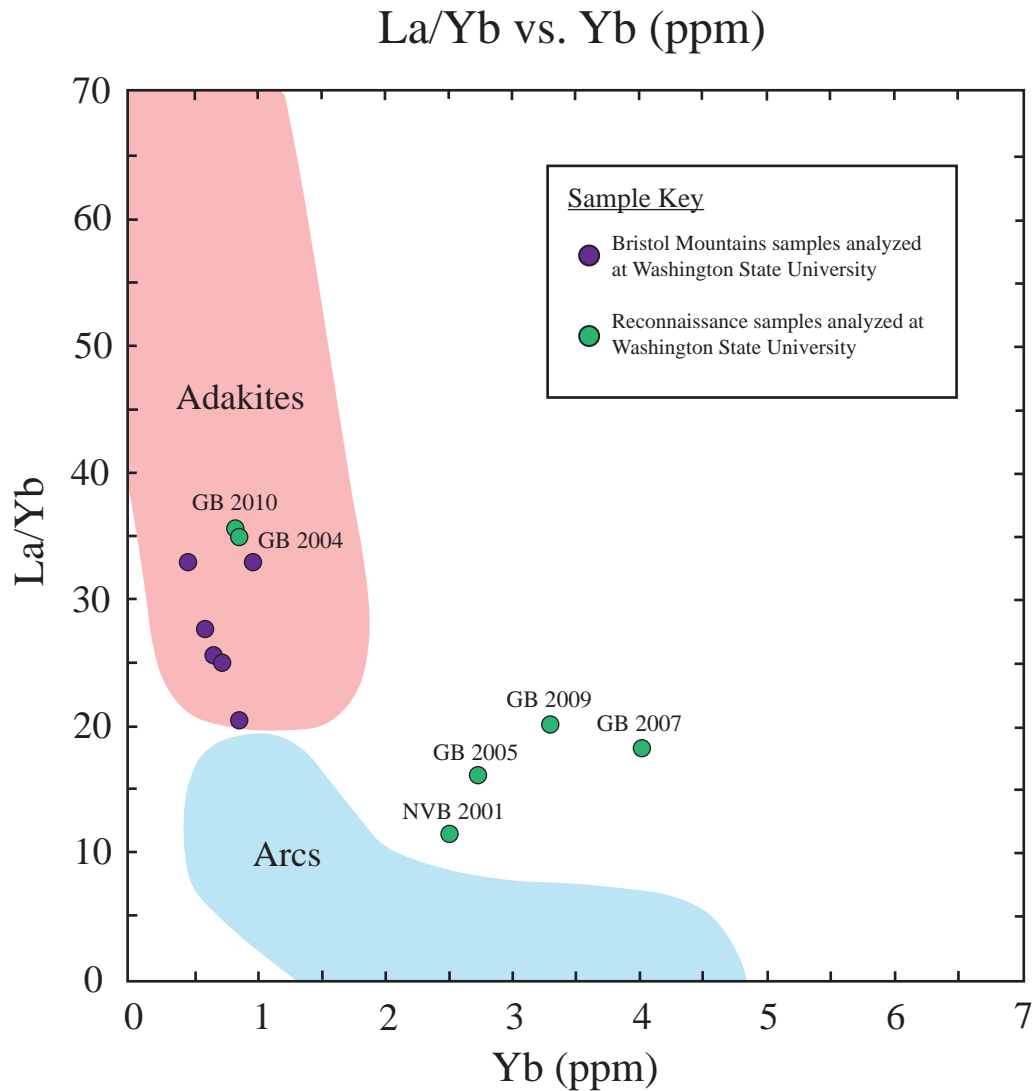


Figure 33. La/Yb vs. Yb (ppm). Purple samples are from the Bristol Mountains field mapping area (Fig. 7). Green samples are reconnaissance samples from the greater area surrounding Ludlow, CA (Fig. 5). Segmentations and groupings in the graph are defined by Hildebrand and Whalen (,2017).

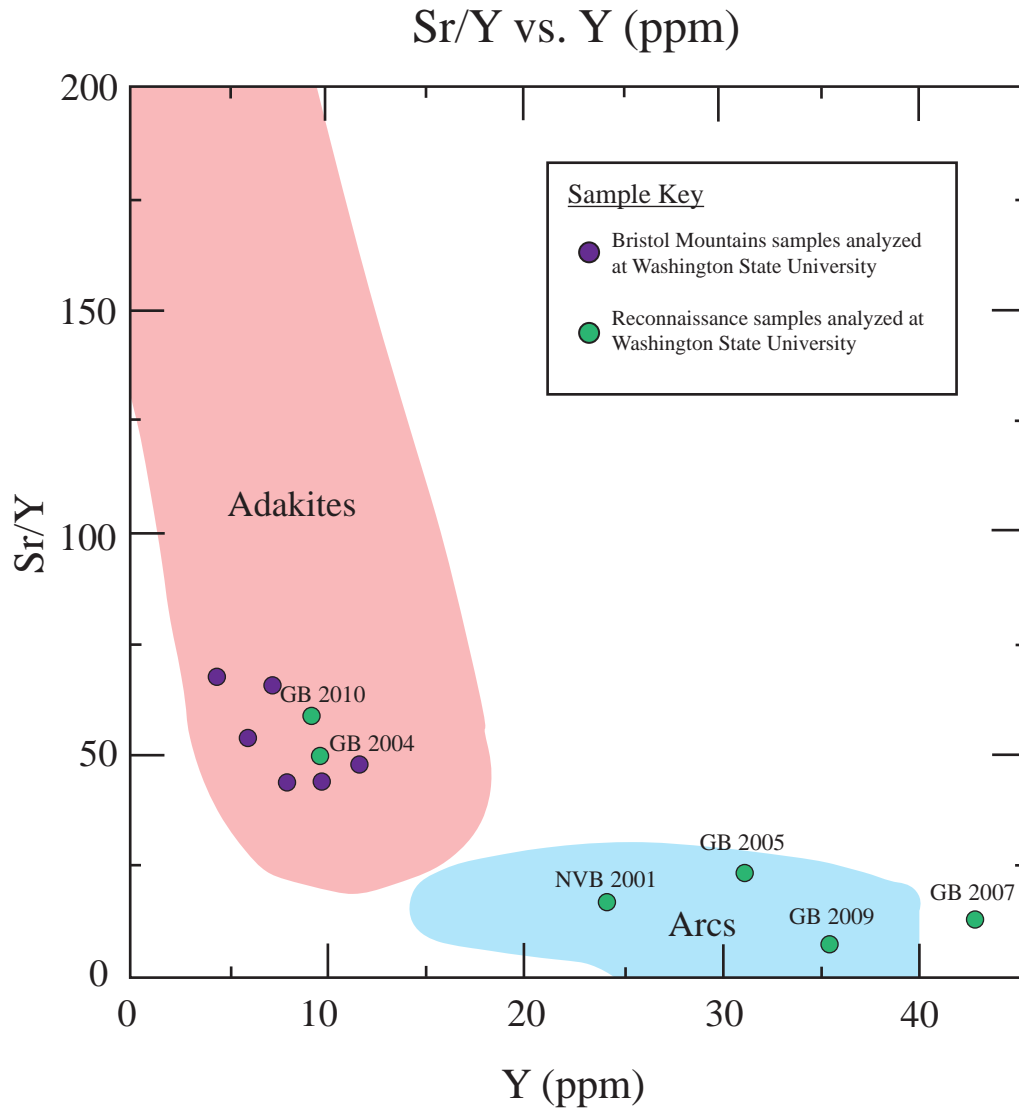


Figure 34. Sr/Y vs. Y (ppm). Purple samples are from the Bristol Mountains field mapping area (Fig. 7). Green samples are reconnaissance samples from the greater area surrounding Ludlow, CA (Fig. 5). Segmentations and groupings in the graph are defined by Hildebrand and Whalen (,2017).

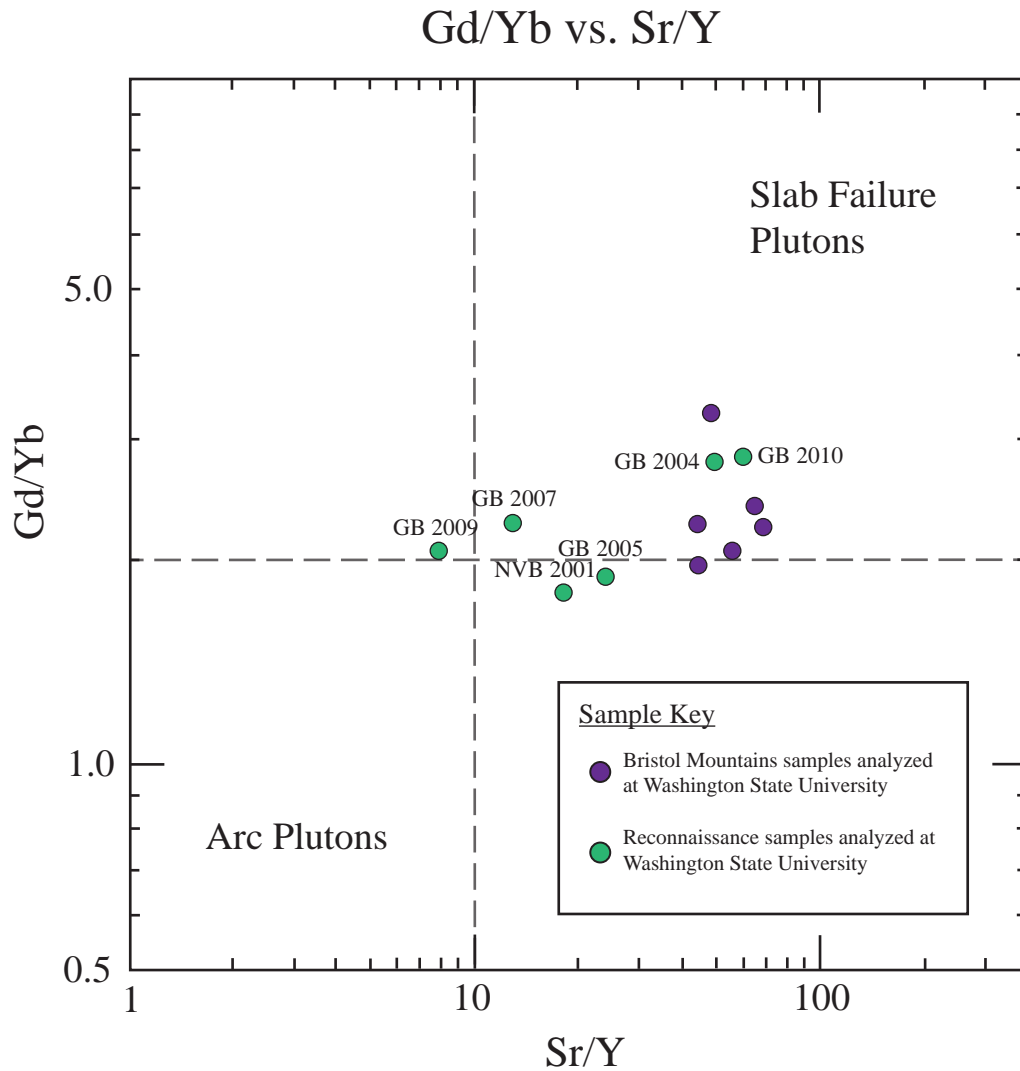


Figure 35. Gd/Yb vs. Sr/Y. Purple samples are from the Bristol Mountains field mapping area (Fig. 7). Green samples are reconnaissance samples from the greater area surrounding Ludlow, CA (Fig. 5). Segmentations and groupings in the graph are defined by Hildebrand and Whalen (,2017).

DISCUSSION

Intrusions in the Bristol Mountains

Field observations, U/Pb geochronology, and geochemical data support the hypothesis that the felsic units in the Bristol Mountains field site are part of a large cogenetic intrusive suite. A cogenetic intrusive suite is composed of plutonic rocks that form from a series of intrusions from a single magma source at different stages of the magma differentiation process (Fig. 4). The plutonic rocks created from this magma source will be similar in age, and geochemically related to one another if they truly form a cogenetic intrusive suite (e.g., Bateman, 1992; Coleman et al., 2004; Hirt, 2007; Van Buer and Miller, 2010) (Fig. 4). The five felsic units in the study area form a concentrically zoned pluton, where units are generally concave in shape, follow near parallel strike directions, and mostly have gradational contacts (Fig. 7). Gradational contacts between units may indicate that there was a continuous input of material from one magma source in this area, and that most units did not fully solidify before the next unit intruded (Fig. 7). Basement exposure in the Bristol Mountains is limited and does not clearly display the same set of nested, inward-younging units as seen in other intrusive suites, but the exposed units do have the similar concentric/concave shape that is seen in other intrusive suites (Bateman, 1992; Coleman et al., 2004; Hirt, 2007; Van Buer and Miller, 2010) (Fig. 4, 7). The gradational contacts between most Bristol Mountains units make determining the dip angle of most contacts difficult (Fig. 7, 8). The most distinct contact is that of Kbw and Ker, which is moderate to steeply dipping and at angles of about 55° to 80° (Fig. 7, 8). Dip angles between intrusions in other Cordilleran intrusive

suites have also been noted to dip steeply at non-gradational contacts (Hirt, 2007; Van Buer and Miller, 2010). (Fig. 4)

The Bristol Mountain intrusions are also compositionally similar but exhibit the slight changes in texture and mineralogy that are seen in most Cordilleran Cretaceous intrusive suites (Fig. 4, 7, 9-13). All five units are predominately granodiorite or granite with a consistently medium- to coarse-grained groundmass (Fig. 7, 9-13). Rocks with finer-grained, more equigranular textures are located on the outer southeastern edge of the pluton, while rocks with coarser-grained, porphyritic textures are located to the northwestern sections of the pluton (Fig. 7, 9-13). Other intrusive suites exhibit similar ranges of properties, and often are composed of granodiorite to granite intrusions that texturally evolve from equigranular to porphyritic from outer-to-inner intrusions (Bateman, 1992; Coleman et al., 2004; Hirt, 2007; Van Buer and Miller, 2010) (Fig. 4). Similarly, the mineralogical evolution of Bristol Mountains units is quite similar to those of other well studied intrusive suites (Fig. 7, 9-13). The Tuolumne, Whitney, and Sahwave intrusions all have relatively mafic outer intrusions with an abundance of mafic enclaves, and inner intrusions that contain K-feldspar megacrysts (Coleman et al., 2004; Hirt, 2007; Van Buer and Miller, 2010) (Fig. 4). Likewise, one of the outer most Bristol Mountains units (Kbw) has the most mafic composition and includes mafic enclaves, while the furthest unit from it also contains K-feldspar megacrysts (Fig. 7, 9, 13). These similarities between well studied intrusive suites with the Bristol Mountains intrusions are suggestive that the Bristol Mountains are also part of a large intrusive suite.

Geochemical data from the Bristol Mountains rocks also indicate that the five felsic units are related and part of one cohesive intrusive suite. Harker plots comparing

the units of the Bristol Mountains field site all exhibit generally linear trends, with three of the four producing very strong linear trends (Fig. 24). The K_2O vs SiO_2 Harker plot is not as strictly linear as the other three with a dip in K_2O around 74% SiO_2 but there is still a clear trend with samples of similar SiO_2 percentages plotting close to one another (Fig. 24). The linear trends in the Harker plots further support the idea that all five felsic units in the Bristol Mountains formed from one melt that gradually differentiated through time (Fig. 24). Bristol Mountain samples also plot in distinct groupings throughout several major-element oxide and trace-element geochemical plots (Fig. 27-35). On the modified alkali-lime index chart, Bristol Mountain samples are either calcic or calc-alkalic and are generally grouped close together (Fig. 27). On the aluminum saturation index vs alkalinity index chart, samples are all peraluminous and group together (Fig. 28). On the iron index chart, samples are all magnesian and form an analogous grouping (Fig. 29). Similarly, on the five plots comparing trace-element data, samples from the Bristol Mountains all plot in a distinct group (Fig. 31-35). These groupings of samples further suggest that the Bristol Mountains intrusions originated from a single source and therefore are cogenetically related intrusions.

Differentiation of the Bristol Mountains Intrusions

From the southeast to the northwest, the five mapped felsic units of the Bristol Mountains field site are referred to as Kbw, Ker, Kbt, Krd, and Kpb (Fig. 7, 9-13). The order and method of differentiation of these units is not clear cut, and there are multiple feasible scenarios that may adequately describe the differentiation process of rocks at this site. Based on geochronological data, unit 1 is undoubtedly the oldest unit at $77.2 \text{ Ma} \pm 1.0 \text{ Ma}$, but there is ambiguity when it comes to the order of crystallization of the other

four units (Fig. 7, 22). U/Pb zircon ages of units 2 through 5 from this study and Hess, 2017, all range from 74 to 75 Ma with an uncertainty of about one million years, making it difficult to definitively determine the order of crystallization based on radiometric ages alone (Fig. 7, 22). The two most likely scenarios that best describe differentiation of these units are as follows: (Scenario 1) Intrusions get younger towards the middle of the Bristol Mountains field site. (Scenario 2) Intrusions get younger from the southeast to the northwest.

Several pieces of evidence point to the possibility of units getting younger towards the middle of the field site (Scenario 1). Multiple compositional, mineralogical, and geochemical trends occur in such a way that a gradual change from unit to unit seems feasible if the intrusions young towards the middle of the field site (Fig. 7). For example, Kbw has the highest mafic content, followed by units Kpb, Krd, Kbt, and Ker (Fig 26). The change in mafic mineral percentages of outcrops and hand samples decreases quite steadily from Kbw to Kpb through Ker, with Kbw being composed of 25% mafics, Kpb being composed of 20% biotite, and Krd, Kbt, and Ker being composed of 15% biotite, 15% biotite, and 10% biotite respectively (Fig. 9-13, 26). An incremental change of ~5% mafic mineral content from unit to unit, suggests the possibility of the outer most units (Kbw and Kpb) being the oldest, with the inner most (Ker) being the youngest (Fig. 7).

Another piece of evidence is the way the five units plot in relation to one another on several geochemical plots (Fig. 7, 25, 30). From Kbw (southeast edge) to Ker (middle of site), there is a large increase in the silica content of samples, but from Ker (middle of site) to Kpb (northwest edge), silica content trends slightly downward (Fig. 7, 25). Potassium content also increases from Kbw to Ker, and decreased from Ker to Kpb (Fig.

7, 25). Similarly, on the QAP ternary diagram, Kbw, Krd, and Kpb plot as granodiorite, while Ker and Kbt plot as granite (Fig. 7, 30). Magmas typically increase in both SiO₂ and K₂O, while decreasing in CaO, during differentiation. This means that an example of a smooth transition in the rocks units formed by gradually changing melt would be quartz monzodiorite → granodiorite → granite. For this common differentiation pattern to be represented at the Bristol Mountains field site, the order oldest to youngest units would have to be Kbw, Kpb, Krd, Kbt, and finally Ker (Fig. 7, 22, 25, 30). It is, however, also possible that later additions of mafic magma could have disrupted the predictable pattern of un-interrupted differentiation, such that the magma composition did not become monotonically more felsic over time, as seen in other intrusive suites such as the Tuolumne, Whitney and Sahwave intrusive suites (Coleman et al., 2004; Hirt, 2007; Van Buer and Miller, 2010) (Fig. 4).

Scenario 2 involves intrusions younging from the southeast to the northwest (Fig. 7). Because Krd and Kpb are more mafic than Ker and Kbt while also being located closer to an edge of the Bristol Mountains field site, Scenario 2 would have to involve an addition of mafic magma that has prevented differentiation from proceeding in a consistent direction over time, as commonly observed in other intrusive (Bateman, 1992; Coleman et al., 2004; Hirt, 2007; Van Buer and Miller, 2010) (Fig. 4, 9, 13). The first piece of evidence to support this scenario is that units closer to the southeastern edge of the pluton have equigranular textures, and units become more porphyritic towards the northwest (Fig. 7, 9-13). Because of its equigranular texture, Ker was likely emplaced relatively near the edge of the pluton in proximity to cold wall rock, and therefore was the first to crystallize after Kbw (Fig. 7, 10). However, the coarser and more porphyritic

textures of Kbt, Krd, and Kpb might be the result of slower cooling if they were emplaced into a crust that had been already heated by the emplacements of Kbw and Ker (Fig. 7, 11-13). Additionally, unit 5 is composed of the highest percentage of and largest phenocrysts, which likely means that it was emplaced into the crust when it was at its relatively hottest temperature, making it the youngest of the five units (Fig. 7, 13).

The orientation of the contacts between Bristol Mountains units also suggests that units young from the southwest to the northwest of the site (Fig. 7). In concentrically zoned plutons, the oldest melt is often found on the edges of the pluton, and the youngest is found in the middle (Bateman, 1992; Coleman et al., 2004; Hirt, 2007; Van Buer and Miller, 2010) (Fig. 4). Therefore, a hypothetical fully exposed 2D representation of a zoned pluton would likely form ring shaped units where the youngest intrusions are nested within the oldest (Fig. 4). Exposure of a segment of most zoned pluton will create concave shaped units that young inwards (Fig. 4). The Bristol Mountains units all follow the same general concave nature, a shape which could be expected if only a portion of a ring-shaped intrusive suite were exposed (Fig. 7). This suggests that units get younger inward and towards the direction of concavity of the contacts and therefore are the youngest to the northwestern most portion of the Bristol Mountains site (Fig. 7). Although similar curved patterns can be replicated by ring dikes, in which case intrusions do not necessarily young in the direction of concavity; in the Cordillera, such patterns have most commonly been observed in gabbroic intrusions (e.g., Clemens-Knott and Saleeby, 1999), which are not what is observed here.

Although some geochemical trends support the case for units younging to the middle of the Bristol Mountains field site (Scenario 1), much stronger evidence exists to

back up the hypothesis that units young from the southeast to the northwest, but additions of mafic magma have prevented differentiation from proceeding in a consistent direction over time (Fig. 7, 9-13, 30). One of the strongest pieces of evidence is that the Bristol Mountains units have more porphyritic textures to the northwest, and even have K-feldspar megacrysts in Kpb, which are also found within the youngest units of the Tuolumne, Whitney, and Sahwawe intrusive suites (Coleman et al., 2004; Hirt, 2007; Van Buer and Miller, 2010) (Fig. 4, 7, 9-13). This textural pattern, as well as the concave shape of the Bristol Mountain units provides a stronger case for younging from the southeast to the northwest than for the hypothesis of younging to the middle of the field site (Fig. 7, 9-13).

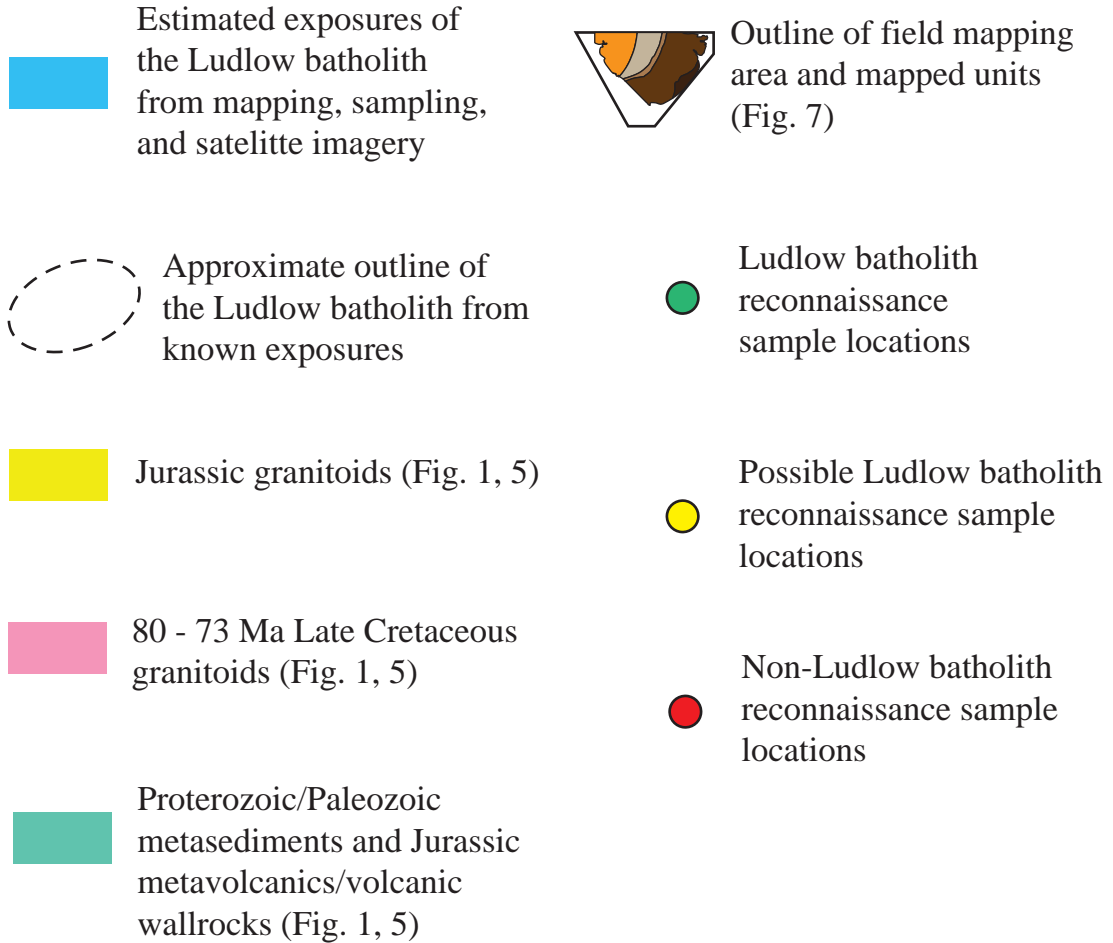
Defining the Ludlow Batholith

Six reconnaissance samples from the Rodman, Cady, and Lava Bed Mountains, were analyzed to determine if there are other locations of outcropping Ludlow batholith rock in the field area (Fig. 5). On most Harker plots, all six reconnaissance samples predominantly plot in a linear fashion with Bristol Mountains samples, although samples GB 2004, GB 2010, and GB 2009 plot closer to the grouping of Bristol Mountain samples than the other three reconnaissance samples (Fig. 24, 36). The only Harker plot that exhibits clear examples of reconnaissance samples being outliers is the K_2O vs. SiO_2 plot, where a few reconnaissance samples have relatively high potassium contents (Fig. 24). On the modified alkali-lime index (Fig. 27), the ASI index vs AI index (Fig. 28), and the Fe-index plots (Fig. 29), samples GB 2004, GB 2010, and GB 2009 all plot with Bristol Mountain samples while GB 2005, GB 2007, and NVB 2001 are predominantly outliers (Fig. 36). From the major-element oxide plots, samples GB 2005, GB 2007, and



Figure 36. Locations of exposed Ludlow batholith rock in the Bristol and Rodman Mountains, and the approximate outline of the Ludlow batholith. Yellow, pink, and green blobs are from figures 1 and 5. Map key is on the next page.

Figure 36 Key



NVB 2001 can be ruled out as being related to Bristol Mountains units, while samples GB 2004, GB 2010, and GB 2009 cannot (Fig. 24, 27-30, 36). On trace-element plots, only samples GB 2004 and GB 2010 from the Rodman Mountains consistently plot with the grouping of samples Bristol Mountains (Fig. 31-36). GB 2009 from the Cady Mountains does not plot with the BM samples, despite doing so in most major-oxide geochemical plots (Fig. 24, 27-36). Samples GB 2005, GB 2007, and NVB 2001 are again obvious outliers to the Bristol Mountains grouping of samples (Fig. 24, 27-36). Samples GB 2004 and GB 2010 from the Rodman Mountains are therefore determined to be the samples most likely related to the Bristol Mountains samples, while GB 2009 from the southern Cady Mountains is possibly related (Fig. 36). As of now, these related samples define the extent of known outcroppings of the Ludlow batholith (Fig. 36).

The Bristol Mountains field site and the segment of the Rodman Mountains determined to be part of the Ludlow batholith, possibly represent two opposite sides of this large intrusive suite (Fig. 36). Most of the intervening area is covered by Cenozoic volcanic and sedimentary strata, which makes more detailed observations about most of the proposed Ludlow batholith nearly impossible (Fig. 36). From field observations and geochronological data, it can be determined that the Bristol Mountain units represent the very northeast edge of the Ludlow batholith (Fig. 7, 22). By comparison to the outer most units of other intrusive suites (Bateman, 1992; Coleman et al., 2004; Hirt, 2007) (Fig. 4), the medium-grained equigranular texture and the inclusion of elongate mafic enclaves in the oldest Bristol Mountains unit (Kbw) indicates that this unit likely crystallized close to, or in contact with, the wall rocks surrounding the batholith, even though the area where these wall rocks would be exposed is buried beneath Cenozoic strata (Fig. 7, 9, 19,

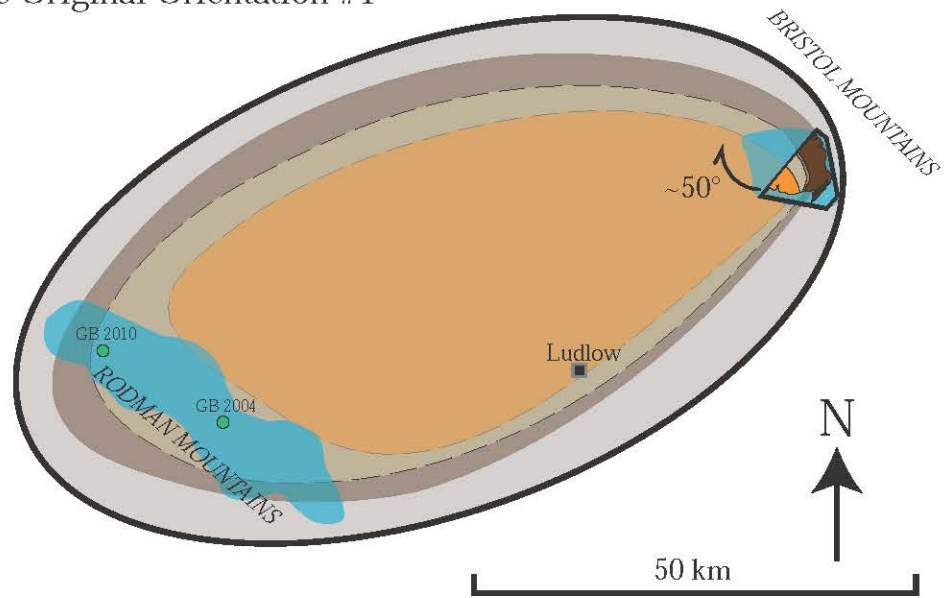
22, 36). The fine-grained equigranular texture on the edge of the Bristol Mountains site in Kbw is an indicator of relatively fast cooling, which can occur when melt is in contact with cold wall rock (Fig. 7, 9). Elongate mafic enclaves may also indicate the pluton margin or bottom is nearby because there may be higher shear stresses generated by magma flow dragging against the pluton wall than there would be in the inner part (Fig. 19, 36). Also, being denser than the surrounding felsic magma, mafic enclaves are more likely to be clustered near the bottom, or along the edges where peripheral sources of mafic magma are most likely to intrude into the pluton, as is seen in other intrusive suites (Bateman, 1992; Coleman et al., 2004; Hirt, 2007; Van Buer and Miller, 2010) (Fig. 4, 7, 19, 36).

The two samples from the Rodman Mountains overlap with the Bristol Mountain samples on all geochemical plots, and therefore are likely to represent the same units as those found in the Bristol Mountains (Fig. 24, 27-36). One possible way this can occur is if the Rodman Mountains segment of the Ludlow batholith is the outcropping of the opposite side of the Bristol Mountains units in an ellipsoidally shaped zoned pluton, about 68 by 36 km in dimension (Fig. 36). Many intrusive suites of similar age, such as the Tuolumne, Whitney, or Cadiz Valley intrusive suites, have similar patterns over similar sizes of up to 80 km (Coleman et al., 2004; Hirt, 2007; Howard, 2002) (Fig. 4, 36). In its current orientation, the Bristol Mountains intrusions get younger to the northwest, not to the southwest, which is the direction of where the Rodman Mountains are in relation to the Bristol Mountains (Fig. 7, 36). Counterclockwise tectonic rotations of up to 50° have been documented in nearby areas of the Central Mojave (Glazner et al., 2002; Luyendyk, 1991; Ross et al., 1989; Wells and Hillhouse, 1989), and therefore it is

possible for significant rotation of the Bristol Mountains site to have occurred since crystallization, which would be more consistent with the expected younging direction (Fig. 37). Alternatively, intrusive suites can have irregular shapes and zoning patterns that are locally misaligned to the regional pluton elongation direction, such as the patterns seen in the Tuolumne Intrusive Suite (Coleman et al., 2004) (Fig. 4, 37). From the areas of known exposures and satellite imagery, the Ludlow batholith can be defined by its northeastern boundary in the Bristol Mountains, and its southwestern boundary in the Rodman Mountains (Fig. 36).

Widespread Cenozoic cover conceals most of the Ludlow batholith, but gravity data may aid in determining a more accurate and detailed boundary for the batholith (Fig. 36, 38). An isostatic residual gravity map from Langenheim and Jachens (,2002) outlines a low-gravity anomaly in the area that encompasses the known exposures of the intrusive suite in the Bristol and Rodman Mountains (Fig. 38). Granodiorite is a relatively low-density material compared to the average continental crust and therefore a thick granodiorite batholith may be the cause of the low-gravity anomaly in the area around Ludlow, CA (Fig. 38). One limitation to defining the Ludlow batholith from gravity data alone is that it is impossible to tell apart felsic plutonic rocks of different ages, therefore it is possible that part of the low-gravity anomaly is created from felsic intrusions unrelated to the Ludlow batholith (Fig. 38). This may also be the reason why there is no real western boundary to the Ludlow batholith seen on the isostatic residual gravity map, since the western Mojave is composed almost entirely of felsic batholiths (Fig. 1, 38). The Granite and southern Bristol Mountains make up a large portion of the gravity anomaly located to the east of the Bristol Mountains field site (Fig. 38.). The Granite

Possible Original Orientation #1



Possible Original Orientation #2

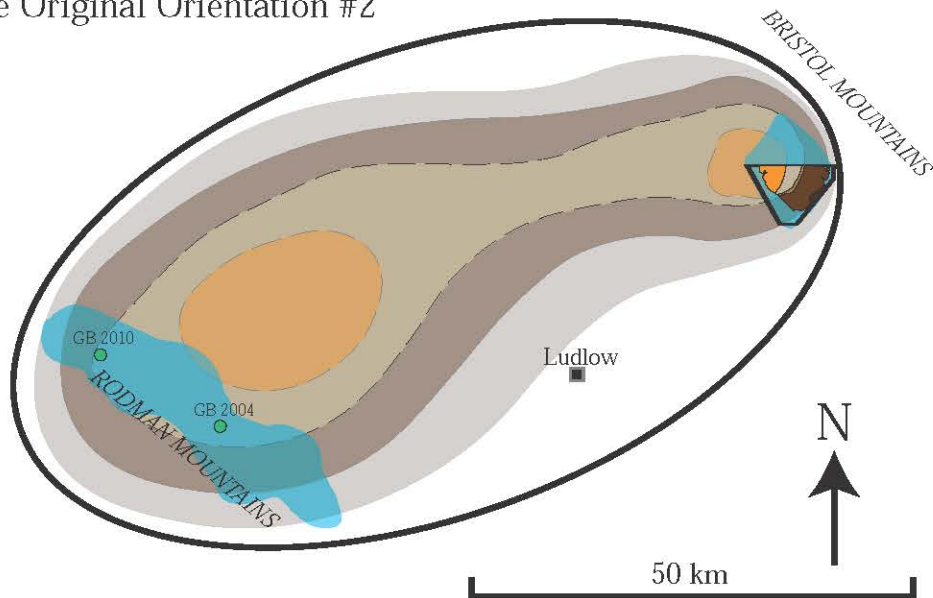


Figure 37. Possible orientations of the Ludlow batholith at time of emplacement. Widespread Cenozoic cover makes it difficult to determine the exact shape of the batholith. Orientation #1 shows the Bristol Mountain units before possibly being rotated up to 50° during the Cenozoic. The blue blobs seen in both “possible orientations” are from figure 36.

Mountains in particular make a distinctly large blue/green low-density blob on the gravity map (Fig. 38). The northern part of the Granite Mountains is Jurassic in age, but the southern portion has been dated in the range of 78-75 Ma, meaning that it is similar in age to, and may be part of the Ludlow batholith (Hess, 2017) (Fig. 22, 38). The southern Bristol Mountains have not been dated, and the rocks there may or may not be related to the felsic intrusions of the Ludlow batholith (Fig. 7, 38). Additionally, some of the Jurassic outcrops throughout the entire research area could be overlaying the Ludlow batholith at depth (Fig. 38). Therefore, the presence of Jurassic outcrops does not necessarily equate to the absence of Ludlow batholith at depth in those specific locations (Fig. 38). Although the orientation of the plutonic subunits beneath the Cenozoic cover cannot be known, the boundaries of the intrusive suite at depth likely mirror certain portions of the low-gravity anomaly, shown in figure 38.

Rapid Melt Intrusion into the Crust

Widespread Cenozoic cover in the Central Mojave makes determining the rate of melt intrusion difficult, as the boundaries of the intrusion are mostly unknown (Fig. 36-38). In the previous section, the boundary of the Ludlow batholith was interpolated from known exposures of the batholith and gravity data (Fig. 36-38). When defining the batholith using the known exposures alone (minimum estimate), the Ludlow batholith probably covers an area of about 1,900 km² (Fig. 36), and when it is defined based on the available gravity data (maximum estimate), the intrusive suite covers an area of about 2,600 km² (Fig. 38). Furthermore, known radiometric ages in the Bristol Mountains range from approximately 77.2 Ma to 74.6 Ma, meaning that magma was emplaced into the crust for at least 2.6 million years (Fig. 7, 22). To determine the rate melt intrusion, it is

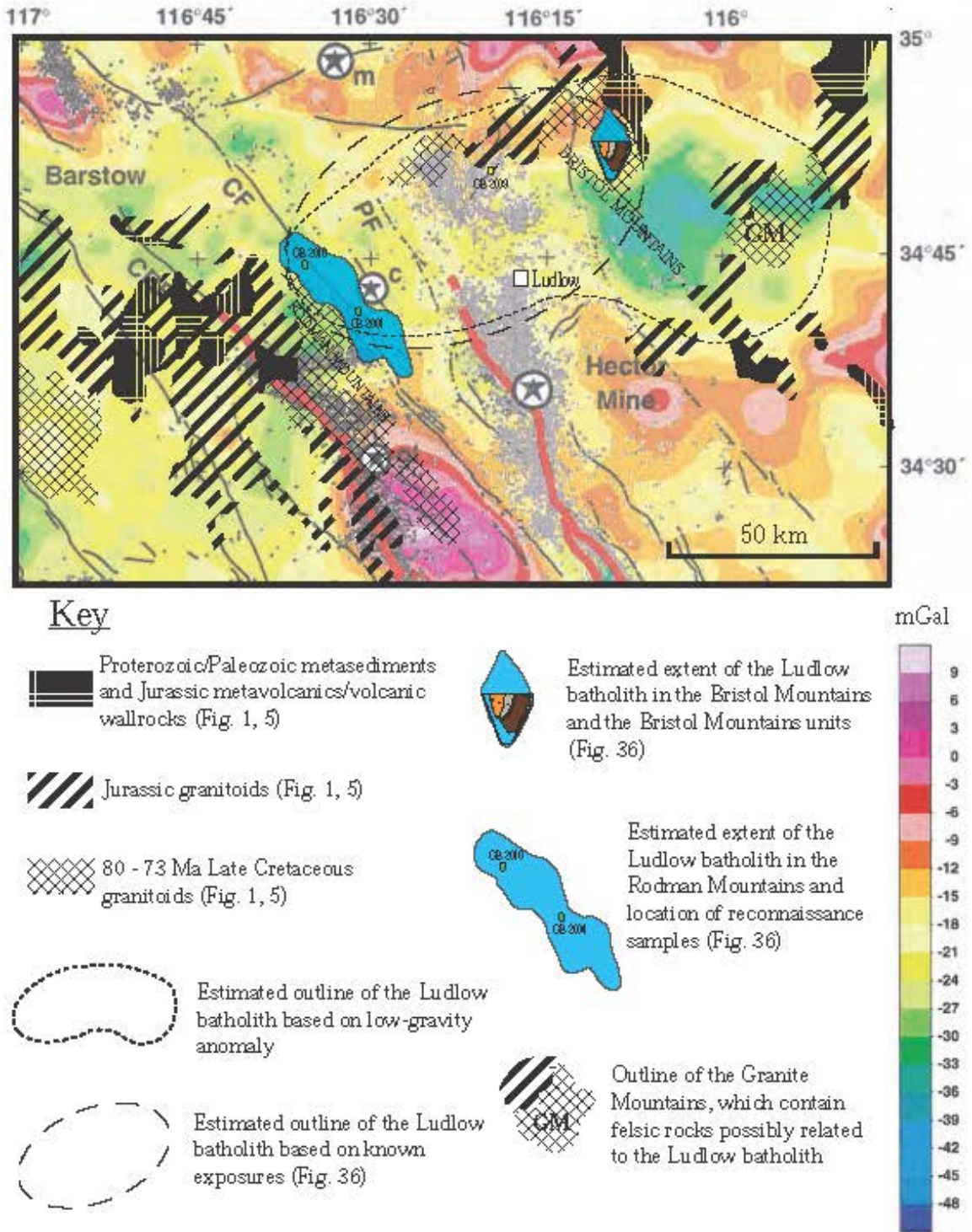


Figure 38. Isostatic residual gravity map showing the possible extent of the Ludlow batholith based on gravity data. Adapted from Langerheim and Jachens, 2002.

necessary to know the full three-dimensional volume of the intrusive suite, and although it is unknown for the Ludlow batholith, data from analogous magmatic bodies can be used to help make estimates. One such analog is located to the south of the Bristol Mountains, in Joshua Tree National Park. Joshua Tree National Park is located within a tilted crustal section of the Mesozoic magmatic arc (Needy et al., 2009). The orientation of this crustal section allows for semi-continuous exposure of a variety of arc related rocks at different depths. In the eastern transverse ranges, this crustal section extends from volcanic and sedimentary units in the east to a mid-crustal magmatic sheeted complex in the west, where it is truncated by the San Andreas fault (Needy et al., 2009). Not unlike the rocks in the Bristol Mountains, the rocks in Joshua Tree National park have been radiometrically dated to as young as 72 Ma, meaning that both areas are composed of rocks that formed post arc-cessation at 80 Ma (Needy et al., 2009). Because of the proximity to one another in time and space, the rocks in both the Bristol Mountains and Joshua Tree National Park may have similar tectonic and magmatic origins, making them somewhat comparable. Needy (et al., 2009) notes that Late Cretaceous granodiorite intrusions, which have similar textures and geochemical characteristics to units of the Ludlow batholith (Fig. 9-13, 27-30), are continuously exposed at paleodepths ranging from 5 to 15 km. Therefore, it is estimated that the Ludlow batholith has a thickness of about 10 km. Assuming the batholith has generally constant thickness throughout, and that it is best defined by the outline of the batholith shown in figure 36, the total volume of melt emplaced is roughly 19,000 km³. When the low gravity anomaly in the central Mojave is used to define the Ludlow batholith (Fig. 38), the total volume of melt emplaced is roughly 26,000 km³. From the estimated extents and known radiometric ages

of the Ludlow batholith, as well as the thickness of analogous sections of Joshua Tree National Park, it is estimated that the melt intruded at a rate that ranges somewhere between 7,300 to 10,000 km³/Ma (Fig. 22, 36, 38). Compared to the similarly sized intrusive suites from the Sierra Nevada batholith, such as the Sahwave intrusive suite which intruded into the crust of a rate of about 2,200 km³/Ma, the rate of melt emplacement of the Ludlow batholith is relatively rapid (Van Buer and Miller, 2010) (Fig. 4).

The Case for Slab-Tear Magmatism in the Central Mojave

The origins of Late Cretaceous plutons in the Mojave Desert have not been extensively researched and their relation to other Mesozoic magmatic arc rocks throughout other parts of California and the Western United States is not well understood. Still, these plutons represent a key transition in the tectonic history of the U.S. Cordillera and need to be studied to fully understand the evolution of the Mesozoic magmatic arc. Normal arc magmatism involving mantle-wedge-derived melt ceased throughout the Sierra Nevada and Peninsular ranges around 80 Ma, when magmatism migrated eastward due to the decreasing angle of subduction of the Farallon plate (Chen and Moore, 1982; Kistler and Peterman, 1973; Irwin and Wooden 2001) (Fig. 3). The subduction of the large igneous province, known as the Shatsky conjugate, that was embedded within the Farallon plate, is generally thought to have been the catalyst for the drastic change in subduction angle and the eastward migration of arc magmatism that occurred after magmatic arc cessation in the Sierras (Saleeby, 2003; Liu et al., 2010) (Fig. 2, 3). The youngest Late Cretaceous arc plutons within the back-arc setting of the Mojave Desert were intruded close to the same time this igneous province was subducted and may be

representative of the changing tectonic situation of Western United States during Laramide disruption. It is unlikely that the Ludlow batholith was a product of normal arc magmatism because of the low-angle orientation of the Farallon plate at the time, and therefore may have a complex tectonic origin that has not yet been thoroughly explored in published literature (Fig. 2, 3).

Whole-rock trace-element data suggests that rock samples from both the Bristol and Rodman Mountains have trace-element concentrations analogous to samples of several known examples of slab-tear magmatism (Fig. 31-35). Geochemical discrimination plots developed by Hildebrand and Whalen (2017), compare various combinations of rare-earth elements (REEs), as well as other trace elements, to create a method of separating arc-derived magmas from slab-tear derived magmas (Fig. 31-35). Several of these trace-element plots consistently form discrete clusters of data when well-constrained examples of both slab-tear and arc magmatism are plotted (Fig. 31-35). For the most part, these empirically derived plots do not show any ambiguous overlap between clusters of known arc and slab-tear samples, and therefore can be used to help determine a probable tectonic and magmatic origin for samples collected for this study (Fig. 31-35). Hildebrand's use of these diagrams to classify all of the large late Cretaceous Cordilleran batholiths as slab-tear related remains controversial. On all five trace-element plots, all samples from the Bristol Mountains cluster and plot well within the range of values associated with slab-tear plutonism (Fig. 31-35). Only one Bristol Mountains sample plots on the border of, or just outside of the "adakites" or "slab tear pluton" data range on any of the plots (Fig. 31-35). These plots are the La/Yb vs. Yb (ppm) plot (Fig. 33) and the Gd/Yb vs. Sr/Y plot (Fig 35). In general, the Bristol and

Rodman Mountain samples follow the trace-element compositions of several well-constrained data sets from known slab-tear plutons (Fig. 31-35).

Although the trace-element plots of Hildebrand and Whalen (2017) have been created based on empirical data separating known arc and slab-tear plutons, the reason these plots work is likely due to the presence or absence of garnet during partial melting or fractional crystallization (Fig. 31-35). Garnet is only stable in the peridotite lithologies at depths of 200 km or below and therefore melts derived from such a depth will be more depleted in elements compatible with garnet than melts that originated closer to the surface (Green and Ringwood, 1967; O'Hara et al., 1971). In particular, rare-earth elements (REEs) are helpful in determining the effect of garnet stability, because light rare-earth elements partition more strongly into the melt phase due to their large ionic radii, while heavy rare-earth elements favor remaining in the mineral garnet (Johnson, 1998; Shimizu and Kushiro, 1975). Because of this, melts derived from mantle depths below 200 km will be depleted in heavy REEs, such as Yb and Y, and will be relatively enriched in lighter REEs. Similarly, Sr, which is a substitute for Ca in plagioclase, more strongly partitions to the mineral plagioclase. Therefore, melts derived from the asthenosphere will be relatively enriched in Sr when compared to arc-derived melts that contain high amounts of residual plagioclase. The trace-element ratios of La/Yb (Fig. 33) and Gd/Yb (Fig. 35) have been noted to reflect the effects of residual garnet in a melt, while the ratio of Sr/Y (Fig. 34, 35) reflects the effects of residual garnet without residual plagioclase (Hildebrand and Whalen, 2014 and 2017). On the La/Yb vs. Yb (ppm) (Fig. 33), the Sr/Y vs. Y (ppm) (Fig. 34), and the Gd/Yb vs. Sr/Y (Fig. 35) plots, Bristol Mountains samples have elevated ratios of La/Yb, Gd/Yb (which compare relatively light

rare earth elements to relatively heavy rare earth elements), and Sr/Y compared to samples of known arc plutons. Thus, the Bristol and Rodman Mountain samples are relatively enriched in light REEs and strontium and depleted in the heavier REEs when compared to most arc-related samples (Fig. 33-35). These elevated ratio values indicate a significant effect of both garnet-present and plagioclase-absent melting, and therefore these samples most likely are derived from melt that originated at a much greater depth than arc-related melts, which form from melting of the mantle wedge at about 150 km depth (Fig. 33-35).

There are environments in which garnet may be stable at shallower depths in non-peridotite lithologies, such as in garnet-pyroxenite residues from re-melted underplated basalts (Ducea, 2001; Saleeby, 2003), therefore making it possible for relatively shallow depth heavy-REE-depleted melts to form. However, near the time of emplacement of the Ludlow batholith, subduction was so shallow that it scraped off the lower lithosphere and replaced it with subduction-channel schist (e.g., Grove et al., 2003; Jacobson et al., 2011; Chapman et al., 2010) (Fig. 3). It is difficult to imagine a situation where the heavy-REE-depleted melts of the Ludlow batholith were created in an arc setting under these conditions. Slab-tear magmatism often involves asthenospheric upwelling from depths below 200 km, and therefore will contain significant residual garnet and be depleted in heavy REEs, as demonstrated by samples from the Bristol and Rodman Mountain samples (Fig. 33-35).

The four outlier reconnaissance samples (GB 2005, GB 2007, GB 2009, and NVB 2001) do not consistently plot in the same section of the five trace-element plots, and often plot within multiple sections or outside of any distinctive section at all (Fig. 31-35).

In a back-arc setting such as the central Mojave, melts must rise through thicker sections of crust when compared to melts in the middle of the arc, and therefore will have slightly different chemical compositions due to the higher level of crustal assimilation caused by the lengthier period spent rising and interacting with crustal rock. The inherited zircon grains found in several Bristol Mountains samples are direct evidence of such assimilation (Fig. 22, 23). All five samples that have been radiometrically dated contain inherited zircon grains that range in age from Early Cretaceous and Jurassic up to Proterozoic (Hess, 2017; this study) (Fig. 22, 23).

Slab-Tear Model for the Origin of the Ludlow Batholith

The preferred model for evolution of the Mesozoic magmatism within the Mojave Desert involves several stages that ultimately conclude with slab-tear magmatism (Fig. 39). Stage 1 (100-92 Ma) includes normal arc magmatism in the Central Mojave (Fig. 39). This form of magmatism is comparable to that found throughout the southern Sierra Nevada and the Peninsular Ranges. Stage 2 (91-82 Ma) marks the transition from normal-angle subduction of the Farallon plate, to increasingly low-angle subduction due to the incipient subduction of the buoyant oceanic plateau known as the Shatsky conjugate (Liu et al., 2010) (Fig. 2, 39). Underplating of the Rand and Pelona schists beneath the Mojave region and the southern Sierra Nevada batholith also begin during this time as they are thought to be related to the onset of flat-slab subduction (e.g., Grove et al., 2003; Jacobson et al., 2011; Chapman et al., 2010) (Fig. 39). The end of stage 2 coincides with the cessation of the magmatic arc in the Sierra Nevada and Peninsular Ranges batholith at 80 Ma (Chapman et al., 2016; Chen and Moore, 1982) (Fig. 39). Stage 3 (about 81 Ma) defines the period in the central Mojave Desert where magmatism was lacking, likely

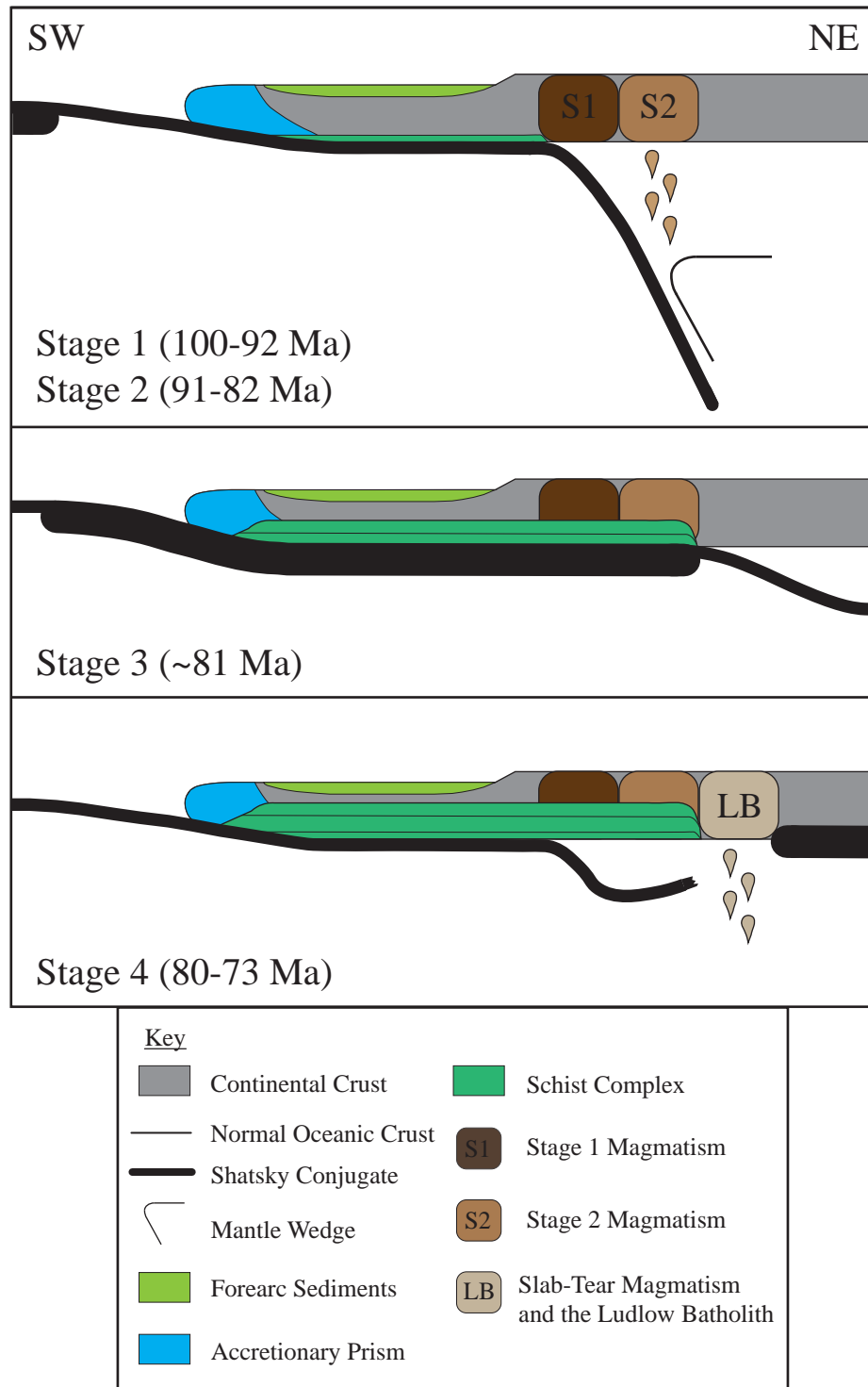


Figure 39. Interpretative Tectonic Diagram. Stage 4 represents the diachronous sweep of slab-tear throughout the Mojave, which includes emplacement of the Ludlow batholith. Adapted from Vermillion et al., in prep.

because the Farallon plate had reached an angle of subduction low enough that a mantle wedge no longer existed, and melting was not occurring in the upper mantle as it had been during the previous stage (Fig. 39). Any slab tear had yet to propagate, therefore leaving a brief time devoid of magmatism in the central Mojave Desert (Fig. 39). The timing of the onset of the magmatic lull varies throughout the Mojave Desert because of the continuous flattening of the subducting slab and the eastward migration of magmatism and the mantle wedge. Stage 4 (80-73 Ma) results from the propagation of a slab tear between the Farallon plate and the Shatsky conjugate (Fig. 39). As the Shatsky conjugate continually travelled along the bottom of the North American plate due to its increased buoyancy when compared to regular oceanic lithosphere, the negative buoyant forces were continually pulling the Farallon plate towards the mantle and away from the Shatsky conjugate (Fig. 39). Eventually, normal oceanic crust began to subduct again at increasingly more normal angles, and once the oceanic crust sank far enough, a slab tear developed at the boundary between the Farallon plate and the backside of the Shatsky conjugate (Fig. 39). This slab tear opened up significant space at the boundary of the oceanic plateau that was filled by an asthenospheric upwelling of deep melt, which generated the Ludlow batholith (Fig. 39). Slab tear likely occurred over the course of a few million years, which is evident in the range of radiometric ages produced by samples collected from the Bristol Mountains (Fig. 7, 22, 39). The Ludlow batholith also likely represents only a small portion of a larger diachronous sweep of slab-tear across the Mojave during the Late Cretaceous, that also gave rise to the similarly aged Cadiz Valley batholith (Howard, 2002). By this point in time, the crust of the Mojave Desert has largely been replaced by the schist complex as a result of continuous underplating from

flat-slab subduction (Chapman et al., 2010; Grove et al., 2003; Jacobson et al., 2011) (Fig. 39). Emplacement of the Rand and Pelona schists and slab-tear magmatism could not have taken place at the same time and space in the central Mojave because schist emplacement results from the existence of a subducting flat-slab, while slab-tear magmatism results from the creation of space behind or within the flat-slab (Fig. 39). Schist emplacement was likely still occurring throughout the central Mojave up until few million years before the intrusion of the Ludlow batholith, and apparently even after that in other areas of the Mojave Desert (Grove et al., 2003; Jacobson et al., 2011).

CONCLUSIONS

Several conclusions can be made based on the data presented within this study.

(1) The five felsic units located within the Bristol Mountains mapping site are all cogenetically related based on their similar ages (ranging from 77.2 ± 1.0 Ma to 74.6 ± 1.1 Ma), and compositions (Fig. 7, 9-13, 22, 27-30). All five units calcic or calc-alkali (Fig. 27), peraluminous (Fig. 28), magnesian (Fig. 29), and either granodiorite or granite with slightly varying mineralogy (Fig. 9-13, 30). Geochemical data for Bristol Mountain samples also create trends that indicate that the five units were derived from the same magma source that differentiated over a few million years (Fig. 7, 22, 24-26).

(2) Based on U/Pb zircon geochronology data from this study, Hess (2017), and data from analogous pluton described in Needy et al., 2009, the rate of magma intrusion for the Ludlow batholith is estimated to range from about $7,300 \text{ km}^3/\text{Ma}$ to $10,000 \text{ km}^3/\text{Ma}$ (Fig. 7, 22, 36, 38).

(3) There are two possible scenarios for how the five felsic units in the Bristol Mountains differentiated. Either there is an inward-younging trend, where the outer units are the two oldest units and the three central units are younger, or the units become younger from the southeastern most unit to the northwestern most unit (Fig. 7). The preferred scenario is the latter, mainly because of the concave shape of the contacts between units, and the changes in texture from equigranular to porphyritic from the southeast to the northwest (Fig. 7, 9-13). The Bristol Mountains intrusions are also similar in composition to rocks from other intrusive suites, and best follow the trends seen throughout these intrusive suites when units are described as younging from the southeast to the northwest (Fig 7).

(4) Exposures of geochemically and petrologically similar plutonic rocks in specific areas within the Bristol Mountains and Rodman Mountains are here identified as the Ludlow batholith (Fig. 36). These two areas are separated by about 50 km and have been determined to be cogenetically related based on their similar mineralogy and geochemical composition (Fig. 27-30). The intervening area, currently obscured by Cenozoic cover, is likely also underlain by a contiguous batholith, which may be responsible for the somewhat negative gravity anomaly in the area (Fig. 38).

(5) U/Pb zircon geochronology and geochemical data indicate that the Ludlow batholith is not a product of normal arc (Fig. 22, 31-35). Instead, the batholith likely formed after arc magmatism was stopped by shallow subduction of an oceanic plateau, and its magma was sourced from a greater depth than is to be expected from arc-related melts, based on its heavy-rare-earth-element depletion (Fig. 33-35, 39). The preferred tectonic model to explain the possible magmatic origin of the Ludlow batholith is that there was asthenospheric upwelling related to a slab-tear event (Fig. 39). Low-angle subduction of the Farallon plate resulted from subduction of the relatively buoyant Shatsky conjugate (Chen and Moore, 1982; Liu et al., 2010; Saleeby, 2003) (Fig. 2, 3). Over time, as the Shatsky conjugate travelled inboard at the base of the North American plate and subduction at the margin began to return to a normal, tension at the boundary of the Farallon plate and Shatsky conjugate could have built up, leading to a slab-tear event (Fig. 39). Asthenosphere would have risen to fill the newly formed space, leading to decompression melting hydrated by the slabs on either side, leading to the formation of what is now known as the Ludlow batholith (Fig. 39).

References

- Anderson, J., & Bender, E. (1989). Nature and origin of Proterozoic A-type granitic magmatism in the southwestern United States of America. *Lithos*, 23(1-2), 19-52.
doi:10.1016/0024-4937(89)90021-2
- Barth, A. P., Wooden, J. L., Howard, K. A., & Richards, J. L. (2008). Late Jurassic plutonism in the southwest U.S. Cordillera. *Geologic Society of America Special Paper 438: Ophiolites, Arcs, and Batholiths: A Tribute to Cliff Hopson*, 379-396.
doi:10.1130/2008.2438(13)
- Barth, A., Wooden, J., Coleman, D., & Vogel, M. (2009). Assembling and Disassembling California: A Zircon and Monazite Geochronologic Framework for Proterozoic Crustal Evolution in Southern California. *The Journal of Geology*, 117(3), 221-239.
doi:10.1086/597515
- Barth, A., Wooden, J., Miller, D., Howard, K., Fox, L., Schermer, E., & Jacobson, C. (2016). Regional and temporal variability of melts during a Cordilleran magma pulse: Age and chemical evolution of the Jurassic arc, eastern Mojave Desert, California. *Geological Society of America Bulletin*, 129(3-4), 429-448.
doi:10.1130/b31550.1
- Bateman, P.C. (1992). Plutonism in the central part of the Sierra Nevada batholith, California: U.S. Geological Survey Professional Paper, v. 1483, 186 p

Bedford, D.R., Miller, D.M. and Phelps, G.A. (2010). Surficial geologic map of the Amboy 30' x 60' quadrangle, San Bernardino County, California: U.S. Geological Survey Scientific Investigations Map 3109, scale 1:100,000.

Burchfiel, B. C., & Davis, G. A. (1975). Nature and Controls of Cordilleran Orogenesis, Western United States: Extensions of an Earlier Synthesis. *American Journal of Science*, 274-A, 363-396.

Cecil, M. R., Ferrer, M. A., Riggs, N. R., Marsaglia, K., Kylander-Clark, A., Ducea, M. N., & Stone, P. (2018). Early arc Development recorded in Permian–Triassic plutons of the northern Mojave Desert region, California, USA. *GSA Bulletin*, 131(5-6), 749-765. doi:10.1130/b31963.1

Chapman, A. D., Jacobson, C. E., Ernst, W., Grove, M., Dumitru, T., Hourigan, J., & Ducea, M. N. (2016). Assembling the world's type shallow Subduction complex: Detrital zircon geochronologic constraints on the origin of the Nacimiento block, central California Coast Ranges. *Geosphere*, 12(2), 533-557. doi:10.1130/ges01257.1

Chapman, A. D., Kidder, S., Saleeby, J. B., & Ducea, M. N. (2010). Role of extrusion of the Rand and Sierra de Salinas Schists in Late Cretaceous extension and rotation of the southern Sierra Nevada and vicinity. *Tectonics*, 29(5). doi:10.1029/2009tc002597

- Chen, J. H., & Moore, J. G. (1982). Uranium-lead isotopic ages from the Sierra Nevada batholith, California. *Journal of Geophysical Research: Solid Earth*, 87(B6), 4761-4784. doi:10.1029/jb087ib06p04761
- Clemens-Knott, D., & Saleeby, J. B. (1999). Impinging ring dike complexes in the Sierra Nevada batholith, California: Roots of the Early Cretaceous volcanic arc. *GSA Bulletin*, 111(4), 484-496. doi:https://doi.org/10.1130/0016-7606(1999)1112.3.CO;2
- Coleman, D. S., Gray, W., & Glazner, A. F. (2004). Rethinking the emplacement and evolution of zoned plutons: Geochronologic evidence for incremental assembly of the Tuolumne Intrusive Suite, California. *Geology*, 32(5), 433. doi:10.1130/g20220.1
- Coney, P. J., & Harms, T. A. (1984). Cordilleran metamorphic core complexes: Cenozoic extensional relics of Mesozoic compression. *Geology*, 12(9), 550. doi:10.1130/0091-7613(1984)122.0.co;2
- Constenius, K. N. (1996). Late Paleogene extensional collapse of the cordilleran foreland fold and thrust belt. *Geological Society of America Bulletin*, 108(1), 20-39. doi:10.1130/0016-7606(1996)1082.3.co;2
- Cross, W., Iddings, J. P., Pirsson, L. V., & Washington, H. S. (1902). A quantitative chemico-mineralogical classification and nomenclature of igneous rocks. *The Journal of Geology*, 10(6), 555-690. doi:10.1086/621030

DeCelles, P. G. (2004). Late Jurassic to Eocene evolution of the cordilleran thrust belt and foreland Basin SYSTEM, western U.S.A. *American Journal of Science*, 304(2), 105-168. doi:10.2475/ajs.304.2.105

Dibblee, T.W. (1964). Geologic map of the Rodman Mountains quadrangle, San Bernardino County, California: U.S. Geological Survey, I-430, scale 1:62,500.

Dibblee, T.W., and Bassett, A.M. (1966). Geologic map of the Cady Mountains quadrangle, San Bernardino County, California: U.S. Geological Survey, I-467, scale 1:62,500.

Dibblee, T.W. (1966). Geologic map of the Lavic quadrangle, San Bernardino County, California: U.S. Geological Survey, I-472, scale 1:62,500.

Dibblee, T.W. (1967). Geologic map of the Broadwell Lake quadrangle, San Bernardino County, California: U.S. Geological Survey, I-478, scale 1:62,500.

Dibblee, T.W. (1967). Geologic map of the Ludlow quadrangle, San Bernardino County, California: U.S. Geological Survey, I-477, scale 1:62,500.

Ducea, M. (2001). The California arc: Thick granitic batholiths, eclogitic residues, lithospheric-scale thrusting, and magmatic flare-ups. *GSA Today*, 11(11), 4. doi:10.1130/1052-5173(2001)0112.0.co;2

Fox, L. K., & Miller, D. M. (1990). Chapter 7: Jurassic Granitoids and Related rocks of the southern Bristol Mountains, southern Providence mountains, and Colton Hills, Mojave Desert, California. *Geological Society of America Memoirs*, 111-132.

doi:10.1130/mem174-p111

Glazner, A. F. (1988). Stratigraphy, structure, and potassic alteration of Miocene volcanic rocks in the Sleeping Beauty Area, central Mojave Desert, California. *Geological Society of America Bulletin*, 100(3), 424-435. doi:10.1130/0016-

7606(1988)1002.3.co;2

Glazner, A. F., Bartley, J. M., & Sanner, W. K. (2000). Nature of the southwestern boundary of the central Mojave Tertiary province, Rodman Mountains, California.

Geological Society of America Bulletin, 112(1), 34-44. doi:10.1130/0016-

7606(2000)1122.0.co;2

Glazner, A. F., Walker, J. D., Bartley, J. M., & Fletcher, J. M. (2002). Cenozoic evolution of the Mojave block of southern California. *Geologic Evolution of the*

Mojave Desert and Southwestern Basin and Range. doi:10.1130/0-8137-1195-9.19

Glazner, A. F., Walker, J. D., Bartley, J. M., & Fletcher, J. M. (2002). Cenozoic

evolution of the Mojave block of southern California. *Geologic Evolution of the*

Mojave Desert and Southwestern Basin and Range. doi:10.1130/0-8137-1195-9.19

Green, D., & Ringwood, A. (1967). The stability fields of aluminous pyroxene peridotite and garnet peridotite and their relevance in upper mantle structure. *Earth and*

Planetary Science Letters, 3, 151-160. doi:10.1016/0012-821x(67)90027-1

Grove, M., Jacobson, C. E., Barth, A. P., & Vucic, A. (2003). Temporal and spatial trends of Late Cretaceous-early Tertiary underplating Pelona and related Schist beneath southern California and southwestern Arizona. Tectonic Evolution of Northwestern Mexico and the Southwestern USA. doi:10.1130/0-8137-2374-4.381

Hess, Lee. (2017) "Late Cretaceous Extensional Collapse of the Southern Cordillera: Evidence from the Bristol and Granite Mountains, SE California" (2017). UNLV Theses, Dissertations, Professional Papers, and Capstones. 2984.

Hildebrand, R. S., & Whalen, J. B. (2014). Arc and slab-failure magmatism in Cordilleran Batholiths II – The Cretaceous Peninsular Ranges Batholith of southern and Baja California. *Geoscience Canada*, 41(4), 399.
doi:10.12789/geocanj.2014.41.059

Hildebrand, R. S., & Whalen, J. B. (2017). The Tectonic Setting and Origin of Cretaceous Batholiths within the North American Cordillera: The Case for Slab Failure Magmatism and Its Significance for Crustal Growth. *Geological Society of America Special Paper 532*. doi:10.1130/2017.2532

Hirt, W. H. (2007). Petrology of the mount Whitney Intrusive Suite, eastern Sierra Nevada, California: Implications for the emplacement and differentiation of Composite felsic intrusions. *Geological Society of America Bulletin*, 119(9-10), 1185-1200. doi:10.1130/b26054.1

- Howard, K.A. (2002). Geologic map of the Sheep Hole Mountains 30' x 60' quadrangle, San Bernardino and Riverside Counties, California: U.S. Geological Survey Geologic Investigations Series I-2344, scale 1:100,000, available at <https://pubs.usgs.gov/mf/2002/2344/>.
- Irwin, W. P., & Wooden, J. L. (2001). Map showing plutons and Accreted terranes of the Sierra Nevada, California, with a tabulation of U/Pb isotopic ages [Map]. In Map showing plutons and accreted terranes of the Sierra Nevada, California, with a tabulation of U/Pb isotopic ages. Reston, VA: U.S. Geological Survey.
- Jacobson, C. E., Grove, M., Pedrick, J. N., Barth, A. P., Marsaglia, K. M., Gehrels, G. E., & Nourse, J. A. (2011). Late Cretaceous-early Cenozoic tectonic evolution of the southern California margin inferred from provenance of trench and forearc sediments. *Geological Society of America Bulletin*, 123(3-4), 485-506.
doi:10.1130/b30238.1
- Johnson, K. T. (1998). Experimental determination of partition coefficients for rare earth and high-field-strength elements between clinopyroxene, garnet, and basaltic melt at high pressures. *Contributions to Mineralogy and Petrology*, 133(1-2), 60-68.
doi:10.1007/s004100050437
- Kistler, R. W., & Peterman, Z. E. (1973). Variations in SR, Rb, K, Na, and Initial Sr87/Sr86 in Mesozoic granitic rocks and Intruded wall rocks in Central California. *Geological Society of America Bulletin*, 84(11), 3489. doi:10.1130/0016-7606(1973)842.0.co;2

Langenheim, V. E., & Jachens, R.C. (2002). The Emerson Lake body: A link between the landers and Hector Mine Earthquakes, Southern California, as inferred from gravity and magnetic anomalies. *Bulletin of the Seismological Society of America*, 92(4), 1606-1620. doi:10.1785/0120000906

Liu, L., Gurnis, M., Seton, M., Saleeby, J., Müller, R. D., & Jackson, J. M. (2010). The role of oceanic plateau Subduction in the Laramide orogeny. *Nature Geoscience*, 3(5), 353-357. doi:10.1038/ngeo829

Livaccari, R. F. (1991). Role of crustal thickening and extensional collapse in the tectonic evolution of the Sevier-Laramide orogeny, western United States. *Geology*, 19(11), 1104. doi:10.1130/0091-7613(1991)0192.3.co;2

Luyendyk, B. P. (1991). A model For Neogene Crustal Rotations, Transtension, and Transpression in southern California. *Geological Society of America Bulletin*, 103(11), 1528. doi:10.1130/0016-7606(1991)1032.3.co;2

Martin, M. W., & Walker, J. D. (1992). Extending the western North American Proterozoic and Paleozoic continental crust through the Mojave Desert. *Geology*, 20(8), 753. doi:10.1130/0091-7613(1992)0202.3.co;2

Miller, C. F. (1978). Early alkalic plutonism in the calc-alkalic batholithic belt of California. *Geology*, 5(11), 685. doi:10.1130/0091-7613(1977)52.0.co;2

Miller, J. S., Glazner, A. F., Walker, J. D., & Martin, M. W. (1995). Geochronologic and isotopic evidence for Triassic-Jurassic emplacement of the eugeoclinal Allochthon in the Mojave Desert region, California. *Geological Society of America Bulletin*, 107(12), 1441-1457. doi:10.1130/0016-7606(1995)1072.3.co;2

Needy, S. K., Anderson, J. L., Wooden, J. L., Fleck, R., Barth, A. P., Paterson, S. R., . . . Pignotta, G. S. (2009). Mesozoic magmatism in an upper- to Middle-crustal section through the Cordilleran continental margin arc, Eastern Transverse Ranges, California. *Crustal Cross Sections from the Western North American Cordillera and Elsewhere: Implications for Tectonic and Petrologic Processes*. doi:10.1130/2009.2456(07)

O'Hara, M. J., Richardson, S. W., & Wilson, G. (1971). Garnet-peridotite stability and occurrence in crust and mantle. *Contributions to Mineralogy and Petrology*, 32(1), 48-68. doi:10.1007/bf00372233

Ross, T. M., Luyendyk, B. P., & Haston, R. B. (1989). Paleomagnetic evidence for Neogene Clockwise tectonic rotations in the central Mojave Desert, California. *Geology*, 17(5), 470. doi:10.1130/0091-7613(1989)0172.3.co;2

Saleeby, J. (2003). Segmentation of the Laramide slab—Evidence from the southern Sierra Nevada region. *Geological Society of America Bulletin*, 115, 655-668. doi:10.1130/0016-7606(2003)1152.0.co;2

Schermer, E. R., & Busby, C. (1994). Jurassic magmatism in the Central Mojave Desert: Implications for arc paleogeography and preservation of continental volcanic sequences. *Geological Society of America Bulletin*, 106(6), 767-790.

doi:10.1130/0016-7606(1994)1062.3.co;2

Shimizu, N., & Kushiro, I. (1975). The partitioning of rare earth elements between garnet and liquid at high pressures: Preliminary experiments. *Geophysical Research Letters*, 2(10), 413-416. doi:10.1029/g1002i010p00413

Stewart, J. H., & Poole, F. G. (1975). Extension of the Cordilleran Miogeosynclinal belt to the San Andreas Fault, Southern California. *Geological Society of America Bulletin*, 86(2), 205. doi:10.1130/0016-7606(1975)862.0.co;2

Stone, P., & Stevens, C. H. (1988). Pennsylvanian and Early Permian Paleogeography of east-central California: Implications for the shape of the continental margin and the timing of continental truncation. *Geology*, 16(4), 330. doi:10.1130/0091-7613(1988)0162.3.co;2

Stone, P., Howard, K. A., & Hamilton, W. (1984). Correlation of metamorphosed Paleozoic strata of the southeastern Mojave Desert region, California and Arizona: Discussion and reply. *Geological Society of America Bulletin*, 95(12), 1485.

doi:10.1130/0016-7606(1984)952.0.co;2

- Strickland, B. A., Wooden, J. L., Mattinson, C. G., Ushikubo, T., Miller, D. M., & Valley, J. W. (2013). Proterozoic evolution of the Mojave crustal province as preserved in the Ivanpah Mountains, southeastern California. *Precambrian Research*, 224, 222-241. doi:10.1016/j.precamres.2012.09.006
- Tosdal, R. M., & Wooden, J. L. (2015). Construction of the Jurassic Magmatic arc, southeast California and southwest Arizona. *Geological Society of America Special Papers*, 189-221. doi:10.1130/2015.2513(04)
- Van Buer, N. J., & Miller, E. L. (2010). Sahwave Batholith, NW Nevada: Cretaceous arc flare-up in a basinal terrane. *Lithosphere*, 2(6), 423-446. doi:10.1130/1105.1
- Vermeesch, P. (2018). Isoplotr: A free and Open toolbox for geochronology. *Geoscience Frontiers*, 9(5), 1479-1493. doi:10.1016/j.gsf.2018.04.001
- Vermillion, K. B., & Van Buer, N. J., & Holk, G. (in prep). Mesozoic Magmatism and Arc Cessation in the Central Mojave Desert, California: in Context of Regional Geochemical and Oxygen-Hydrogen Isotopic Data.
- Wells, R. E., & Hillhouse, J. W. (1989). Paleomagnetism and Tectonic rotation of the lower Miocene peach springs Tuff: Colorado Plateau, Arizona, to Barstow, California. *Geological Society of America Bulletin*, 101(6), 846-863. doi:10.1130/0016-7606(1989)1012.3.co;2

Wood, D. J., & Saleeby, J. B. (1997). Late Cretaceous-Paleocene extensional collapse and disaggregation of the southernmost sierra Nevada batholith. *International Geology Review*, 39(11), 973-1009. doi:10.1080/00206819709465314

Wooden, J. L., & Miller, D. M. (1990). Chronologic and isotopic framework for Early Proterozoic crustal evolution in the eastern Mojave Desert Region, SE California. *Journal of Geophysical Research*, 95(B12), 20133. doi:10.1029/jb095ib12p20133

Yonkee, W. A., & Weil, A. B. (2015). Tectonic evolution of the Sevier and Laramide belts within the North American cordillera Orogenic system. *Earth-Science Reviews*, 150, 531-593. doi:10.1016/j.earscirev.2015.08.001

APPENDIX

U/Pb Geochronology Data

Spot Name	ppm U	ppm Th	7-corr ppm 206*	7-corr ppm 208*	232Th /238U	% err	Total 206Pb /238U	% err
Gb1905-9.1	488	428	4.5	1.30	0.91	0.44	0.0109	4.4
Gb1905-10.1	693	418	6.6	1.35	0.62	1.81	0.0111	3.2
Gb1905-7.1	824	475	8.1	1.58	0.59	0.12	0.0116	2.0
Gb1905-6.1	719	862	7.2	2.71	1.24	0.63	0.0117	2.1
Gb1905-11.1	508	309	5.1	1.00	0.63	0.72	0.0117	2.4
Gb1905-12.1	2438	2106	24.4	6.78	0.89	1.11	0.0116	2.3
Gb1905-4.1	621	360	6.2	1.22	0.60	0.98	0.0117	2.3
Gb1905-8.1	763	683	7.7	2.23	0.92	0.55	0.0118	2.3
Gb1905-1.1	91	144	0.9	0.48	1.65	0.70	0.0120	1.6
Gb1905-2.1	560	376	5.8	1.36	0.69	2.39	0.0120	2.3
Gb1905-3.1	329	537	3.5	1.92	1.69	3.45	0.0124	2.0
Gb1905-5.1	395	426	8.8	3.10	1.11	0.38	0.0260	2.3

Spot Name	Total 208Pb /232Th	% err	Age S-K com Pb	C-Pb 206 /204	C-Pb 207 /206	C-Pb 208 /206	204corr 206Pb /238U Age	1σ err
Gb1905-9.1	0.0037	4.8	69	18.60	0.840	2.070	69.8	3
Gb1905-10.1	0.0037	4.6	71	18.60	0.840	2.070	70.7	2
Gb1905-7.1	0.0041	2.6	73	18.59	0.840	2.070	73.4	1
Gb1905-6.1	0.0036	3.1	74	18.59	0.840	2.070	74.6	2
Gb1905-11.1	0.0039	3.2	75	18.59	0.840	2.070	73.9	2
Gb1905-12.1	0.0036	2.7	75	18.59	0.840	2.070	74.6	2
Gb1905-4.1	0.0038	3.2	75	18.59	0.840	2.070	74.6	2
Gb1905-8.1	0.0037	2.8	75	18.59	0.841	2.071	75.5	2
Gb1905-1.1	0.0038	4.1	76	18.59	0.841	2.071	76.3	1
Gb1905-2.1	0.0039	3.8	77	18.59	0.841	2.071	77.0	2
Gb1905-3.1	0.0040	5.9	79	18.58	0.841	2.071	79.0	2
Gb1905-5.1	0.0081	2.6	166	18.45	0.846	2.077	166	11

Spot Name	207corr 206Pb /238U Age	1σ err	208corr 206Pb /238U Age	% err	204corr 207Pb /206Pb Age	1σ err	204corr 208Pb /232Th Age	1σ err	% Dis-cordant
Gb1905-9.1	69.3	3	69.5	3.6	365	254	72.3	3	+81
Gb1905-10.1	70.9	2	70.7	2.5	-37	94	70.9	3	+291
Gb1905-7.1	73.5	1	73.3	1.7	19.9	132	74.0	2	-270
Gb1905-6.1	74.4	2	75.3	2.0	187	65	71.9	2	+60
Gb1905-11.1	74.5	2	74.7	2.0	-282	167	66.8	3	+127
Gb1905-12.1	74.6	2	75.0	2.0	66.9	35	72.4	2	-12
Gb1905-4.1	74.7	2	74.6	1.9	13.3	81	74.9	3	-462
Gb1905-8.1	75.2	2	75.5	2.0	247	67	76.1	2	+70
Gb1905-1.1	76.3	1	76.6	2.0	83.9	248	75.5	3	+9
Gb1905-2.1	77.3	2	76.9	2.0	-90	74	78.4	3	+187
Gb1905-3.1	79.4	2	79.1	2.7	-170	125	78.6	5	+147
Gb1905-5.1	166	4	166	4.5	171	2337	164	61	+3

Spot Name	ppm U	ppm Th	7-corr ppm 206*	7-corr ppm 208*	232Th /238U	% err	Total 206Pb /238U	% err
Gb1907-8.1	203	173	2.1	0.56	0.88	0.77	0.0118	1.8
Gb1907-3.1	164	118	1.7	0.37	0.74	2.52	0.0120	2.2
Gb1907-1.1	159	166	1.6	0.53	1.08	2.50	0.0120	2.4
Gb1907-11.1	139	104	1.4	0.34	0.77	0.26	0.0119	2.2
Gb1907-9.1	111	77	1.1	0.26	0.72	0.31	0.0119	3.0
Gb1907-10.1	156	125	1.6	0.45	0.83	0.24	0.0119	2.0
Gb1907-5.1	211	264	2.2	0.92	1.29	0.60	0.0121	2.4
Gb1907-6.1	167	149	1.7	0.50	0.92	0.25	0.0121	1.5
Gb1907-7.1	162	116	1.7	0.42	0.74	2.81	0.0122	3.2
Gb1907-12.1	180	132	1.9	0.44	0.76	0.25	0.0122	1.3
Gb1907-2.1	120	103	2.4	0.69	0.89	0.82	0.0239	2.1
Gb1907-4.1	75	48	1.6	0.34	0.65	0.40	0.0244	3.0

Spot Name	Total 208Pb /232Th	% err	Age S-K com Pb	C-Pb 206 /204	C-Pb 207 /206	C-Pb 208 /206	204corr 206Pb /238U Age	1σ err
Gb1907-8.1	0.0036	3.7	76	18.59	0.841	2.071	75.4	1
Gb1907-3.1	0.0038	4.9	76	18.59	0.841	2.071	77.0	26
Gb1907-1.1	0.0037	6.8	76	18.59	0.841	2.071	76.8	2
Gb1907-11.1	0.0037	4.4	76	18.59	0.841	2.071	76.1	2
Gb1907-9.1	0.0036	5.3	77	18.59	0.841	2.071	76.2	2
Gb1907-10.1	0.0039	3.9	77	18.59	0.841	2.071	76.2	2
Gb1907-5.1	0.0038	3.4	77	18.59	0.841	2.071	77.3	2
Gb1907-6.1	0.0037	3.5	78	18.58	0.841	2.071	78.0	24
Gb1907-7.1	0.0041	10.4	78	18.58	0.841	2.071	78.0	2
Gb1907-12.1	0.0037	3.8	79	18.58	0.841	2.071	78.6	1
Gb1907-2.1	0.0077	3.7	152	18.47	0.846	2.076	153	3
Gb1907-4.1	0.0080	5.0	156	18.47	0.846	2.076	157	5

Spot Name	207corr 206Pb /238U Age	1σ err	208corr 206Pb /238U Age	% err	204corr 207Pb /206Pb Age	1σ err	204corr 208Pb /232Th Age	1σ err	% Dis-cordant
Gb1907-8.1	75.8	1	76.3	1.6	-129	163	69.6	3	+159
Gb1907-3.1	76.0	2	76.8	1.9	519	10028	78.9	227	+86
Gb1907-1.1	76.4	2	77.3	2.4	276	232	74.6	5	+73
Gb1907-11.1	76.4	2	76.8	1.9	-105	199	71.0	4	+173
Gb1907-9.1	76.6	2	76.7	2.6	-161	182	71.6	4	+148
Gb1907-10.1	76.7	2	76.1	1.8	-263	195	76.5	3	+130
Gb1907-5.1	77.4	2	77.2	2.4	55.2	117	77.9	3	-40
Gb1907-6.1	77.9	1	78.2	1.4	141	11564	77.1	168	+45
Gb1907-7.1	78.0	2	77.5	3.0	84.5	135	82.6	9	+8
Gb1907-12.1	78.6	1	79.1	1.2	74.5	230	74.5	3	-5
Gb1907-2.1	452	3	152	3.8	467	153	161	7	+68
Gb1907-4.1	456	5	155	5.2	403	208	173	12	+62

Spot Name	ppm U	ppm Th	7-corr ppm 206*	7-corr ppm 208*	232Th /238U	% err	Total 206Pb /238U	% err
Gb1910-5.1	356	146	3.4	0.47	0.43	1.34	0.0112	3.2
Gb1910-2.1	386	187	3.8	0.60	0.50	0.92	0.0115	2.2
Gb1910-4.1	582	246	5.8	0.83	0.44	0.35	0.0115	2.1
Gb1910-10.1	455	189	4.5	0.64	0.43	9.33	0.0117	3.6
Gb1910-9.1	452	167	4.5	0.58	0.38	2.92	0.0117	3.3
Gb1910-1.1	1968	1117	19.7	3.63	0.59	0.37	0.0117	1.5
Gb1910-12.1	159	56	1.6	0.17	0.37	0.62	0.0117	2.4
Gb1910-6.1	792	302	7.9	0.98	0.39	0.98	0.0117	2.0
Gb1910-11.1	1906	1024	19.2	3.30	0.55	0.66	0.0117	2.8
Gb1910-3.1	92	98	0.9	0.33	1.10	0.29	0.0117	1.2
Gb1910-7.1	901	349	9.2	1.12	0.40	0.51	0.0118	1.6
Gb1910-8.1	110	184	2.5	1.41	1.72	0.56	0.0268	2.3

Spot Name	Total 208Pb /232Th	% err	Age S-K com Pb	C-Pb 206 /204	C-Pb 207 /206	C-Pb 208 /206	204corr 206Pb /238U Age	1σ err
Gb1910-5.1	0.0035	4.7	72	18.59	0.840	2.070	71.8	2
Gb1910-2.1	0.0036	3.6	74	18.59	0.840	2.070	73.5	2
Gb1910-4.1	0.0038	3.3	74	18.59	0.840	2.070	73.8	2
Gb1910-10.1	0.0040	14.5	74	18.59	0.840	2.070	74.7	3
Gb1910-9.1	0.0040	6.6	75	18.59	0.840	2.070	74.9	2
Gb1910-1.1	0.0037	2.0	75	18.59	0.840	2.070	74.7	1
Gb1910-12.1	0.0035	8.7	75	18.59	0.841	2.070	74.7	2
Gb1910-6.1	0.0036	5.3	75	18.59	0.841	2.070	74.8	2
Gb1910-11.1	0.0037	3.1	75	18.59	0.841	2.071	75.1	2
Gb1910-3.1	0.0036	4.3	76	18.59	0.841	2.071	75.7	44
Gb1910-7.1	0.0036	2.7	76	18.59	0.841	2.071	75.9	1
Gb1910-8.1	0.0085	3.9	171	18.44	0.847	2.078	171	4

Spot Name	207corr 206Pb /238U Age	1σ err	208corr 206Pb /238U Age	% err	204corr 207Pb /206Pb Age	1σ err	204corr 208Pb /232Th Age	1σ err	% Dis-cordant
Gb1910-5.1	72.0	2	71.9	2.4	-33	94	69.8	3	+318
Gb1910-2.1	73.6	2	73.6	1.8	54.5	85	72.1	3	-35
Gb1910-4.1	73.8	2	73.7	1.7	33.7	78	74.3	3	-120
Gb1910-10.1	74.4	3	74.3	3.0	236	77	80.7	12	+69
Gb1910-9.1	74.6	2	74.4	2.6	200	103	82.3	6	+63
Gb1910-1.1	74.7	1	74.8	1.2	90.9	70	73.5	2	+18
Gb1910-12.1	74.8	2	75.1	1.9	11.3	154	67.2	6	-565
Gb1910-6.1	74.9	2	75.0	1.6	48.5	60	71.9	4	-55
Gb1910-11.1	75.1	2	75.4	2.3	73.1	64	72.6	2	-3
Gb1910-3.1	75.8	0.9	75.8	1.2	37.7	23895	75.3	264	-102
Gb1910-7.1	76.0	1	76.2	1.3	43.1	58	71.6	2	-76
Gb1910-8.1	174	4	170	5.8	228	151	173	7	+25

Cal Poly Pomona XRF Raw Data

Sample	Sum	Result type	Na2O	MgO	Al2O3	SiO2	P2O5	K2O	CaO	TiO2	MnO	FeO
	of conc.		Na	Mg	Al	Si	P	K	Ca	Ti	Mn	Fe
	(%)		(%)	(%)	(%)	(%)	(%)	(%)	(%)	(%)	(%)	(%)
GB1923 B	95.44	Concentration	4.045	0.442	13.654	70.622	0.062	3.038	2.275	0.165	0.03	0.971
GB1922 B	95.274	Concentration	3.925	0.436	14.123	69.861	0.05	3.457	2.281	0.14	0.021	0.799
GB1921 B	95.541	Concentration	4.038	0.457	13.775	70.536	0.061	3.095	2.245	0.174	0.028	0.975
GB1916 B	95.545	Concentration	3.714	1.124	14.645	66.816	0.149	3.671	2.499	0.402	0.043	2.227
GB1918 B	96.161	Concentration	3.378	0.457	12.906	72.138	0.079	3.814	1.793	0.208	0.028	1.144
GB1915 B	97.401	Concentration	3.75	2.056	15.536	65.149	0.19	3.293	3.707	0.415	0.055	2.965
GB1920 B	94.95	Concentration	3.906	0.424	13.787	70.295	0.059	3.256	1.998	0.154	0.028	0.887
GB1917 B	95.312	Concentration	3.103	0.467	12.217	72.438	0.068	4.314	1.249	0.181	0.033	1.066
GB1919 B	95.161	Concentration	3.656	0.5	14.181	68.884	0.074	4.377	1.945	0.191	0.04	1.101
GB1923 A	94.557	Concentration	3.977	0.431	13.361	70.164	0.06	3.021	2.254	0.165	0.03	0.963
GB1922 A	95.267	Concentration	3.914	0.43	14.08	69.938	0.049	3.444	2.283	0.138	0.021	0.796
GB1921 A	95.352	Concentration	4.026	0.458	13.728	70.424	0.061	3.086	2.226	0.177	0.028	0.988
GB1915 A	97.633	Concentration	3.75	2.046	15.589	65.319	0.191	3.292	3.714	0.414	0.055	2.972
GB1916 A	96.449	Concentration	3.758	1.15	14.846	67.445	0.152	3.693	2.512	0.404	0.043	2.187
GB1917 A	95.04	Concentration	3.083	0.476	12.201	72.211	0.068	4.3	1.244	0.184	0.033	1.063
GB1918 A	93.797	Concentration	3.199	0.435	12.271	70.695	0.078	3.77	1.775	0.208	0.027	1.128
GB1920 A	94.8	Concentration	3.883	0.425	13.75	70.204	0.056	3.25	1.995	0.156	0.028	0.89
GB1919 A	95.153	Concentration	3.631	0.498	14.066	69.06	0.073	4.351	1.936	0.188	0.04	1.103